

**GENESIS OF COPPER-PRECIOUS METAL SULFIDE DEPOSITS
IN THE PORT COLDWELL ALKALIC COMPLEX, ONTARIO**

By

DAVID JOHN GOOD, M.Sc.

A Thesis

Submitted to the School of Graduate Studies

in Partial Fulfilment of the Requirements

for the Degree

Doctor of Philosophy

McMaster University

(c) Copyright by David John Good, February 1992

GENESIS OF Cu-PGE SULFIDE DEPOSITS IN THE COLDWELL COMPLEX

DOCTOR OF PHILOSOPHY (1992)
(Geology)

McMASTER UNIVERSITY
Hamilton, Ontario

TITLE: Genesis of Copper-Precious Metal Sulfide Deposits
in the Port Coldwell Alkalic Complex

AUTHOR: David John Good, B.Sc. (McMaster University)
M.Sc. (University of Toronto)

SUPERVISOR: Professor J.H. Crocket

NUMBER OF PAGES: xii, 203

Abstract

Two gabbro-hosted sulfide deposits in the Port Coldwell alkalic complex were studied to determine the most probable mode of Cu-precious metal sulfide deposition. The deposits examined are the Marathon deposit (Fleck Resources Ltd.) in the Two Duck Lake gabbro on the eastern margin of the complex, and the MacRae occurrence in the Geordie Lake gabbro located well within the complex.

A magmatic origin for sulfides in the Marathon deposit is consistent with geochemical and petrographic evidence, but is inconsistent with experimental studies for equilibration of sulfide liquids with olivine and/or silicate melts. In general, the proposed sulfide liquid contains too little Ni and Ir, and possibly too much Cu. In addition, metals in the sulfide liquid are fractionated such that their geochemical behaviour becomes increasingly like that of Pd in the order Ni=Ir<<Rh=Pt<Cu<Au, and there is no known phase that could have coexisted with a sulfide liquid to account for this observation. Indeed, the order of fractionation is consistent with partitioning between silicate magma and spinel ± clinopyroxene. Consequently, a possible mechanism that applies the principle of continuous sulfide liquid formation from a silicate magma at various stages of its crystallization history in a pre-existing

magma chamber is proposed. Concentration of sulfide droplets occurred during movement of the Two Duck Lake crystal mush into the present site.

The petrology of sulfide mineralization in the MacRae occurrence is consistent with deposition from a hydrous fluid. The sulfides are strongly enriched in Pd and Au with somewhat weaker concentrations of Rh and Ni. Ir is not concentrated above background. The possibility that the hydrous fluid responsible for mineralization was derived from an evolved silicate magma that intruded the host gabbro and crystallized numerous albite microdikelets and pods is consistent with petrographic and geochemical evidence.

ACKNOWLEDGEMENTS

I express my appreciation to Dr. J.H. Crocket for his patient guidance during the evolution of this thesis. I thank Dr. D.M. Shaw and Dr. L.A. Prevec for their support and insightful comments.

Funding for this project was provided by the Geoscience Research Grant Program grant 341.

I thank Mr. John McGoran (Fleck Resources Ltd.), Bond Gold Canada Inc. (formerly St. Joe Canada Inc.), and Mr. M. Joa and Mr. MacRae, prospectors, for access to their properties, accumulated geological information, and diamond drill core. I thank Fleck Resources Ltd. for providing support to attend the GAC-MAC conference in Vancouver. I also thank Bernie Schnieders, Resident Geologist, and Mark Smyk, Staff Geologist, Schreiber-Hemlo District, Ministry of Northern Development and Mines, for introducing me to the MacRae occurrence, and for their logistical support.

The assistance and advice of Ms. A. Pidruczny at the centre for INAA, McMaster Nuclear Reactor, and of Mr. R. Barnett and Mr. D. Kingston at the Electron microprobe facility, University of Western Ontario are greatly appreciated.

TABLE OF CONTENTS

Chapter 1 - Introduction	
1-1 Introduction	1
1-2 Thesis objectives	3
1-3 Location and access	4
1-4 Geology of the Port Coldwell alkalic complex	4
1-4-1 Previous work	4
1-4-2 General geology	6
1-4-3 Age and tectonic setting	7
1-5 Introduction to platinum-group elements	8
1-6 Geochemical evolution of orthomagmatic Ni-Cu-PGE deposits	9
1-6-1 Acquisition of ore forming elements	9
1-6-2 Silicate magma-mineral partitioning	10
1-6-3 Concentration of OFE	11
A- Silicate melt-sulfide liquid partitioning	11
B- Sulfide liquid-mineral partitioning	13
C- Concentration of sulfide liquid in magma	14
D- Silicate magma-hydrous fluid partitioning	14
Chapter 2 - Petrography	
2-1 Introduction	18
2-2 Geology of the Two Duck Lake intrusion (Marathon Deposit)	18
2-2-1 Petrography	22
A- Upper zone	23
B- Lower zone	25
C- Xenoliths of Eastern gabbro	30
2-2-2 Crystallization history of TDL gabbro	33
2-2-3 Mineral Chemistry	36
A- Pyroxene	36
B- Olivine	42
C- Olivine-pyroxene and pyroxene- pyroxene equilibrium	42
D- Plagioclase	46
E- Significance of two generations of plagioclase	47
2-2-4 Classification of TDL magma	50
2-2-5 Emplacement of TDL magma	52
2-3 Geology of the Geordie Lake gabbro (MacRae occurrence)	53
2-3-1 Petrography of the GL gabbro	56
A- Unmineralized zone	56
B- Mineralized zone	60
2-3-2 Mineral chemistry	64
2-3-3 Albite rims, microdikelets and pods	65
A- Albite rims	66
B- Albite microdikelets	69
C- Albite pods	72

2-3-4	Summary of plagioclase features	76
2-3-5	Discussion	79
Chapter 3 - Geochemistry		
3-1	Introduction	81
3-2	Organization of trace-element data	81
3-3	Geochemistry of the TDL gabbro	82
3-3-1	Compositional cross section	82
3-3-2	Rare earth elements	85
3-3-3	Origin of granophyre	87
A-	Determination of partition coefficients	88
B-	Comparison of trace-element data to model D values: Element-Zr variation diagrams	91
C-	Rayleigh fractionation of interstitial melt	96
3-3-4	Summary	100
3-4	Geochemistry of the Geordie Lake gabbro	101
3-4-1	Cross-section of unmineralized zone	102
3-4-2	Genesis of unmineralized gabbro	104
3-4-3	Mineralized zone	106
3-4-4	Rare earth elements	106
3-4-5	Origin of albite pods	108
A-	Determination of partition coefficients	108
B-	Comparison of trace-element data to model D values: Element-Zr variation diagrams	110
C-	K-Rb fractionation	114
D-	Discussion	116
3-4-6	Summary	118
Chapter 4 - Sulfides and PGE distribution		
4-1	Introduction	120
4-2	Data	120
4-3	Platinum-group minerals	121
4-4	Petrography of sulfides at the Marathon deposit	123
4-4-1	Main sulfide zone	123
4-4-2	Basal sulfide zone	127
4-4-3	Other sulfides	128
4-4-4	Phase relationships and temperatures of sulfide formation	128
4-5	Distribution of ore-forming elements	130
4-5-1	Sulfur-metal variation diagrams	133
4-5-2	Distribution of Ni in various minerals	133
4-5-3	Distribution of Ir in various minerals	136
4-5-4	Silicate melt-sulfide liquid partitioning	137
4-5-5	Sulfide liquid-olivine disequilibrium (K_D3)	139
4-5-6	Mantle normalized PGE, Ni, Cu and Au	142
4-5-7	Pd-metal partitioning	143
4-5-8	Possible mechanisms for Cu, Ni and PGE fractionation	148
4-5-9	Summary	151
4-5-10	Problems	151

4-6	Petrography of sulfides in the MacRae occurrence	152
4-7	Distribution of ore-forming elements	155
4-7-1	Unmineralized zone (background values)	155
4-7-2	Mineralized zone	155
4-7-3	Distribution of Ni and Ir	158
4-7-4	Distribution of Cu and Pd	160
4-7-5	Mantle normalized PGE, Ni, Cu and Au	161
4-8	Discussion	161
Chapter 5 - Discussion and Conclusions		
5-1	Genesis of TDL gabbro	164
5-2	Genesis of sulfides in TDL gabbro	165
5-3	Genesis of GL gabbro	169
5-4	Genesis of sulfides in GL gabbro	170
	References	173
	Appendix I - Whole rock analyses	183
	Introduction	183
	Sample selection	183
	Sample preparation	183
	Major- and trace-element analysis by XRF	184
	Trace-element analysis by INAA	184
	Counting error and reproducibility of INAA data	184
	REE, Ta, Th, Hf, Cs, and Sc analysis	185
	Cl analysis	186
	U analysis	186
	PGE analysis	187
	Appendix II - Mineral Analyses	203

LIST OF FIGURES

1-1	Location of the Port Coldwell alkalic complex	2
1-2	Location of the Marathon deposit and MacRae occurrence	5
2-1	Geology of the Bamooos Lake area	19
2-2	Detailed geological map of the Marathon deposit	20
2-3	Cross-section of the Marathon deposit	21
2-4	Outcrop photographs of TDL intrusion	24
2-5	Photomicrographs and scanning electron photomicrographs of TDL gabbro	26
2-6	Variation of modal mineral abundance across the TDL gabbro	28
2-7	Relationships between TDL gabbro and Eastern gabbro xenoliths	31
2-8	Schematic crystallization history of TDL gabbro	34
2-9	Photomicrographs of TDL gabbro	35
2-10	Variation of mineral compositions across TDL gabbro	40
2-11	Summary of pyroxene and olivine compositions	41
2-12	Geology of the MacRae Occurrence	54
2-13	Geological cross-section of the GL gabbro	55
2-14	CIPW normative mineral abundance across unmineralized zone	58
2-15	Photographs of GL gabbro in unmineralized zone	59
2-16	Textures of GL gabbro in mineralized zone	61
2-17	CIPW normative mineral abundance across mineralized zone	62
2-18	Examination of an albite/oligoclase rim	67
2-19	Textural relationships of albite/oligoclase rims	68
2-20	Examination of an albite microdikelet	71
2-21	Textural relationships at albite pod/gabbro contacts	73
2-22	Photographs of albite pod and neighbouring gabbro	74
2-23	Mineral compositions across an albite pod	75
2-24	Summary of plagioclase compositions	78
3-1	Compositional variation across TDL gabbro	83
3-2	Chondrite normalized REE plot for TDL gabbro	86
3-3	REE-Zr variation diagrams	92
3-4	HFSE-Zr variation diagrams	93
3-5	LILE-Zr variation diagrams	94
3-6	Modelled variation of interstitial melt compositions	99
3-7	Compositional variation across unmineralized section of GL gabbro	103
3-8	Chondrite normalized REE for GL gabbro	107
3-9	REE-Zr variation diagrams for GL gabbro	111
3-10	HFSE-Zr variation diagrams	112

3-11	LILE-Zr variation diagrams	113
3-12	LILE variation diagrams	115
4-1	Common textural relationships in TDL main zone sulfides	126
4-2	Schematic sulfide phase diagrams	129
4-3	Compositional variation of S and metals across the TDL gabbro	132
4-4	Sulfur-metal variation diagrams	134
4-5	Mantle normalized PGE in Marathon deposit	144
4-6	Palladium-metal variation diagrams	145
4-7	Pd/Ir versus Cu/Ni	147
4-8	Photomicrographs of sulfides in MacRae occurrence	154
4-9	Compositional variation of metals across GL gabbro	156
4-10	Mantle normalized PGE in GL gabbro	162

LIST OF TABLES

1.1	Melt-mineral partition coefficients	11
2.1a	Representative microprobe analyses of olivine	37
2.1b	Representative microprobe analyses of pyroxene	38
2.1c	Representative microprobe analyses of plagioclase	39
2.2	Fe-Mg exchange coefficients for mafic minerals	45
3.1	Trace- and minor-element correlation coefficients	84
3.2	Mineral-melt partition coefficients	89
4.1	Platinum-group minerals in in TDL and GL gabbro	122
4.2	Ore-forming elements in TDL gabbro	131
4.3	Ni distribution in various minerals	135
4.4	KD3 calculation	140
4.5	Ore-forming elements in GL gabbro	157

LIST OF PHOTOGRAPHS

Fig. 2-4	Upper and lower zones of TDL intrusion	24
Fig. 2-5	Photomicrographs of TDL gabbro	26
Fig. 2-7	TDL gabbro-xenolith relationships	31
Fig. 2-9	Photomicrographs of TDL gabbro	35
Fig. 2-15	Unmineralized GL gabbro	59
Fig. 2-16	Textures in mineralized zone	61
Fig. 2-18	Examination of albite/oligoclase rim	67
Fig. 2-19	Textures of albite/oligoclase rims	68
Fig. 2-20	Examination of albite microdikelet	71
Fig. 2-21	Albite pod-gabbro relationships	73
Fig. 2-22	Gabbro and albite pod photomicrographs	74
Fig. 4-1	Common sulfide-sulfide and sulfide-plagioclase relationships in TDL gabbro	126
Fig. 4-8	Common sulfide-silicate relationships in GL gabbro	154

LIST OF ABBREVIATIONS

CIPW norm weight norm devised by Cross, Iddings, Pirsson, and Washington (see Hutchinson 1974).

f	fugacity
GL	Geordie Lake
MORB	Mid Ocean Ridge Basalt
OFE	ore-forming element(s)
PGE	platinum-group element(s)
PGM	platinum-group mineral(s)
TDL	Two Duck Lake

Minerals:

Ab	albite content of plagioclase
An	anorthite content of plagioclase
am	amphibole
bi	biotite
ch	chlorite
cpx	clinopyroxene
cpy	chalcopyrite
ct	calcite
Fo	forsterite content of olivine
ks	potassium feldspar
ol	olivine
opx	orthopyroxene
po	pyrrhotite

Preface

The majority of the worlds supply of platinum-group elements (PGE) is extracted from a very few deposits located in Republic of South Africa and Russia. Canada produces a relatively small amount of PGE (4.5 % of the world total), predominantly as a by-product of Ni-Cu production near Sudbury, Ontario. To aid in the search for other deposits, it is important to understand the processes involved in their deposition. This thesis investigates the mode of deposition of PGE in the Marathon deposit and MacRae occurrence, both of which are located within the Port Coldwell alkalic complex. The Marathon deposit is one of only three deposits in Ontario, outside of established mining camps, for which PGE reserves have been calculated, and is one of four of the most advanced prospects in North America. The MacRae occurrence is of lesser economic importance relative to the Marathon deposit, but nevertheless is host to a significant amount of mineralization. Both deposits were studied because on the basis of preliminary field investigation it was known that textural features from each locality were very different, and, consequently it was inferred that the principal mechanisms of PGE deposition were also different.

The thesis consists of three portions. The first (Chapter 1), introduces the objectives of the thesis and the

general geology of the Port Coldwell alkalic complex, and summarizes the geochemical evolution of PGE deposits in terms of partitioning of the ore-forming elements between various phases present during subsequent stages of the crystallization history of mafic magmas. The goal of the second part of the thesis (Chapters 2 and 3) is to define the principal processes that occurred during the intrusive and subsequent crystallization histories of the mineralized gabbroic bodies. The respective models provide a framework that is used in the third section (Chapter 4) to describe the genesis of sulfide and PGE mineralization. In Chapter 4 sulfide-sulfide and sulfide-silicate textural relationships, and the distribution of ore-forming elements are described. The observations are then compared to partitioning behaviour between various mineral systems described in Chapter 1 to determine the most probable mode of PGE deposition in each deposit.

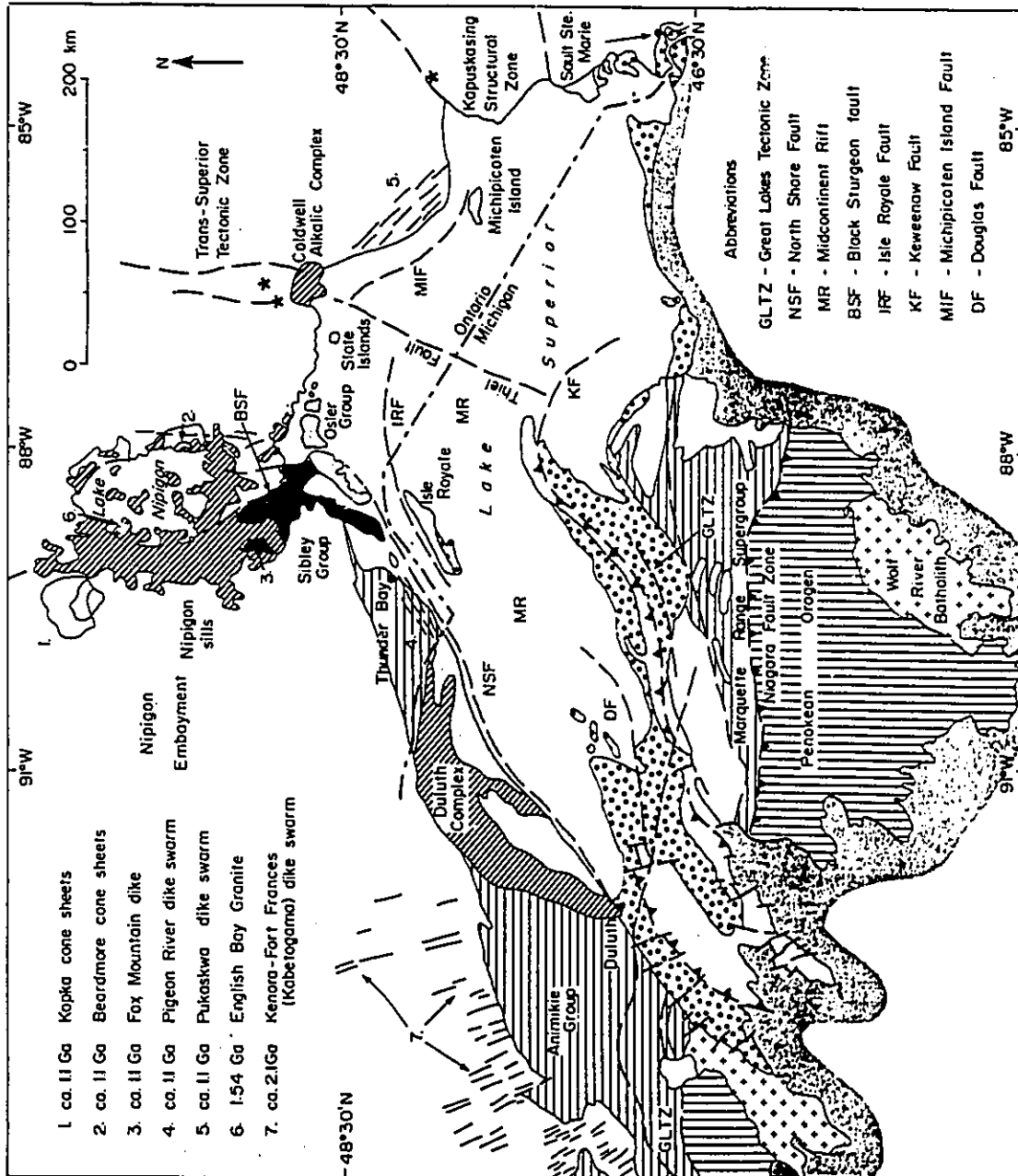
**Genesis of Cu-precious metal sulfide deposits
in the Port Coldwell alkalic complex**

Chapter 1 - Introduction

1-1 Introduction

The lack of economic concentrations of platinum-group elements (PGE) in alkaline complexes is apparent in several reviews of the economic geology and geochemistry of the PGE (e.g. Crocket 1979, 1981; Naldrett and Cabri, 1976; Naldrett, 1981). Documentation of PGE mineralization within the Port Coldwell alkalic complex, located north of Lake Superior near Marathon, Ontario (Fig. 1-1), therefore, is important with respect to determining the potential for alkaline complex settings to host economic deposits. Two PGE deposits within the complex are described in order to obtain a wide range of geochemical and petrographic criteria for distinguishing the processes involved in PGE deposition. The criteria, once established, may be applicable to the interpretation of other deposits, or they could form the basis of models used in exploration.

Fig. 1-1. Location of the Port Coldwell alkalic complex on the north shore of Lake Superior, Ontario. Geological map after Sutcliffe (1991).



1-2 Thesis Objectives

The research is a study of two gabbro-hosted Cu-precious metal sulfide deposits, the MacRae occurrence and the Marathon deposit, located in the Port Coldwell alkalic complex. The former is hosted by the Geordie Lake (GL) gabbro and is located approximately 4 km from the margin of the complex, and the latter by the Two Duck Lake (TDL) gabbro located at the eastern intrusive contact of the complex (Fig. 1-2).

The principal objective of this study is to determine the distribution of Ni, Cu, platinum-group elements (Ir, Rh, Pt, and Pd) and Au in the two deposits for the purpose of:

- i) characterizing the deposits with respect to their noble metal content, and
- ii) defining PGE fractionation trends, to evaluate their implications on probable mode of PGE deposition.

A second objective of the study is to describe the petrology and geochemistry of the host gabbroic bodies for the purpose of:

- i) formulating the crystallization history of each gabbro,
- ii) relating the timing of sulfide mineralization to the silicate crystallization history, and
- iii) assessing the importance of post crystallization geologic processes such as hydrothermal alteration.

1-3 Location and access

The GL gabbro is located about 1 km south of the southern tip of Coubran Lake at $48^{\circ}49'30''$ latitude and $86^{\circ}29'30''$ longitude. The gabbro is accessible by four wheel drive vehicle on the Geordie Lake road that exits north from highway 17, 1.6 km east of the road to Port Coldwell.

The TDL gabbro is located about 1.9 km southeast of the east tip of Bamooos Lake at $48^{\circ}48'10''$ latitude and $86^{\circ}18'45''$ longitude. The gabbro is accessible by four wheel drive vehicle on the Bamooos Lake road that turns off of the Pic River road. The Pic River road exits north from highway 17 just east of the Marathon airfield.

1-4 Geology of the Port Coldwell alkalic complex

1-4-1 Previous work

Valuable reviews of numerous studies covering various portions of the Port Coldwell alkalic complex are found in Puskas (1967), Currie (1980), Wilkinson (1983), Mulja (1989), and Sage (1991). Compilation maps of the complex were produced by Puskas (1967) and Currie (1980). A gravity study of the complex was conducted by Mitchell et al. (1983). A review of Rb/Sr geochronology of the complex is found in Platt & Mitchell (1982), and an U/Pb age for the complex was determined by Heaman & Machado (1987).

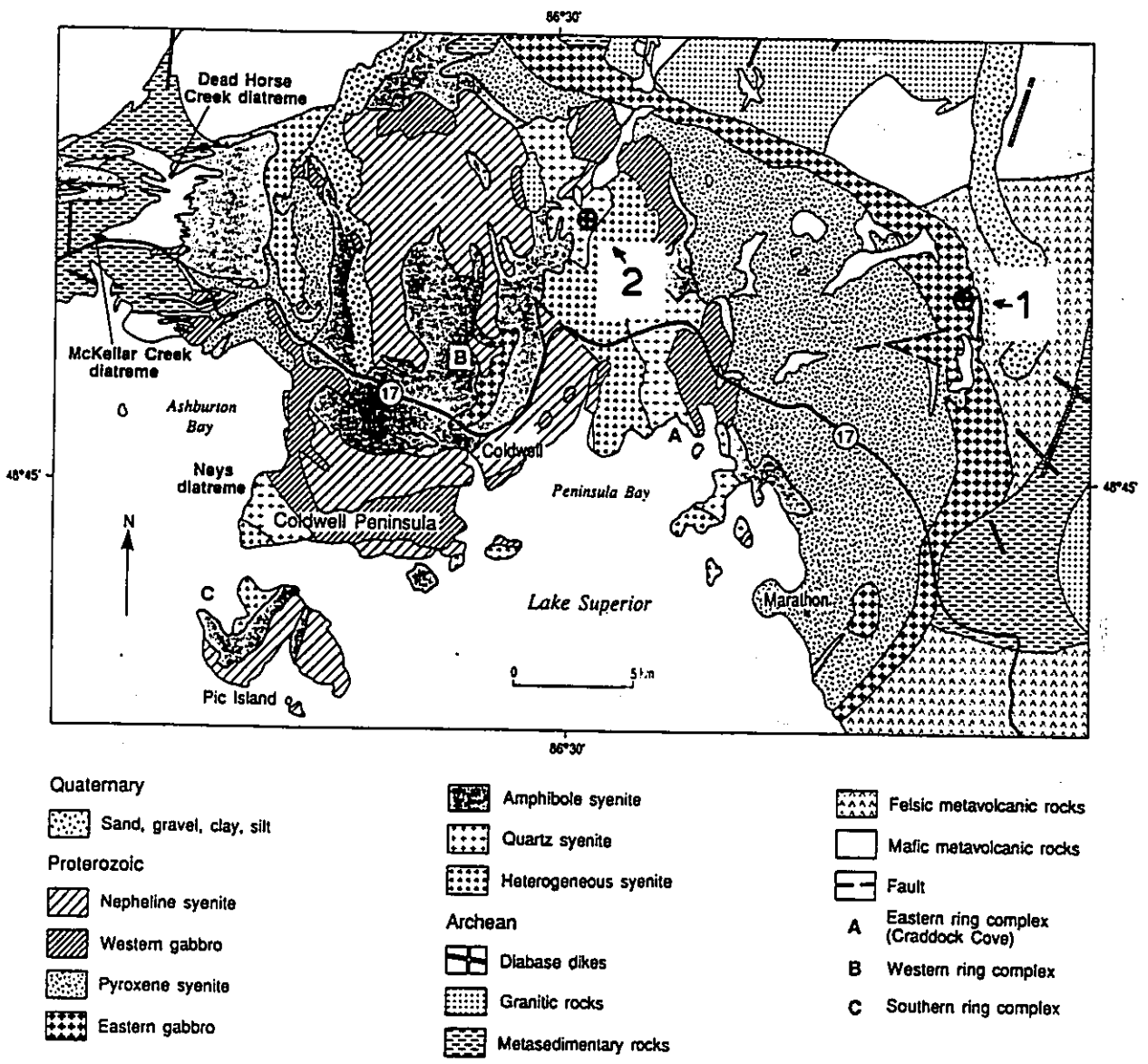


Fig. 1-2. Location of the Marathon deposit (1), and MacRae occurrence (2) in the Port Coldwell alkalic complex, after Sage (1991).

The TDL gabbro was studied in detail by Wilkinson (1983), Watkinson et al. (1983), Watkinson & Dahl (abstract 1988), Ohnenstetter et al. (abstract 1989), and Ohnenstetter & Watkinson (abstract 1991). The east central portion of the complex including the contact between the quartz syenite and eastern gabbro was mapped by Whittaker (1979). The Geordie Lake (GL) gabbro was mapped for the first time by St Joe Canada Inc. (Private Company report, 1987). The GL gabbro was studied in detail by Mulja (1989), and Mulja & Mitchell (1990; 1991).

1-4-2 General geology

The Port Coldwell alkalic complex is an arcuate body, 26 km wide (Fig. 1-2). Three intrusive centres or ring complexes (A, B, and C in Fig. 1-2), defined by crosscutting relationships and distinct magmatic geochemical trends, are recognized (Mitchell & Platt, 1982; Currie, 1980, Sage, 1991). The eastern ring complex is outlined by the eastern basal gabbro, and consists of gabbros and ferroaugite syenites (Mitchell & Platt, 1982). The western ring complex consists of alkaline gabbro and nepheline syenite (Mitchell & Platt, 1982). The southern ring complex consists mainly of quartz syenites (Mitchell & Platt, 1982). Initial Sr isotope ratios (0.70354 ± 0.00016) indicate that the Port Coldwell alkalic complex rocks were derived from

the upper mantle (Platt & Mitchell 1982). Although the complex consists predominantly of alkaline igneous rocks, some portions, e.g., the eastern border gabbro, are representative of tholeiitic igneous activity. Therefore, the genesis of the complex is somewhat enigmatic.

1-4-3 Age and tectonic setting

A precise U/Pb zircon/baddeleyite age of 1108 ± 1 Ma for gabbroic rocks of the eastern ring complex and syenitic rocks of the western ring complex, and 1099 ± 1 Ma for a granitoid rock of the southern ring complex, were determined by Heaman and Machado (1987). The main volcanism of the Keweenawan rifting event occurred between about 1110 and 1090 Ma (Sutcliffe, 1991). Therefore, the majority of Port Coldwell alkalic complex rocks were emplaced at the beginning of the main volcanism of the Keweenawan Midcontinent Rift.

The Port Coldwell alkalic complex is one of several, apparently contemporaneous, igneous intrusions that occur in a cluster north of Lake Superior (Sage 1991). The group includes the Killala Lake alkalic complex, Chipman Lake and Prairie Lake carbonatite complexes and numerous diatremes. All of the intrusions are located in close proximity to the Thiel fault which is part of the north-trending Trans-Superior Tectonic Zone (Sage, 1991). The Thiel fault was

interpreted by Cannon et al. (1989) as a transverse fault or zone of accommodation that separates two segments of the Midcontinent Rift which experienced different tectonic histories of rifting and subsidence.

1-5 Introduction to platinum-group element geochemistry

The platinum-group elements (Ru, Os, Rh, Ir, Pd and Pt) comprise the six heavier members of the iron, cobalt and nickel Groups in the periodic table. Like the elements of the first transition series the PGE exhibit a dominant siderophile and subordinate chalcophile nature. Because of their chalcophile nature they are commonly found together in magmatic sulfide deposits.

The PGE, together with gold, exhibit similar and regularly varying chemical properties. For example, the boiling and melting points of the elements decrease in the order Os, Ir, Ru, Rh, Pt, Pd and Au (see summary of properties in Table II Barnes et al. 1985). The regular order of variation of chemical properties is also observed for their geochemical behaviour. Data from magmatic sulfide deposits, when chondrite normalized, tend to exhibit fractionation in the order described above (Naldrett et al. 1979). Therefore, PGE data are commonly presented on diagrams similar to those for the rare-earth elements and the degree of fractionation is synonymous with the slope of

the pattern, e.g., increasingly positive slopes are indicative of increasing fractionation.

Recently, Fleet & Stone (1991) and Fleet et al. (1991) emphasized the differences between heavy (Os, Ir and Pt) and light (Ru, Rh, and Pd) PGE in coexisting silicate melt-alloy-sulfide melt systems.

1-6 Geochemical evolution of orthomagmatic Ni-Cu-PGE deposits

The geochemical evolution of an orthomagmatic Ni-Cu-PGE sulfide deposit can be summarized in terms of three sequential processes: 1) acquisition of ore-forming elements (OFE) by a magma, 2) partitioning of these elements into minerals or residual melt of a sulfur undersaturated magma, and 3) release of the OFE from the residual melt to a concentrating medium (sulfide melt or hydrous vapour phase), and deposition in the mineralized zone.

1-6-1 Acquisition of OFE

In general, the OFE in all PGE deposits include Cu, Ni, PGE, Au, Ag, S, Se, Te, As, Sb and Bi. It is assumed that these elements were acquired from the mantle and that the concentrations attained in mantle partial melts will be a function of the degree of partial melting and the composition of the source mantle area. It is possible that

some of the volatile elements (e.g., sulfur) were obtained from the crust during magma ascent.

1-6-2 Silicate magma-mineral partitioning

During crystallization of a sulfur undersaturated basaltic magma the OFE will be partitioned between minerals and residual melt. Those elements that are compatible in the crystallizing minerals will become depleted in the residual melt, and incompatible elements will become enriched. For example, Cu is considered to be incompatible whereas Ni is compatible to olivine, magnetite and pyroxene (Irving 1978); consequently, evolved silicate melts will have high Cu/Ni ratios. Similarly, Pd is apparently more incompatible than Pt in the early stages of crystallization of mafic magmas (Naldrett and Cabri 1976), and Pd, Pt and Au are more incompatible than Os, Ir and Ru (Barnes et al. 1985; Brugmann et al. 1987).

Recent experimental evidence for mineral-melt systems is summarized in Table 1-1. In general, clinopyroxene favours Ru over Pd, Au, Rh and Pt; spinel favours Rh and Ru over Pt, Pd and Au; all PGE are incompatible to olivine (Capobianco et al. 1990); and, alloys strongly partition Pt from Pd and Ir (Fleet et al. 1991). The experiments by Capobianco et al (1990) were run in air, or pure oxygen, and used synthetic compositions, and

although they are not representative of magmatic compositions or conditions they do demonstrate a crystal chemical control on the distribution of the PGE between spinel and magma.

Table 1-1: Experimental partition coefficients for silicate melt-mineral systems. Reference 3, Capobianco et al. 1990; reference 4, Capobianco & Drake 1990; reference 5, Fleet et al. 1991.

Mineral	Ru	Pd	Au	Rh	Pt	Ni ¹	reference
cpx	1.3	<.3	<.1	-	<1	4.3	3
olivine	0.9	.46	-	-	-	14	3
spinel ²	22	<.02	-	90	-	14.7	4
alloy		<100			>1000		5

1-Ni partitioning data from Irving 1978

2-D_{Ni} for spinel is that of magnetite.

1-6-3 Concentration of OFE

A- Silicate magma-sulfide melt partitioning

In general, the abundance of S that can be dissolved in a basaltic melt is about 0.1 wt. % (e.g., Fleet et al. 1991, Peach et al. 1990). The solubility of S decreases with decreasing temperature and activity of FeO, and increasing fO₂ (references cited p. 28-30, Naldrett 1989). Therefore, changes in any of these characteristics could result in the separation of an immiscible sulfide liquid from a previously sulfur unsaturated magma. An immiscible sulfide liquid will presumably interact or equilibrate with

residual magma and minerals, and therefore concentrate compatible OFE.

The partitioning of PGE between silicate magma and an immiscible sulfide liquid is very strong. Experimental data by Crocket et al. (in press), and Fleet et al. (1991) indicate that sulfide liquid-basalt melt partition coefficients at 1300°C and the oxygen fugacity of the iron-silica-fayalite buffer are 3720±1320 for Os, 3180±640 for Ir, 3030±980 for Au, 4950 for Pd and 4450 for Pt. Fleet et al (1991) suggested that these D values increase with decrease in temperature, f_{O_2} , S, Fe, and possibly Ni (Ni and f_{O_2} variations are coincident), and increase in total PGE abundance; however, Crocket et al. (in press) concluded that there is no significant correlation of D with sulfide phase bulk composition or total PGE content within the range of concentrations expected in mafic magmas. Higher D values for Pd (10^5) and Ir (10^4) at 1200°C (Stone et al. 1990) imply that there is a strong temperature dependance on partitioning, however, it should be emphasized that the experimental techniques used in the two experiments differ. In general, the two experiments employed different oxygen buffering techniques and, consequently, different methods for quenching the charges.

Experimentally determined partition coefficients of Ni and Cu between basaltic magma and sulfide melt are 275

and 250, respectively (references in Naldrett 1989). Peach et al. (1990) measured metal abundances in coexisting glass and sulfide droplets in MORB and determined that D_{Ni} (500-900), and possibly D_{Cu} (1383, single determination), vary with composition of the sulfide liquid and silicate melt, increasing with a decrease of mole fraction of FeS in sulfide liquid and FeO in silicate melt.

The partitioning of Ni, Cu, PGE and Au into an immiscible sulfide melt is so strong that once it forms, the silicate melt-mineral partitioning becomes insignificant. The timing of sulfide melt formation with respect to the degree of fractionation of the silicate magma is therefore an important factor in determining the composition of ore.

B- Sulfide liquid-mineral partitioning

PGE in a sulfide liquid can be fractionated in the presence of alloy phases. Recent experimental work by Fleet & Stone (1991) has shown that at 1000°C Os, Ir and Pt are strongly partitioned into an Fe alloy (D values >1000), but that Rh, Pd and Ni are much less strongly fractionated with $D(Rh)=30$ to 110 and $D(Pd \text{ and } Ni)=1$ to 2. Thus a strong fractionation of Pt from Rh and Pd will occur in systems where metal (alloy) phases are stable, whereas little fractionation of Pd from Ni will be induced by metal phases.

Partitioning of PGE between sulfide liquid and Ni-bearing troilite was also examined by Fleet & Stone (1991). They determined that Ru, Rh and, to some extent, Pd were soluble in the troilite, and only Ru was actually compatible ($D > 1$). The partitioning of Ni is comparable to that for Rh (D about 0.2).

C- Concentration of immiscible sulfide liquids

The separation of an immiscible sulfide liquid from a basaltic melt will presumably result in the formation of widely dispersed, very small droplets of sulfide liquid. Since a basaltic melt contains approximately 0.1 wt.% S prior to saturation, then formation of a sulfide-rich horizon requires significant sulfide melt migration through the silicate melt. For example, the formation of a sulfide horizon that contains 5.5 wt.% sulfides (or approximately 2 wt.% sulfur), requires accumulation of sulfur from approximately 20 times the volume of the sulfide horizon. A simple mechanism for accumulating sulfides is the settling out of the more dense sulfide liquid from silicate magma (e.g., Usselman et al. 1979).

D- Silicate magma-hydrous fluid partitioning

There is not enough known about the solubility of PGE in high temperature fluids (greater than approximately

700°C) (Mathez & Peach, 1989) nor is there sufficient knowledge about the composition of immiscible hydrothermal fluids in mafic magmas (Mathez 1989b) to be able to define the partitioning of PGE between basaltic magma and immiscible hydrous fluids. Nevertheless, there is significant evidence for the transport of Pt and Pd at intermediate temperatures (200-700°C) to form hydrothermal PGE deposits (Orlova et al., 1987; Sassini & Shock, 1990). Examples of hydrothermal PGE deposits include the platiniferous dunite pipes in the Bushveld Complex, and the New Rambler Pt-Cu-Au deposit, Wyoming where temperatures of ore-forming fluids were $600^{\circ} \pm 150^{\circ}\text{C}$ (Schiffries 1982) and at least 335°C (Nyman et al., 1990), respectively.

Despite the absence of high temperature experimental work on magma-hydrous fluid partitioning it is possible to speculate on the possible results of this process. For instance, it is doubtful that Ir will be concentrated in a mineralized zone that originated by deposition from an immiscible hydrothermal fluid for the following reasons. Firstly, Ir is apparently much less soluble than Pd, Cu and Ni in hydrous fluids. Theoretical thermodynamic calculations imply that the solubility of Pd as neutral chloride complexes at near magmatic temperature and oxygen fugacity, and $\log f_{\text{HCl}} = 100$ bars will be two orders of magnitude greater than that for Ru (and probably greater for

Ir) (Wood 1987; Mountain and Wood 1988a and b). Therefore, Ir will be very strongly partitioned from Pd, Ni and Cu by hydrothermal processes. Secondly, the Pd/Ir ratios of magma from which a volatile phase is likely to separate will also be very high (section 1-6-2). Therefore, because of the multiple stage fractionation of Pd from Ir, it is unlikely that Ir will be concentrated in this way.

Further to the calculations noted above, the concentrations of Pd and Ru in the solution will be on the order of parts per trillion (Wood 1987; Mountain and Wood 1988a and b); therefore, concentration of PGE to the ppm level would require very high fluid/rock ratios. In addition, it is likely that the presence of interstitial volatiles will lead to a continuum of reactions that span the cooling history of the mineralized zone. Therefore, fluid-rock reactions in a mineralized zone formed by hydrothermal processes should be extensive and complex.

Finally, if the PGE are carried in the fluid as Cl complexes, as is suggested by the evidence in the Bushveld and Stillwater complexes (Boudreau et al., 1986; Ballhaus and Stumpfl, 1986; Stumpfl and Ballhaus, 1986; Boudreau and McCallum, 1989), then the fluid will also carry significant Na, K and Fe (\pm Ca) (Webster and Holloway, 1988). Therefore, fluid-rock interactions resulting in the deposition of the

PGE should also result in redistribution of some of the soluble major- and trace-elements.

Chapter 2 - Petrography

2-1 Introduction

The Marathon Cu-precious metal sulfide deposit and the MacRae Cu-precious metal sulfide occurrence are hosted within the Two Duck Lake (TDL) gabbro and the Geordie Lake (GL) gabbro, respectively. The petrography of each gabbroic intrusion is described in this chapter. The goal is to define the principal processes that occurred during the crystallization of the silicate melts which might have been relevant to the genesis of sulfides and the deposition of platinum-group elements.

2-2 Geology of the Two Duck Lake intrusion (Marathon Deposit)

The Marathon deposit is hosted by gabbro at the south end of a thin intrusive body known as the Two Duck Lake (TDL) intrusion (Fig. 2-1). The TDL intrusion is continuous over 2.2 km and is less than 200m thick (Wilkinson, 1983). A detailed geological map across part of the Marathon deposit is presented in Figure 2-2, and a cross-section along line A-B (Fig. 2-2) in Figure 2-3. Samples located in Figure 2-3 are a combination of those collected on outcrop and from borehole Fleck-23. The

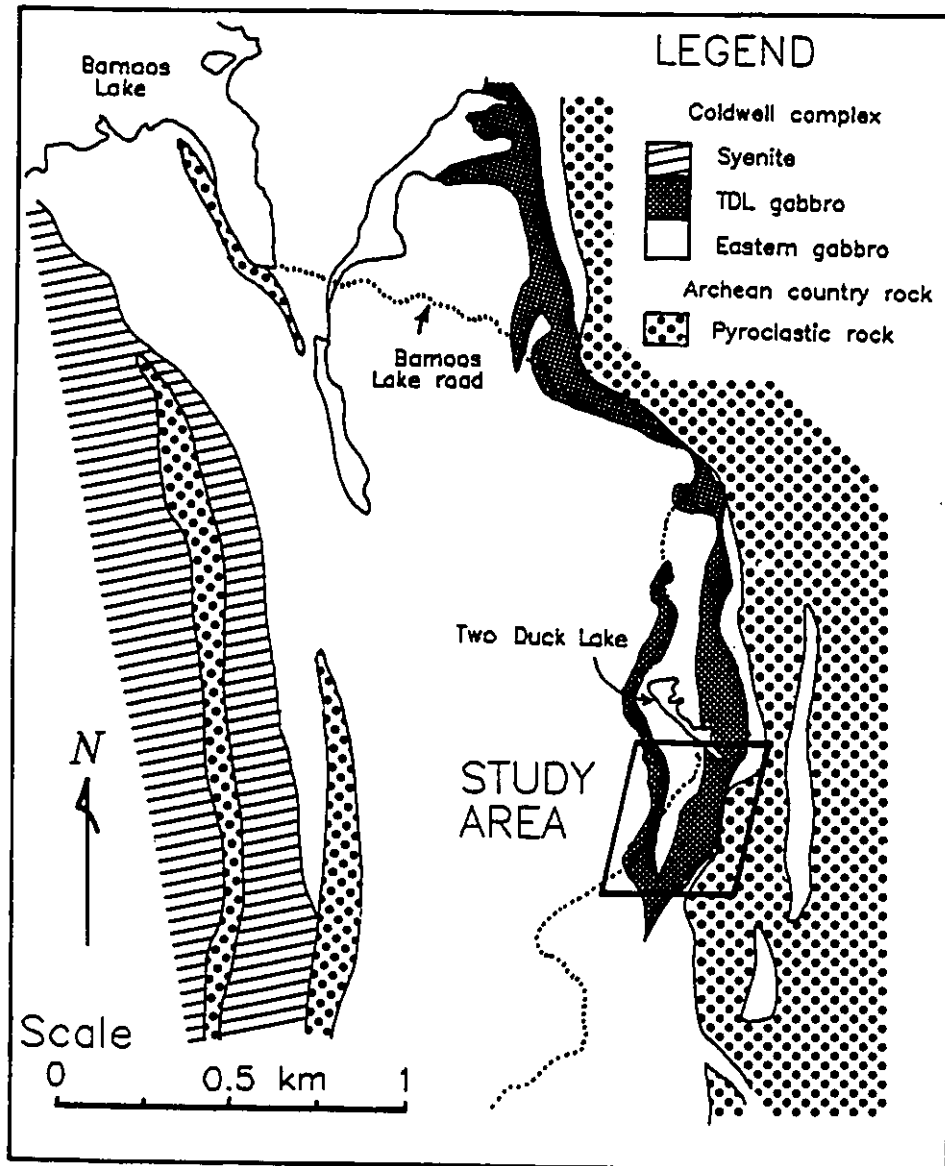


Fig. 2-1: Location of the Marathon deposit study area on a map of the Bamaos Lake area, modified after Wilkinson (1983).

Fig. 2-2: Detailed geological map of the Marathon deposit study area. A cross-section of the geology from points A to B is shown in Fig. 2-3. Eastern gabbro is also referred to as Old gabbro in the text. Property mapped with the permission of Fleck Resources Ltd.

LEGEND

ARCHEAN COUNTRY ROCK

- 1 intermediate pyroclastic rock

PORT COLDWELL ALKALIC COMPLEX

Eastern Gabbro (Old gabbro xenoliths)

- 2a fine-grained gabbro
- 2b medium-grained gabbro
- 2c layered
- 2d poikilitic
- 2e clusters of plagioclase
- 2f zoned olivine to plagioclase blebs
- 2g zoned clinopyroxene to plag blebs

Two Duck Lake Intrusion

- 3a medium- to coarse-grained gabbro
- 3b pegmatitic gabbro
- 3c poikilitic, 1 to 3 cm sized oikocrysts
- 3d poikilitic, 3 to 10 cm sized oikocrysts
- 3e very coarse-grained gabbro
- 3f xenoliths of Eastern gabbro

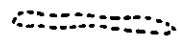
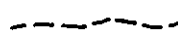


Leucogabbro

- 4 xenolith laden leucogabbro
(xenoliths of 1, 2 and 3)

Quartz-Syenite dikes

- 5 quartz syenite dikes

SYMBOLS

-  outcrop stripped of overburden
-  lithologic contacts
-  bulk sample test pits
-  quartz syenite dikes

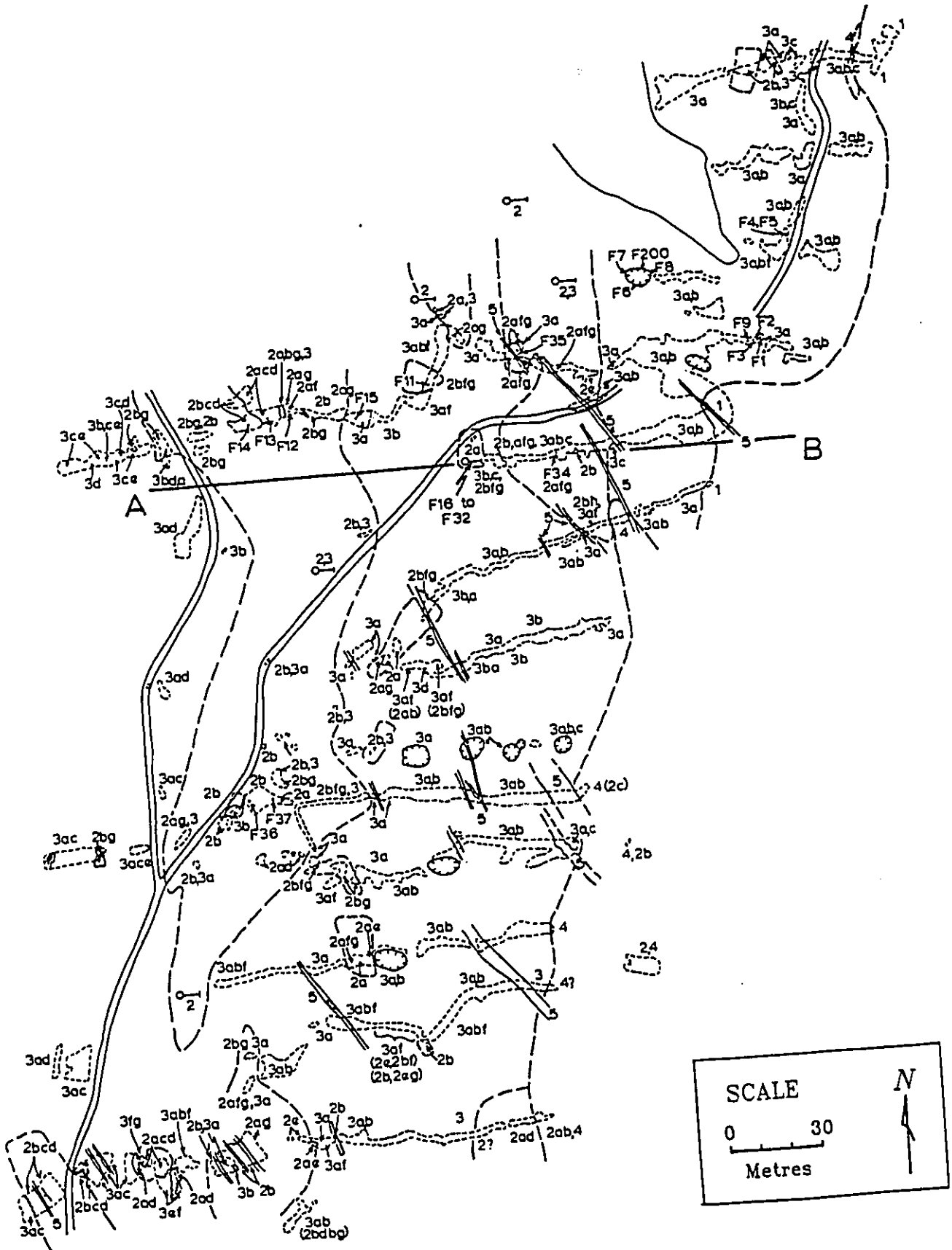
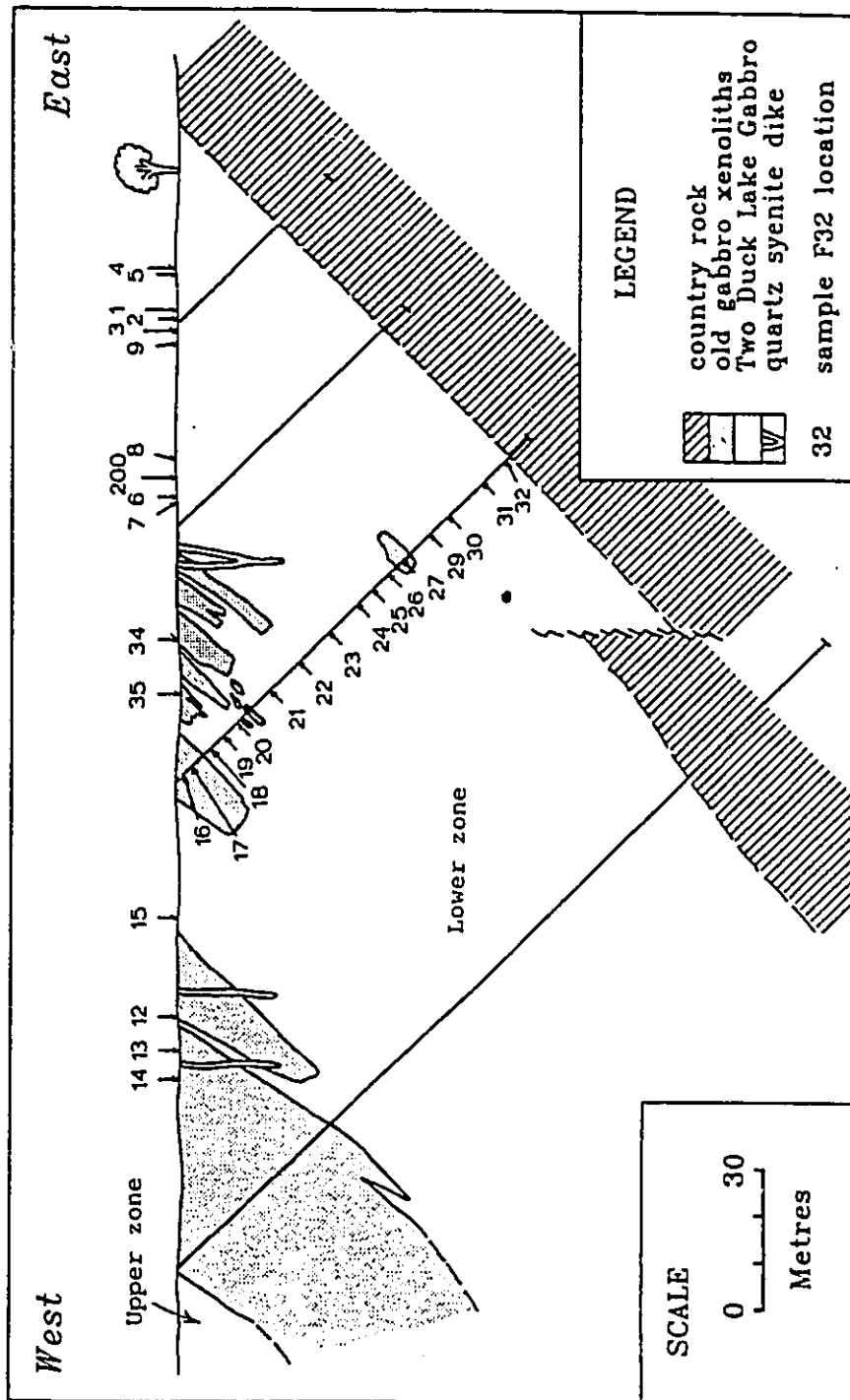


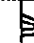

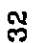


Fig. 2-3: Geological cross section of the TDL gabbro along line A to B in Fig. 2-2. Surface sample locations are projected by the respective distance from the basal contact. Drill core samples are from diamond drill hole Fleck 7.



SCALE
0 30
Metres

LEGEND

-  country rock
-  old gabbro xenoliths
-  Two Duck Lake Gabbro
-  quartz syenite dike
-  sample F32 location

surface samples in Figure 2-3 are projected from Figure 2-2 by their respective distance from the basal contact.

The TDL magma intruded along the contact between an older gabbroic body known as the Eastern gabbro and the Archean basement. The TDL intrusion-country rock contact trends north-northeast and dips moderately west. The Archean basement consists of intermediate, pyroclastic rock with rare fragments of metasediment. Weak to moderate schistosity in the pyroclastic and the orientation of flattened fragments are parallel to the intrusive contact.

A thin body of leucogabbro was emplaced along the contact between the TDL intrusion and the Archean country rock. The leucogabbro consists of numerous rounded fragments of old gabbro and rare, angular fragments of TDL gabbro. All of the above units were cut by late north-northwest trending, vertically dipping quartz syenite dykes. The dykes range in thickness from less than one to several metres. Thick dykes contain cores of granophyre.

2-2-1 Petrography

The TDL intrusion is subdivided into an upper and a lower zone. The upper zone is located west of the long, 30 to 50 m thick xenolith that strikes northerly just west of the centre of the map area (Fig. 2-2 and 2-3). The upper zone is equivalent to the unit of mottled gabbro (units 6d

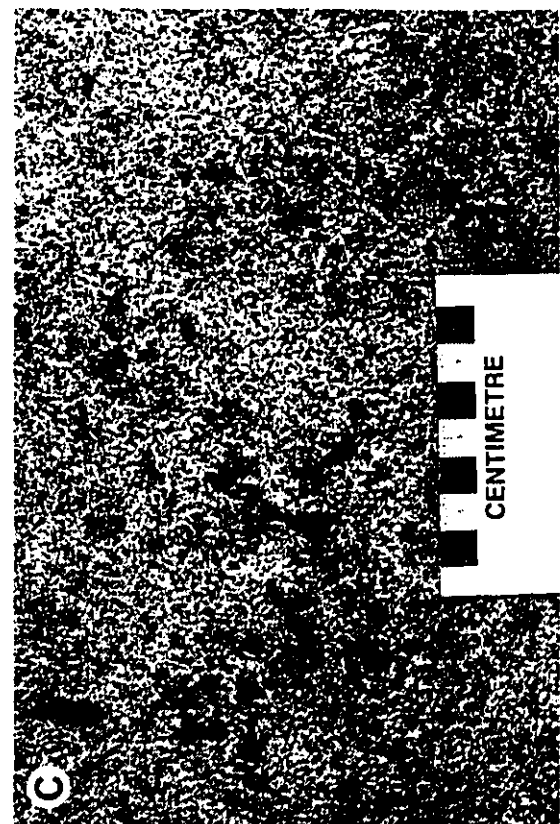
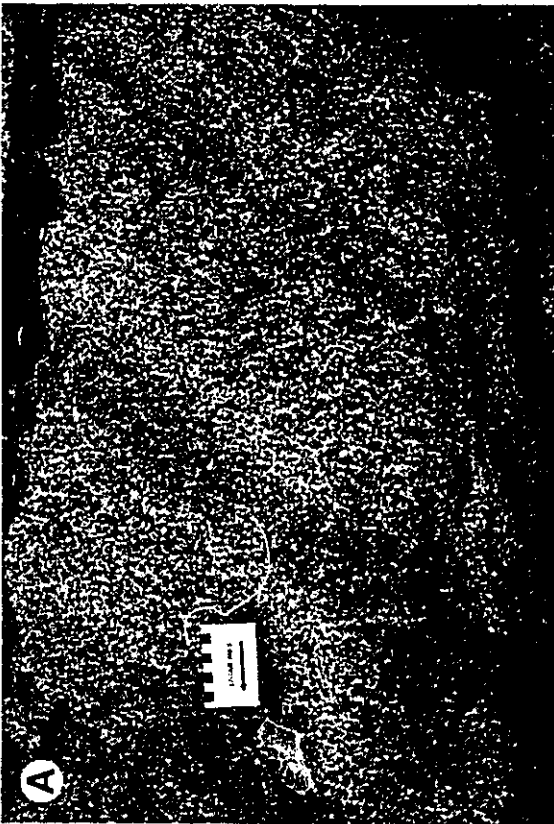
and e) and the lower zone to heterogeneous gabbro (6ac), as mapped by Wilkinson (1983). There are two major differences between the upper and lower zones. Firstly, the upper zone exhibits layering which is defined by attributes such as grain size, mineral morphology and modal abundance. In the lower zone layering is rare and where observed it is weakly defined by a gradational change in the modal composition (Fig. 2-4a). The second major difference is that sulfide mineralization occurs only within the lower zone. No mineralization has, as yet, been observed in the upper zone. The mineralized zone and layering in the upper and lower zones strike approximately north-northeast and dip moderately west approximately parallel to the intrusive contact.

A- Upper zone

The upper zone of the TDL intrusion consists of layered, poikilitic to very coarse-grained or pegmatitic gabbro. Layers strike approximately 170° , dip moderately west, and are a few to several metres thick. The contacts are gradational. Poikilitic gabbro (Fig. 2-4c) consists of medium- to coarse-grained, subhedral plagioclase and subround oikocrysts of pyroxene, olivine, and magnetite. The silicate oikocrysts range in size from one to ten centimetres. Coarse-grained to pegmatitic gabbro (Fig. 2-

Fig. 2-4: Outcrop photographs of the TDL intrusion.

- A.** Rare modal layering in the lower zone, presumably caused by partial settling out of plagioclase crystals (white) from the crystal mush and the crystallization of the resultant relatively plagioclase-poor TDL magma (see discussion in text).
- B.** Pod of pegmatitic gabbro in the lower zone. The dark interstitial minerals are predominantly pyroxene, hornblende, and spinel with lesser amounts of biotite and olivine. The major mineral and trace-element compositions of pegmatite are similar to those of the coarse-grained gabbro (see text), and the contacts between the two rock types are gradational. Therefore, this association is not intrusive in origin.
- C.** Poikilitic gabbro in the upper zone, also referred to as mottled gabbro by Wilkinson (1983). Dark spots are predominantly oikocrysts of pyroxene, and minor, subophitic spinel.
- D.** Pegmatitic gabbro in the upper zone. This pegmatite differs from that in the lower zone as it is interlayered with poikilitic or mottled gabbro.



4d) is heterogeneous with respect to grain size and consists of subhedral plagioclase and olivine, and interstitial, anhedral pyroxene, magnetite, hornblende and biotite.

B- Lower zone (TDL gabbro)

The lower zone of the TDL intrusion consists of coarse-grained, homogeneous gabbro, and sporadic pegmatitic pods (Fig. 2-4b) that may contain zones of granophyre. A precise definition of the rock name for the homogeneous coarse-grained TDL gabbro using the terminology of Streckeisen (1976) is biotite- and apatite-bearing olivine gabbronorite, however, subsequent reference to it will be simply the TDL gabbro. Note that the name TDL gabbro applies only to the coarse-grained homogeneous type and not the pegmatitic gabbro, granophyre or rocks of the upper zone. The latter rock types will be referred to using the appropriate prefix, e.g., pegmatitic TDL gabbro.

The TDL gabbro consists of subhedral plagioclase and olivine, and interstitial clinopyroxene, orthopyroxene, magnetite, sulfides, biotite, and apatite. Minor amphibole, and trace orthoclase and quartz occur locally.

The dominant texture of the TDL gabbro is that of an orthocumulate (Fig. 2-5a) (terminology of Wadsworth 1985 after Wager et al. 1960). The initial cumulus grains are plagioclase and olivine. Crystallization of intercumulus

Fig. 2-5: Photomicrographs (A and B) and scanning electron photomicrographs (C and D) of TDL gabbro.

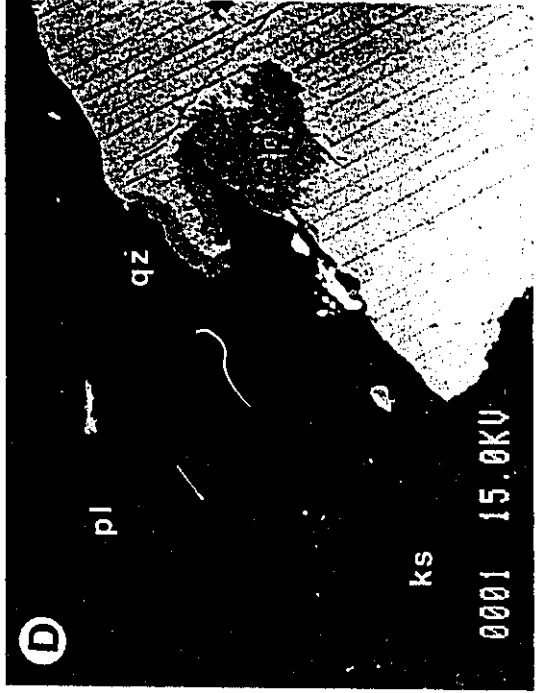
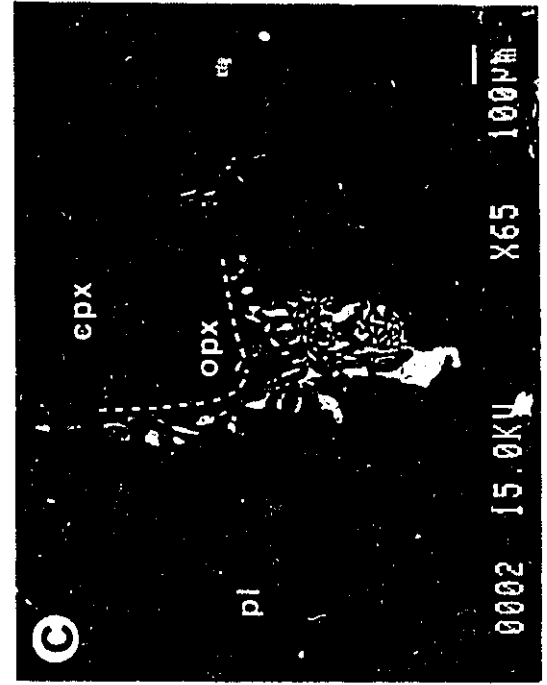
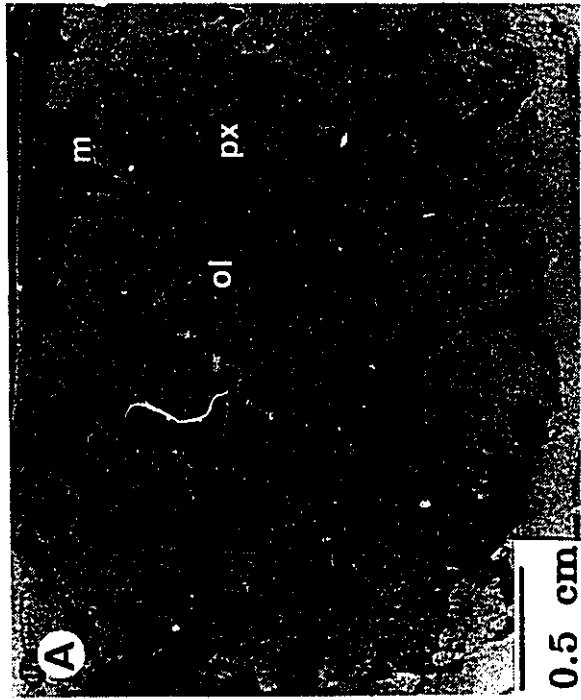
A. Typical orthocumulate texture. Plagioclase (white) and olivine (ol) are cumulus minerals, and formed a framework for crystallization of the interstitial melt. Note the post-cumulus overgrowths of olivine and the interstitial nature of clinopyroxene (px) and spinel (m). Minor interstitial orthopyroxene and biotite cannot be distinguished from clinopyroxene in this photo. From sample F1.

B. Peritectic rim of orthopyroxene on olivine. Note myrmekitic intergrowth of spinel with orthopyroxene, and exsolution lamellae of orthopyroxene in clinopyroxene. The thin, light grey rim between clinopyroxene and plagioclase in the lower left of the photo is orthopyroxene. From sample F29.

C. and D. Examination of feldspar and pyroxene compositions from a single thin section (F31) of TDL gabbro that contains a very small dikelet of contact-related granophyre that locally infiltrated between initial TDL gabbro grains. Photo C is pyroxene in gabbro near the microdikelet contact and is at chemical equilibrium. This pyroxene pair corresponds to point F31-3 of microprobe analyses in Table 2-1b. Photo D is a pyroxene pair, associated with contact-related granophyre, that is not at chemical equilibrium, and corresponds to points 31-1 and 31-2 of microprobe analyses in Table 2-1b. The pyroxene pair is not at equilibrium presumably due to interference of the normal cooling and exsolution process by the infiltration of felsic melt that crystallized granophyre.

The composition of plagioclase in D is An₃₄, Or_{4.1}, and homogeneous, but at about 100 microns from the plagioclase-K spar contact the An content decreases rapidly to An_{23.7}, Or_{3.6} at 25 microns. The composition of K-spar, 25 microns from the contact is An_{1.5}, Or_{72.7} and moving away from the contact the Or content decreases to Or₅₈, An_{3.0}. The compositions and textures are consistent with hypersolvus re-equilibration of infiltrated felsic magma and early cumulus plagioclase. This interpretation is consistent with the argument for pyroxene data.

Note myrmekitic intergrowth of spinel and orthopyroxene in C. Spinel consists of magnetite and ilmenite in the approximate proportions of 3 (magnetite) to 1 (ilmenite). Rare sulfide blebs occur in contact with the spinel.

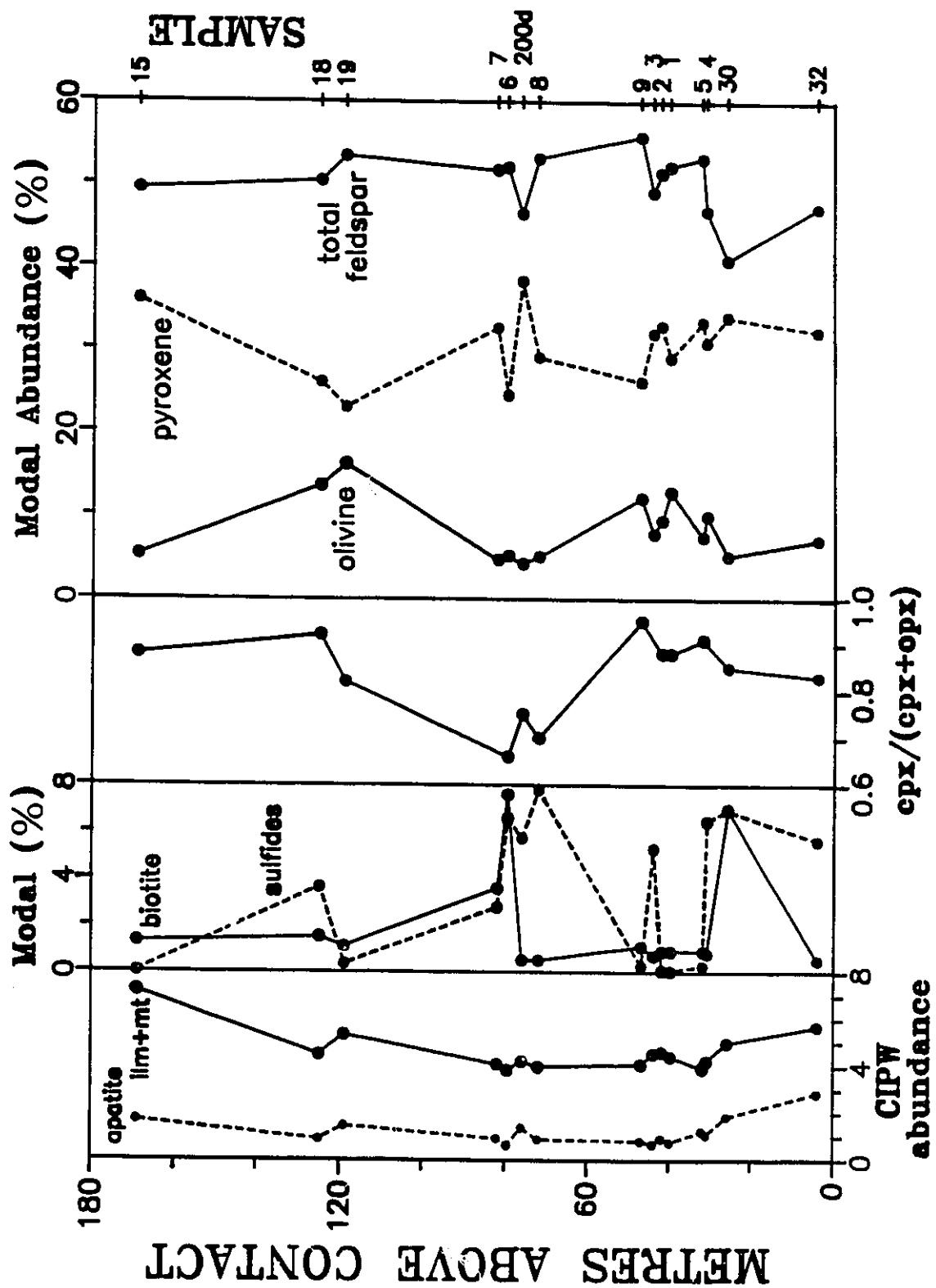


melt resulted in: a) zoned overgrowths on plagioclase, b) unzoned overgrowths on olivine, c) peritectic rims of orthopyroxene on olivine (Fig. 2-5b), and d) interstitial pyroxene, magnetite, apatite and biotite and accessory orthoclase and quartz.

Myrmekitic intergrowths of orthopyroxene and magnetite occur throughout the TDL gabbro (Fig. 2-5b and c). The intergrowths are typically associated with olivine but are also found with clinopyroxene. The magnetite consists of magnetite and exsolved ilmenite. Similar intergrowths have been observed in gabbros of the Duluth Complex (Schwartz 1930; Newhouse 1936), in olivine gabbro at Duke Island (Irvine 1974), in Lower Zone A of the Skaergaard Intrusion and in lunar breccia (Haselton and Nash 1975), however, the significance of the intergrowths is not clear.

The variation of modal composition across the lower zone, excluding pegmatite and granophyre, is shown in Figure 2-6. The abundance of apatite and ilmenite plus magnetite are calculated molecular normative abundances. In general, the section shows: a) nearly constant amounts of plagioclase, pyroxene, olivine, apatite and ilmenite plus magnetite from the base to the top, b) local increases in the amount of olivine are matched by decreasing pyroxene, c) the amount of clinopyroxene is much greater than

Fig. 2-6. Variation of modal mineral abundance across the Two Duck Lake gabbro. The distance on the left is metres above the basal contact. The abundances of apatite and spinel are normative CIPW values.



orthopyroxene, and d) the amount of biotite does not correlate with the amount of sulfides.

Pegmatitic pods (Fig. 2-4b) occur sporadically in the central portion of the TDL gabbro. Pegmatite consists of plagioclase, clinopyroxene, amphibole, magnetite, quartz, olivine, biotite, calcite and sulfides. The composition of minerals in pegmatite (see below) and their order of crystallization are generally similar to those of the coarse-grained gabbro. The pegmatite/gabbro contacts are marked by increasing grain size over a few centimetres and are not believed to be intrusive in origin.

Granophyre occurs in two settings in the TDL intrusion. The first setting is within pegmatitic TDL gabbro. This granophyre occurs in irregular shaped patches that range in size up to tens of cm across and consist of subhedral, lath-like, coarse-grained (up to 2 cm) plagioclase, subhedral to anhedral brown and olive-green amphibole, subhedral to anhedral magnetite, and interstitial graphic-textured quartz and cloudy orthoclase. Minor subhedral apatite is included in plagioclase and granophyre. Rare, partly altered, subhedral clinopyroxene with exsolved orthopyroxene lamellae are included in plagioclase laths.

The second setting for granophyre is within wispy, discontinuous felsic dikelets, approximately one by four cm in size, located in the TDL gabbro within a few metres of

the basal contact. The dikelets are evenly dispersed and make up to, approximately, 5 % of the TDL gabbro. At the thin section scale, felsic material infiltrated between initial plagioclase and pyroxene crystals of the TDL gabbro. The infiltration resulted in apparent interstitial texture for granophyre (Fig. 2-5d) and compositional disequilibrium between clinopyroxene and orthopyroxene (section 2-2-3D). Hydrous minerals (e.g., amphibole) are rare and plagioclase, olivine and pyroxenes are beautifully preserved. The felsic dikelets are interpreted to have been formed by the local intrusion of partial melt, derived from the country rock, into partly solidified TDL gabbro. The pristine nature of minerals in both the gabbro and felsic dikelets indicates that the partial melt had a very low volatile content, thereby distinguishing it from pegmatite-associated granophyre.

C- Xenoliths of eastern gabbro

Xenoliths of an early gabbroic body, referred to as the Eastern gabbro, occur sporadically in the TDL gabbro. They range in size from a few centimetres to tens of metres across, and are typically angular in form (Fig. 2-7a). The xenoliths are principally gabbroite, but they exhibit a greater diversity of rock types than does the TDL gabbro. Based on textural and compositional evidence there are at

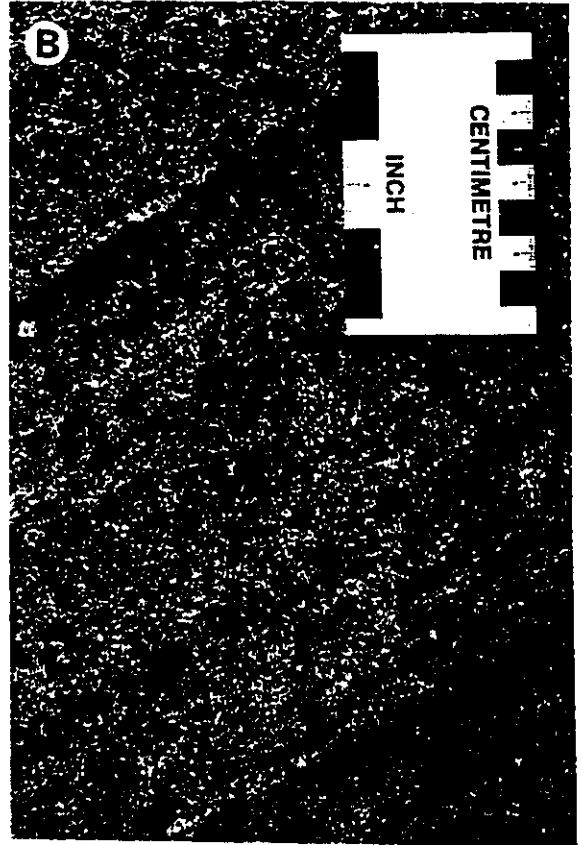
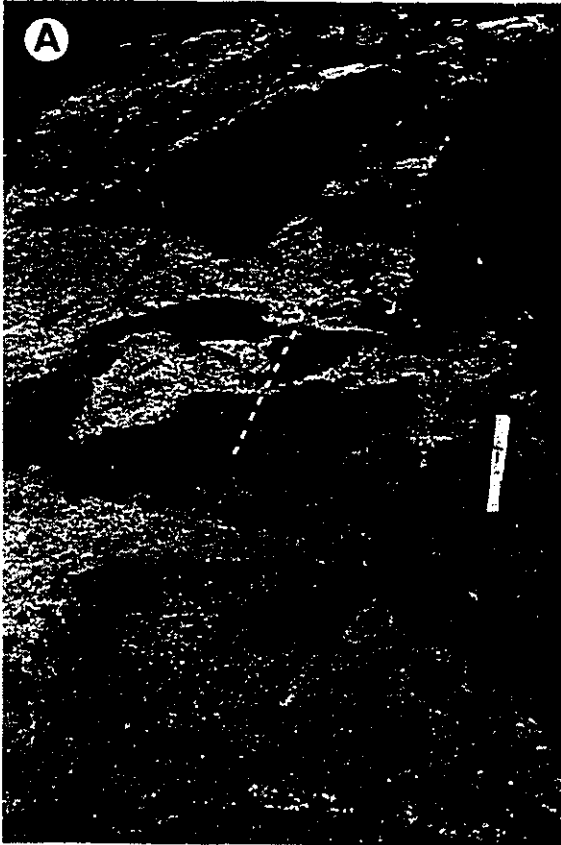
Fig. 2-7: Relationships between TDL gabbro and Eastern gabbro xenoliths.

A. Angular xenoliths (dark) in the TDL gabbro (light). The dashed line indicates layering in the xenoliths that can be traced across several adjacent fragments. The contact is between xenolith types 7 and 8 (see text), and clusters of plagioclase (type 8 gabbro) appear as white spots. This feature is evidence that xenoliths are close to their pre-TDL magma intrusion positions. This is consistent with the observed order of occurrence of xenolith types at the north and south ends of the study area.

B. Layering in fine-grained olivine gabbro with subophitic pyroxene, olivine and spinel.

C. Small, partly resorbed xenolith in the TDL gabbro. A 2 to 4 cm thick zone surrounding the xenolith is plagioclase-rich relative to the TDL gabbro. Within the plagioclase in this zone are small, rounded inclusions of clinopyroxene. This texture indicates the coincident resorption of clinopyroxene from the xenolith and crystallization of plagioclase from the TDL magma, and is consistent with other evidence that suggests the TDL magma intruded with plagioclase, and not clinopyroxene, on the liquidus. The composition of the TDL magma is not believed to have been changed significantly by the assimilation of xenoliths because the mineral compositions and trace-element concentrations of each are approximately equivalent.

D. Dikelets of TDL magma intruding xenoliths. The dikelets are commonly patchy with clinopyroxene-, olivine- or plagioclase-rich zones. The dark patches consist of clinopyroxene or olivine and are separated from the xenoliths by thin rims of plagioclase (see arrow).



least eight types of Eastern Gabbro. They are classified as follows:

- 1) fine-grained gabbronorite,
- 2) fine-grained olivine gabbronorite,
- 3) fine-grained olivine gabbronorite with poikilitic pyroxene, olivine and magnetite (Fig. 2-11b).
- 4) medium-grained mela-olivine gabbronorite,
- 5) fine-grained mela-gabbronorite,
- 6) medium-grained olivine gabbronorite,
- 7) medium-grained gabbronorite, and
- 8) fine-to medium-grained gabbro with clusters of feldspar phenocrysts.

Rocks of the TDL intrusion are easily distinguished from the Eastern gabbro xenoliths by the respective order of major mineral crystallization. In the former (both upper and lower zones) plagioclase crystallized first and forms subhedral laths, whereas in xenoliths plagioclase crystallized later and is interstitial and anhedral.

Evidence suggests that xenoliths are in close proximity to their pre-TDL gabbro intrusion location. In several instances (e.g., Fig. 2-7a) it is possible to trace layering across adjacent xenoliths. In general, this relationship holds for most of the map area as the order of occurrence of xenolith rock types from east to west is the same at the north and south ends of the map area.

Field evidence indicates that mass transfer between the TDL magma and the Eastern gabbro xenoliths occurred (Fig. 2-7 c and d); however, it is assumed to be important only on a local scale and not to affect the composition of the TDL gabbro. This is a reasonable assumption because the composition of xenoliths and TDL gabbro are similar.

2-2-2 Crystallization history

The crystallization history of the TDL gabbro follows two main paths. The most common sequence of crystallization which excludes plagioclase is illustrated, in Figure 2-8. Listed in order of first appearance the sequence is plagioclase, olivine, clinopyroxene, orthopyroxene, magnetite, biotite, orthoclase, and finally quartz. Plagioclase crystallizes throughout. Where interstitial melt was in contact with olivine, orthopyroxene crystallized prior to clinopyroxene (Fig. 2-5b).

The second possible crystallization sequence occurs locally in response to higher H₂O content. Actually, this is not a well defined path because local effects of high H₂O content are numerous, but in all cases the sequence above is interrupted in favour of hydrous minerals. Where this occurs it is possible for one or more of the following to occur: a) growth of hornblende at the expense of pyroxene (Fig. 2-9b), b) crystallization of biotite plus trace quartz

Fig. 2-8. Projection of the approximate composition of the Two Ducks Lake magma (A) into the $\text{CaSiO}_3\text{-Mg}_2\text{SiO}_4\text{-Fe}_3\text{O}_4\text{-SiO}_2$ tetrahedron (after Osborn, 1979), to show the crystallization path of residual interstitial magma. The circle at right is an enlarged inset near point A to show detail. The inferred sequence is:

from A to B, olivine;
B to C, ol+clinopyroxene;
C to D, ol+cpx+magnetite;
D to E, cpx+mt+orthopyroxene; and,
at E, cpx+mt+opx+quartz.

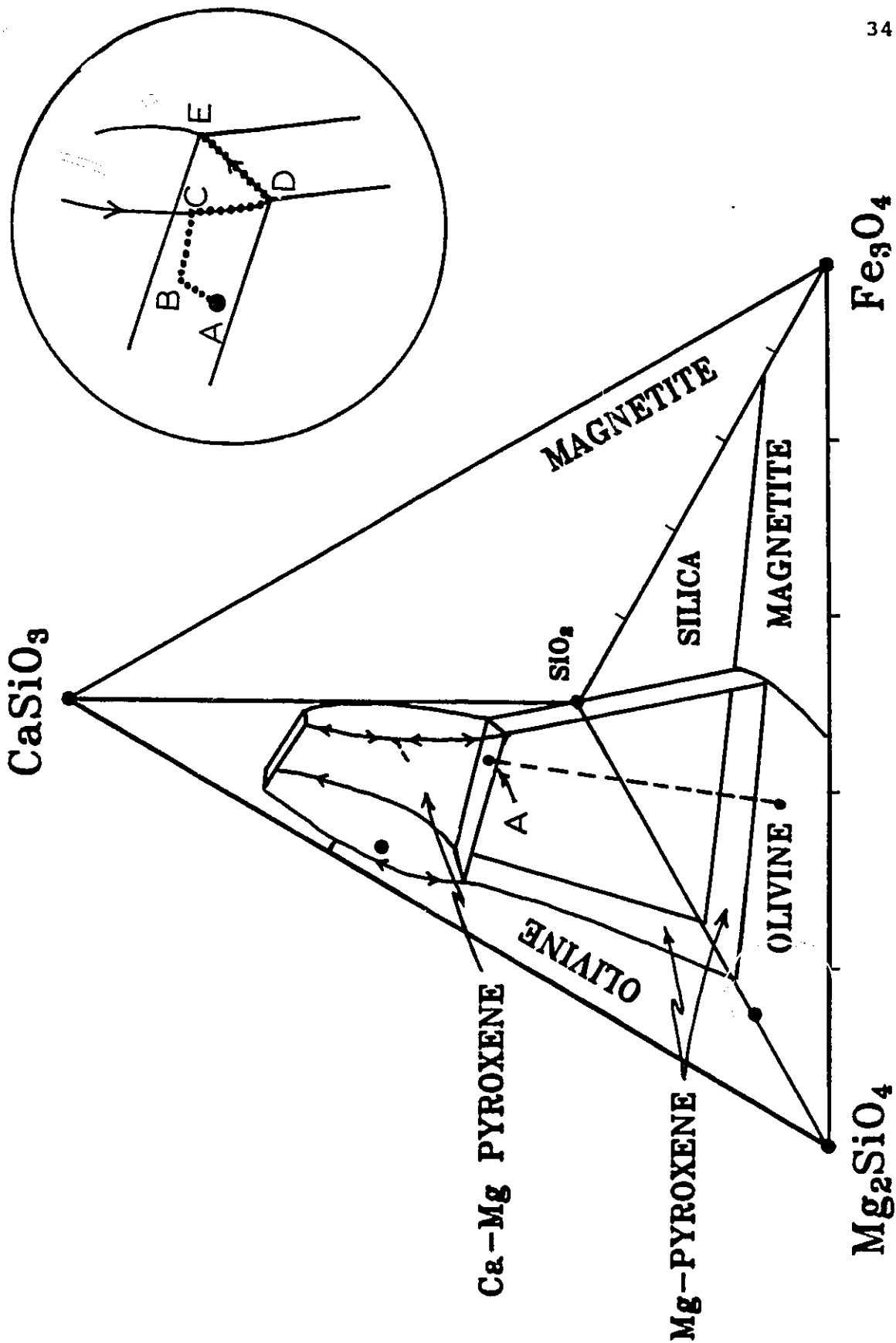
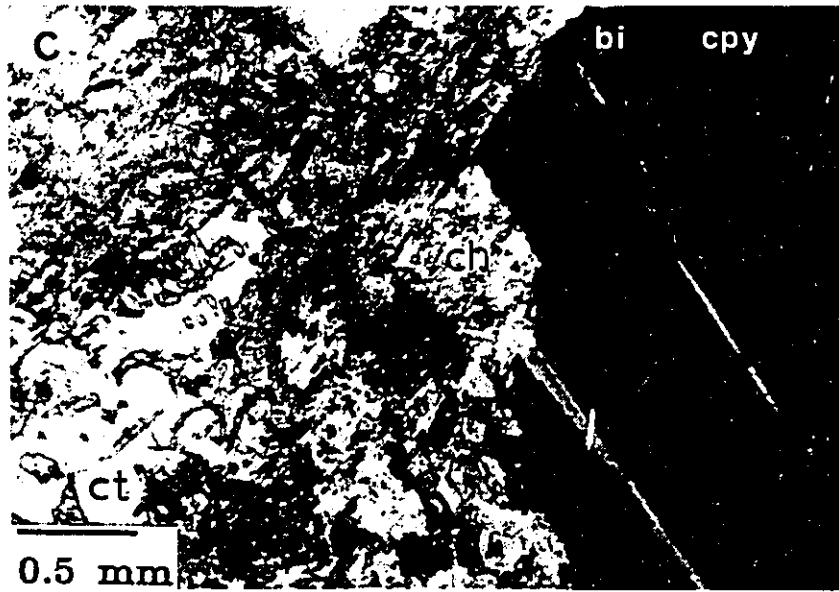
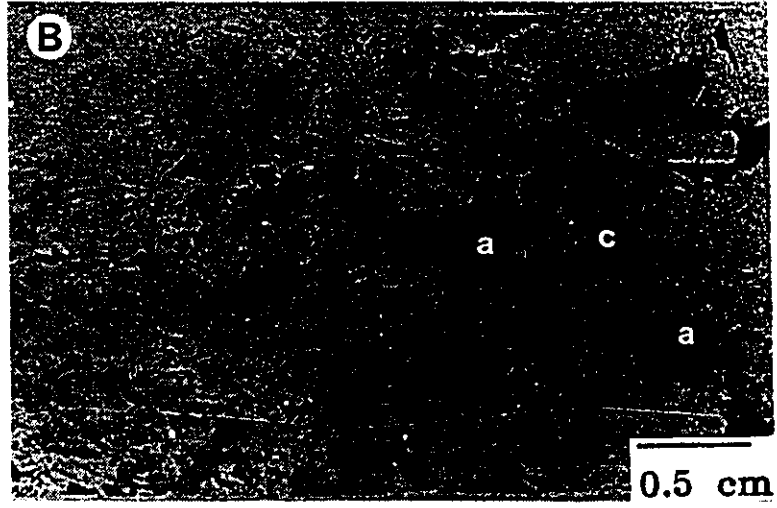
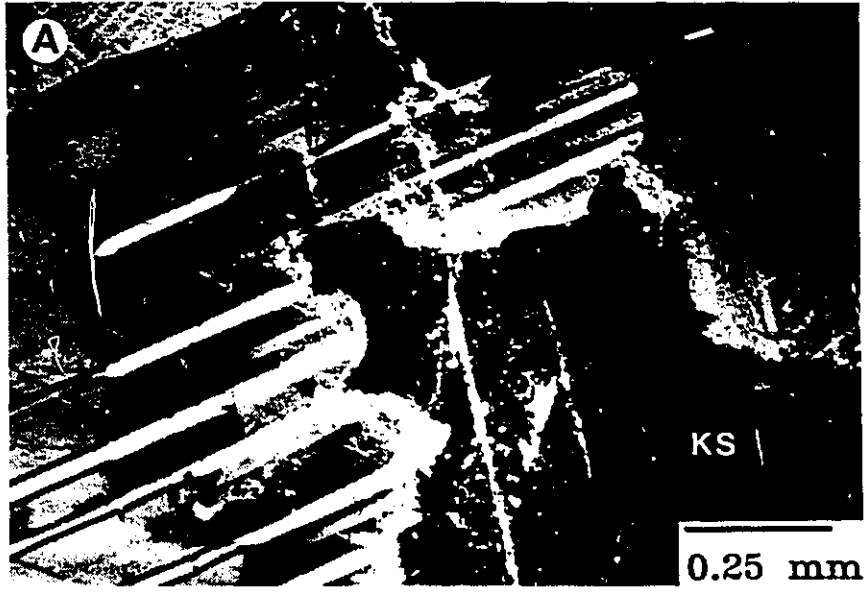


Fig. 2-9: Photomicrographs of textural relationships in TDL gabbro due to processes that occur late in the crystallization sequence of the TDL magma.

A. Resorption and recrystallization of early plagioclase by late interstitial melt that crystallized K-spar. The composition of primary plagioclase (far left) is An_{63} , that of recrystallized plagioclase (center left) An_{44} , $Or_{2.4}$, and K-spar (dark) Ab_{25} , Or_{72} . The two end-member compositions are typical of early and late stages, respectively, of fractionating magma and this feature is evidence that minor interstitial melt is migrating through the crystal pile. From sample F18.

B. Occurrence of green amphibole (a) presumably due to local elevated H_2O contents brought about by crystallization of anhydrous minerals. The majority of the thin section consists of clinopyroxene (c) and plagioclase with minor olivine, biotite and spinel, except for the two areas labelled (a) where amphibole is present. The opaques are predominantly chalcopyrite and pyrrhotite. From basal sulfide zone (F32).

C. Association of chalcopyrite (cpy), biotite (bi), chlorite (ch), and calcite (ct) in sample F20. The texture is local and is considered to represent solidification of the mesostasis. The majority of the thin section consists of pristine clinopyroxene, olivine and plagioclase and minor spinel, sulfides, amphibole and biotite. The temperatures of phlogopite and amphibole crystallization from a hydrous basaltic magma are less than $950^{\circ}C$ and $1050^{\circ}C$, respectively (see references cited in Barnes & Campbell, 1988), and these temperatures overlap the crystallization of a sulfide melt ($>900^{\circ}C$, see chapter four). Therefore, the biotite/chalcopyrite intergrowth is not inconsistent with coincident solidification of a basaltic magma and a sulfide liquid.



in place of orthoclase plus orthopyroxene, and c) local accumulation of chlorite, calcite, epidote, and biotite (Fig. 2-8c).

2-2-3 Mineral chemistry

The composition of major minerals in the TDL gabbro were determined using a JEOL model electron microprobe at the University of Western Ontario. Details of the procedure are in Appendix II. Representative analyses are listed in Table 2-1.

The variation of major mineral compositions across the section in Figure 2-6 is shown in Figure 2-9. In general, the mineral compositions are nearly constant from just above the base of the intrusion to the top of the lower zone. The deflection in mafic mineral compositions to lower MgO content at the base of the intrusion is attributed to disequilibrium crystallization brought on by assimilation of country rock (see section 2-2-3D).

A- Pyroxene

Clinopyroxene and orthopyroxene are unzoned. Representative compositions are listed in Table 2-1b and presented in Figure 2-10. The compositions of clinopyroxene lie within the field of augite. The range for Na₂O concentration in clinopyroxene (.15 to .38 wt. %) is within

Table 2-1a: Representative olivine compositions from the TDL gabbro.

sample no.	F3	1 sig	F7	1 sig	F15	1 sig	F18	1 sig
no. grains	3		3		2		3	
no. analys.	8		27		5		9	
SiO ₂	35.12	0.21	35.24	0.48	36.08	0.26	35.61	0.16
FeO	37.64	1.16	36.8	0.89	36.67	0.56	37.16	0.5
MnO	0.49	0.06	0.62	0.08	0.55	0.09	0.53	0.04
MgO	25.03	0.68	26.97	0.77	27.9	0.27	26.37	0.29
CaO	0.11	0.02	0.08	0.02	0.07	0.01	0.1	0.02
NiO	0.067	0.026	0.067	0.016	0.058	0.013	0.054	0.013
Total	98.46		99.78		101.33		99.82	

number of ions on the basis of 4 oxygens

Si	1.006		0.992		0.995		1.002	
Fe	0.902		0.866		0.846		0.874	
Mn	0.012		0.015		0.013		0.013	
Mg	1.069		1.132		1.147		1.106	
Ca	0.003		0.002		0.002		0.003	
Ni	0.002		0.002		0.001		0.001	
Forsterite	54.2		56.7		57.6		55.9	
Fayalite	45.8		43.3		42.4		44.1	

sample no.	F29	1 sig	F31-3	1 sig	F32	1 sig
no. grains	3		3		3	
no. analys.	10		13		4	
SiO ₂	34.72	0.33	34.88	0.26	33.18	0.02
FeO	38.89	0.47	40.77	0.36	47.01	0.35
MnO	0.73	0.07	0.67	0.06	0.79	0.03
MgO	24.72	0.35	23.55	0.16	17.59	0.29
CaO	0.09	0.02	0.09	0.02	0.1	0.02
NiO	0.030	0.012	0.038	0.015	n.a.	
Total	99.18		100		98.67	

number of ions on the basis of 4 oxygens

Si	0.995		0.999		1.00	
Fe	0.897		0.977		1.185	
Mn	0.017		0.016		0.02	
Mg	1.017		1.006		0.791	
Ca	0.003		0.003		0.003	
Ni	0.001		0.001			
Forsterite	53.1		50.7		40.0	
Fayalite	46.9		49.3		60.0	

Table 2-1b: Representative clinopyroxene and orthopyroxene compositions for the Two Duck Lake (F) and Geordie Lake gabbros (G).

sample no.	F18	F29	F31-1	F31-2	F31-3	F18	F29	F31-1	F31-2
grains	1	1	1	1	1	1	1	1	1
no. of anal	5	12	1	1	1	5	9	1	1
SiO ₂	53.14	52.22	51.20	51.21	52.44	50.05	51.07	51.71	50.48
TiO ₂	0.22	0.29	0.13	0.29	0.22	0.85	0.48	0.06	0.64
Al ₂ O ₃	0.79	0.89	0.15	0.22	0.59	3.16	1.51	0.36	1.11
FeO	21.78	22.06	31.88	29.61	24.06	9.54	11.38	13.57	14.26
MnO	0.59	0.64	0.80	0.83	0.72	0.22	0.39	0.30	0.43
MgO	22.66	21.15	14.63	15.48	20.69	13.25	13.55	11.19	11.52
CaO	1.23	1.66	1.15	1.71	1.28	21.50	20.86	21.75	19.64
Na ₂ O	0.03	0.01	0.00	0.03	0.03	0.37	0.25	0.15	0.35
Total	100.44	98.92	99.94	99.38	100.03	98.94	99.49	99.09	98.43
	number of ions on the basis of 6 oxygens								
Si	1.970	1.974	2.005	1.999	1.976	1.902	1.940	1.990	1.957
Ti	0.006	0.008	0.004	0.009	0.006	0.024	0.014	0.002	0.019
Al (IV)	0.030	0.026		0.001	0.024	0.098	0.060	0.010	0.043
Al (VI)	0.005	0.014	0.007	0.01	0.002	0.044	0.008	0.007	0.008
Fe	0.675	0.697	1.044	0.967	0.758	0.303	0.362	0.437	0.462
Mn	0.019	0.021	0.027	0.027	0.023	0.007	0.013	0.010	0.014
Mg	1.253	1.192	0.854	0.901	1.168	0.751	0.768	0.642	0.666
Ca	0.049	0.067	0.048	0.072	0.052	0.875	0.849	0.897	0.816
Na	0.002	0.001		0.002	0.002	0.027	0.018	0.011	0.026
Fe	34.1	35.6	53.6	49.8	38.3	15.7	18.3	22.1	23.8
Ca	2.5	3.4	2.5	3.7	2.6	45.4	42.9	45.4	42.0
Mg	63.4	60.9	43.9	46.4	59.0	38.9	38.8	32.5	34.3
sample no.	F31-3	F3	F7	F32	G2	G47	G48	G50	
no. of grai	1	2	1	1	2	2	2	3	
no. of anal	1	10	12	1	8	7	6	15	
SiO ₂	50.71	50.65	50.79	50.96	50.80	50.93	50.16	50.81	
TiO ₂	0.61	0.66	0.80	0.77	0.90	0.80	0.95	0.87	
Al ₂ O ₃	1.64	2.44	3.00	1.54	1.26	2.09	2.72	2.33	
FeO	11.58	10.20	9.56	13.37	11.94	11.16	10.86	11.93	
MnO	0.48	0.28	0.25	0.29	0.33	0.28	0.28	0.29	
MgO	12.74	13.47	13.97	12.12	12.24	12.60	12.43	12.39	
CaO	20.70	21.48	21.78	19.07	21.73	21.87	21.49	21.49	
Na ₂ O	0.27	0.38	0.33	0.24	0.38	0.39	0.39	0.39	
Total	98.73	99.56	100.48	98.36	99.53	100.12	99.28	100.50	
	number of ions on the basis of 6 oxygens								
Si	1.941	1.918	1.899	1.960	1.585	1.927	1.912	1.920	
Ti	0.018	0.019	0.022	0.022	0.021	0.023	0.027	0.025	
Al (IV)	0.059	0.082	0.111	0.040	0.415	0.073	0.088	0.080	
Al (VI)	0.015	0.027	0.021	0.030	0.367	0.020	0.034	0.024	
Fe	0.371	0.324	0.299	0.430	0.311	0.353	0.346	0.377	
Mn	0.016	0.009	0.008	0.009	0.009	0.009	0.009	0.009	
Mg	0.727	0.763	0.779	0.695	0.569	0.711	0.706	0.698	
Ca	0.849	0.874	0.873	0.786	0.726	0.887	0.878	0.870	
Na	0.020	0.028	0.024	0.018	0.023	0.029	0.029	0.029	
Fe	19.1	16.5	15.3	22.5	19.4	18.1	17.9	19.4	
Ca	43.6	44.6	44.7	41.1	45.2	45.5	45.5	44.7	
Mg	37.3	38.9	39.9	36.4	35.4	36.4	36.6	35.9	

Table 2-1c: Representative plagioclase compositions for the Two Duck Lake (F) and Geordie Lake gabbros (G).

sample no	F3b	F31f	F31f	F31f	F31f	F29a	F24d	F24b	F15-f	F15-b	F8-4	F8-4
*type	interstit	gran	gran	gran	gran	gabbro	peg	peg	gabbro	gabbro	core	cpy assoc.
SiO ₂	63.52	65.89	65.87	63.03	59.88	57.71	57.64	53.65	56.19	53.42	50.62	48.04
Al ₂ O ₃	19.13	19.23	18.77	23.24	25.08	26.54	27.39	28.67	27.96	29.31	30.86	32.21
FeO	0.16	0.15	0.11	0.28	0.28	0.38					0.50	0.47
Na ₂ O	1.48	4.41	2.93	8.27	7.21	6.72	5.82	4.73	5.33	4.55	3.76	2.66
K ₂ O	13.51	10.10	12.51	0.63	0.75	0.19	0.53	0.64	0.74	0.45	0.24	0.12
CaO	0.40	0.62	0.30	4.89	7.15	8.47	9.54	11.57	10.52	12.13	13.50	15.12
BaO		0.26	0.38	0.00	0.02	0.09					0.04	0.08
Total	98.20	100.66	100.87	100.34	100.37	100.10	100.92	99.26	100.74	99.86	99.52	98.70

number of ions on the basis of 32 oxygens

Si	11.853	11.886	11.955	11.141	10.676	10.351	10.252	9.789	10.060	9.693	9.283	8.921
Al	4.207	4.088	4.014	4.840	5.269	5.609	5.741	6.164	5.899	6.267	6.668	7.049
Fe	0.025	0.023	0.017	0.041	0.042	0.057					0.077	0.073
Na	0.535	1.542	1.031	2.834	2.492	2.337	2.007	1.673	1.850	1.601	1.337	0.958
K	3.216	2.324	2.896	0.142	0.171	0.043	0.120	0.149	0.169	0.104	0.056	0.028
Ca	0.080	0.120	0.058	0.926	1.366	1.628	1.818	2.262	2.018	2.358	2.652	3.008
Ba		0.018	0.027	0.000	0.001	0.006					0.003	0.006
Ab	13.97	38.69	25.87	72.63	61.85	58.31	50.87	40.96	45.83	39.40	33.05	23.99
Or	83.95	58.30	72.67	3.64	4.24	1.07	3.04	3.65	4.19	2.56	1.38	0.70
An	2.09	3.01	1.46	23.73	33.90	40.62	46.08	55.39	49.99	58.04	65.56	75.31

sample no	G2	G47	G47	G48	G48	G50	G50	G49	**44	G52	G58	G58
**type	core	core	rim	core	rim	core	dikelet	pod	pod	rim	replac	replac
grains							2	6		2	1	1
analys.							3	9		4	3	2
SiO ₂	55.72	55.20	56.63	54.46	55.65	55.28	69.22	69.50	63.61	65.70	64.46	65.87
Al ₂ O ₃	27.27	27.55	26.60	28.08	25.93	27.79	19.40	19.31	20.58	21.56	23.71	19.00
FeO	0.54	0.59	0.52	0.51	1.83	0.45	0.02	0.04	0.18	0.18	0.08	0.00
Na ₂ O	5.58	5.07	5.58	4.87	5.98	5.44	9.65	9.89	1.70	9.48	8.52	1.50
K ₂ O	0.10	0.31	0.59	0.44	0.28	0.14	0.73	0.03	13.35	0.02	0.14	13.92
CaO	10.49	10.53	9.23	10.96	8.46	10.94	0.49	0.33	0.14	2.68	4.72	0.13
BaO	0.03	0.01	0.08	0.01	0.08	0.03	0.00	0.00		0.36	0.01	0.60
Total	99.73	99.26	99.23	99.33	98.21	100.07	98.81	99.10	99.56	99.98	101.64	101.02

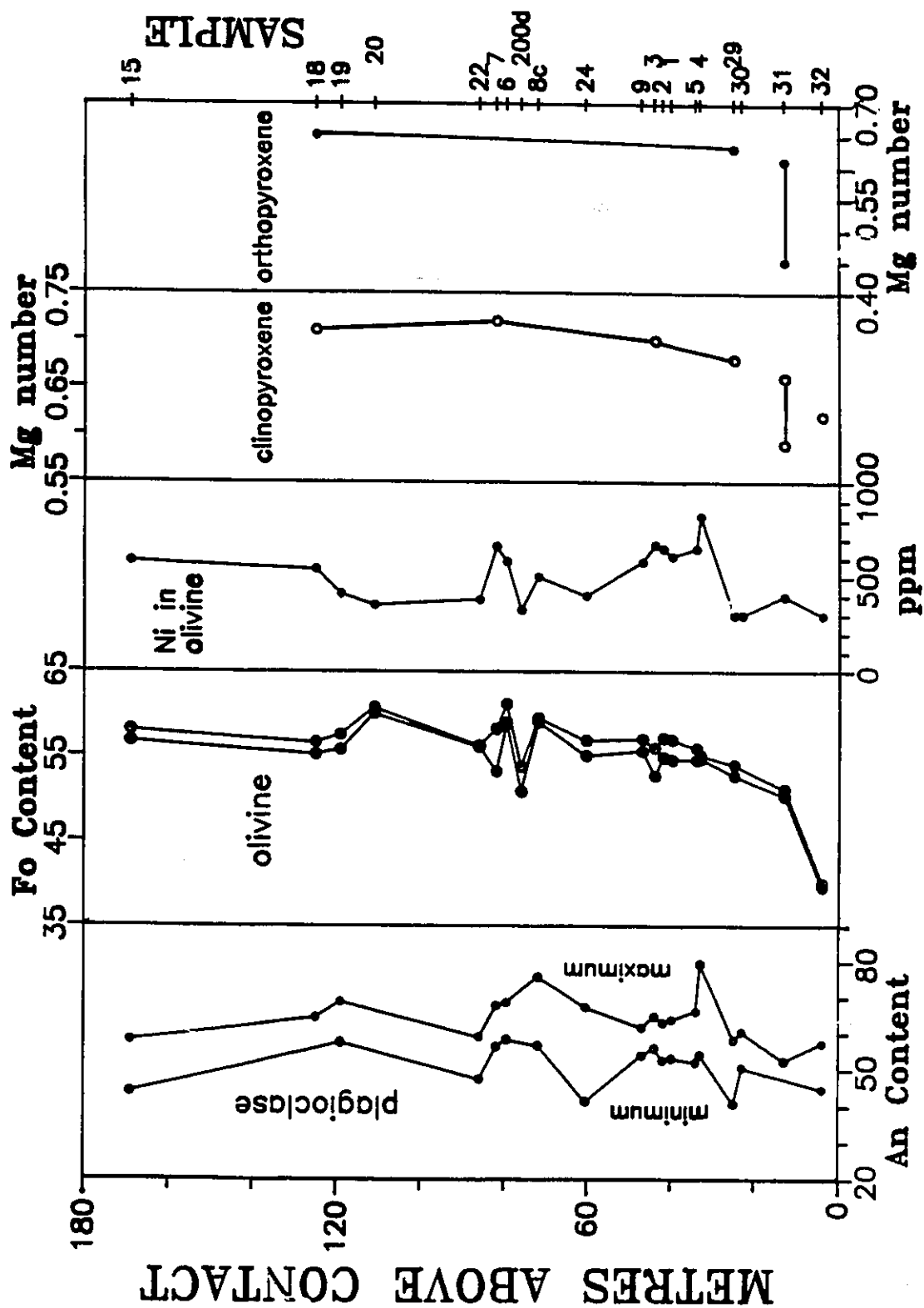
number of ions on the basis of 32 oxygens

Si	10.083	10.036	10.271	9.916	10.249	9.948	12.127	12.144	11.635	11.558	11.191	11.973
Al	5.632	5.905	5.688	6.027	5.630	5.896	4.006	3.978	4.439	4.473	4.853	4.071
Fe	0.079	0.090	0.079	0.078	0.282	0.068	0.002	0.006	0.028	0.026	0.012	0.000
Na	1.895	1.787	1.962	1.719	2.135	1.898	3.279	3.351	0.604	3.233	2.868	0.529
K	0.022	0.072	0.137	0.102	0.066	0.032	0.007	0.007	3.117	0.004	0.031	3.228
Ca	1.969	2.051	1.794	2.138	1.669	2.110	0.092	0.062	0.028	0.505	0.878	0.025
Ba	0.002	0.001	0.006	0.001	0.006	0.002	0.000	0.000	0.000	0.025	0.001	0.043
Ab	48.76	45.70	50.40	43.42	55.17	46.98	97.07	97.98	16.11	86.40	75.93	13.99
Or	0.57	1.84	3.52	2.58	1.71	0.79	0.21	0.20	83.14	0.11	0.82	85.35
An	50.67	52.46	46.08	54.00	43.13	52.23	2.72	1.81	0.75	13.50	23.25	0.66

*type refers to TDL plagioclase type: interstit, late orthoclase; gran, contact related granophyre; peg, pegmatic TDL gabbro; c.g., TDL gabbro; core, core of early plagioclase; cpy assoc., second generation of plagioclase associated with sulfides

**type refers to GL gabbro plagioclase types: dikelet, albite microdikelet; **44 is from albite pod analysed by (Mulja 1989); replace, located in recrystallized zone of primary plagioclase crystal.

Fig. 2-10. Variation of mineral compositions across the section of Two Duck Lake gabbro described in Fig. 2-6. Lines joining pyroxene compositions near the base are not drawn because they do not represent equilibrium compositions.



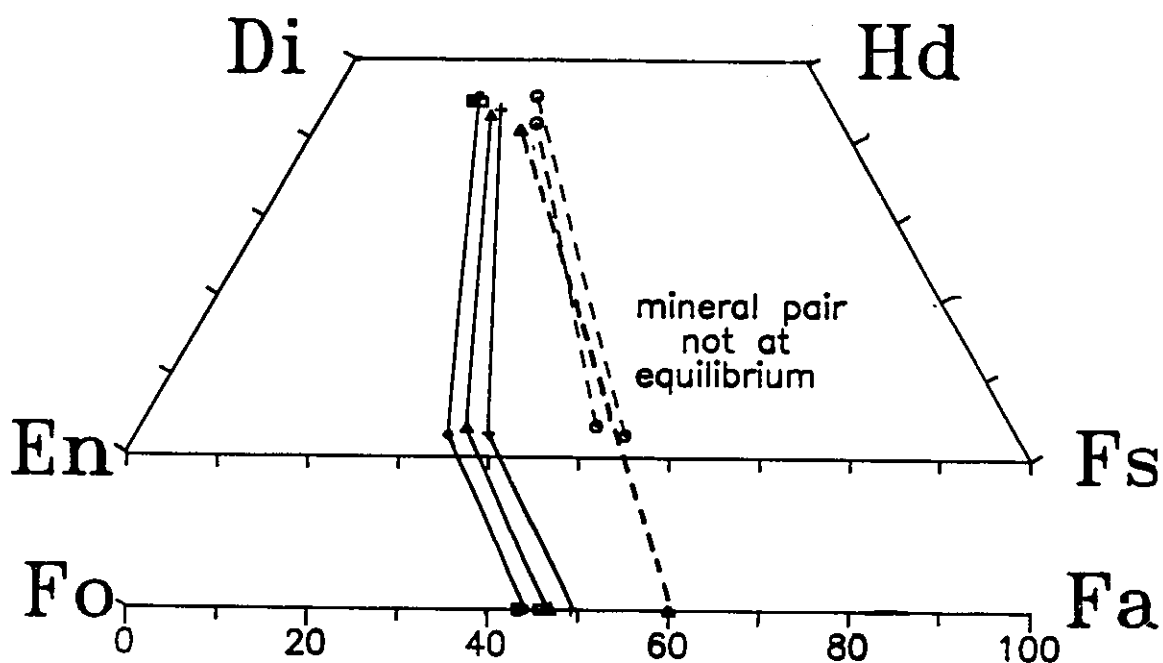


Fig. 2-11: Summary of pyroxene and olivine compositions in TDL gabbro. The compositions are listed in Table 2-1 and shown in Fig. 2-9. The dashed lines represent mineral pairs (from points F31-1, F31-2 and sample F32) not at equilibrium as indicated in Table 2-2.

the range (.1 to .65 wt. %) reported for augite in the Skaergard Intrusion (Brown 1957). The compositions of orthopyroxene (except points 31-1 and 31-2) lie within the field of hypersthene.

B- Olivine

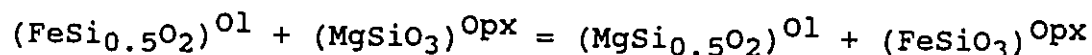
Olivine is unzoned. Representative compositions are listed in Table 2-1a and presented in Figure 2-10. The average olivine composition, excluding sample F32 for reasons discussed in section C, is 56.9 ± 2.5 % forsterite. The average Ni content of olivine for the TDL gabbro is 540 ± 140 ppm Ni. The Ni content in olivine varies by approximately 30 % across the intrusion, but does not indicate any systematic trend. The variation of Ni in olivine at the hand specimen scale is up to 30 %. The average composition and Ni content of olivine that occurs in pegmatitic gabbro (samples F22 and F24) is Fo₅₆ and 400 ppm, respectively. These values are within the range for coarse-grained gabbro.

C- Olivine-pyroxene and pyroxene-pyroxene equilibrium

At the base of the intrusion, the forsterite content of olivine and Mg number of pyroxenes, both of which are defined by the molecular proportion of $Mg/(Mg+Fe)$, are deflected to values lower than those stratigraphically

above, but the An content of plagioclase remains approximately constant throughout (Fig. 2-9). These observations are difficult to interpret and cannot be explained by simple magmatic processes. Therefore, it is likely that something unusual interfered with the normal crystallization of magma at the base of the intrusion. Recall that approximately five % wispy, felsic dikelets (contact-related granophyre) occur at the base of the intrusion. The question arises, therefore, as to what affect the intrusion of contact granophyre had on the composition of minerals crystallizing from the TDL magma. Perhaps the mafic minerals did not crystallize in equilibrium with each other.

To test the state of equilibrium of mafic minerals, Fe-Mg exchange coefficients for olivine-orthopyroxene, clinopyroxene-orthopyroxene and olivine-clinopyroxene are obtained from measured compositions of coexisting mineral pairs. The exchange of Fe and Mg between olivine and orthopyroxene will follow the equation,



and the equilibrium constant is defined by,

$$K_D = (N_{\text{Mg}})^{\text{Ol}} \times (N_{\text{Fe}})^{\text{Opx}} / (N_{\text{Fe}})^{\text{Ol}} \times (N_{\text{Mg}})^{\text{Opx}} \quad (1)$$

where $(N_{\text{Fe}})^{\text{Ol}}$ is the molecular proportion Fe/(Mg+Fe) in olivine. The above equation is simplified by assuming activity coefficients (γ) are unity, i.e., deviations of

activity and composition relations, as determined by Nafziger and Muan (1967), are minimal.

Derivation of expressions for Fe-Mg exchange between orthopyroxene-clinopyroxene and olivine-clinopyroxene will be similar to that for olivine-orthopyroxene. However, the substitution of Mg and Fe²⁺ into clinopyroxene is nonideal (Fleet 1974), and therefore the assumption of minimal deviation of activity coefficients from unity in these two systems is incorrect. Nevertheless, activity coefficients are omitted because the intent of this exercise is to determine discrepancies between samples near the basal contact and those further up section, and variations in bulk composition and temperature between the two are believed to be small. The expressions for K_D are:

$$K_D = (N_{Mg})^{Opx} \times (N_{Fe})^{Cpx} / (N_{Fe})^{Opx} \times (N_{Mg})^{Cpx} \quad (2)$$

$$K_D = (N_{Mg})^{Ol} \times (N_{Fe})^{Cpx} / (N_{Fe})^{Ol} \times (N_{Mg})^{Cpx} \quad (3)$$

The data and results of the calculations are listed in Table 2-2.

TABLE 2-2: Calculation of Fe-Mg exchange coefficients for coexisting mineral pairs. Sample 31-1, 31-2 and 31-3 are from the same thin section (F31). Analyses 31-1 and 31-2 are from a single grain of pyroxene adjacent to contact-related granophyre (shown in Fig. 2-5d).

samp	ol		opx		cpx		$K_D(1)$ ol-op	$K_D(2)$ op-cp	$K_D(3)$ ol-cp
	NFe	NMg	NFe	NMg	NFe	NMg			
F3	.458	.542			.298	.702			1.99
F7	.433	.567			.277	.723			1.99
F18	.441	.559	.350	.649	.287	.713	1.46	.746	1.96
F29	.469	.531	.369	.631	.320	.680	1.51	.805	1.88
F31-1			.550	.450	.405	.595		.560	
F31-2			.518	.482	.410	.590		.650	
F31-3	.493	.507	.394	.606	.338	.662	1.50	.785	1.90
F32	.600	.400			.382	.618			2.43

Note: K_D1 refers to Fe-Mg exchange between olivine and orthopyroxene, K_D2 to orthopyroxene and clinopyroxene, and K_D3 to olivine and clinopyroxene.

Inspection of data in Table 2-2 indicate that coexisting mineral pairs in samples well above the base are equilibrium assemblages, whereas those near the base (F32) or associated with contact related granophyre (F31-1 and F31-2) are not. Therefore, it is inferred that the deflection of mafic mineral compositions to lower MgO content is due to disequilibrium imposed by the assimilation of country rock.

The average of measured K_D values for olivine-orthopyroxene pairs in the three TDL gabbro samples is 1.49,

a value higher than experimentally determined values of 1.07 ± 0.16 (Nafziger and Muan 1967) and 1.30 (Medaris, 1969), and the natural value of 1.31 ± 0.18 obtained by Nafziger and Muan (1967) for 19 chondrites analysed by Ringwood (1961). The average measured K_D value for orthopyroxene-clinopyroxene pairs is 0.78, a value higher than the experimentally determined value of 0.73 (Kretz, 1961), and slightly higher than natural values determined for Skaergard and Bushveld (after Fleet 1974). The discrepancies between measured K_D values in this study and the experimental and natural data are probably a result of oversimplification of the equations above by deleting activity coefficients, i.e., the solutions of Fe and Mg in the minerals, particularly pyroxenes, are nonideal. Differences in temperature between the experiments quoted and the TDL gabbro cannot account for the discrepancies in K_D because the dependence of K_D on temperature in most Fe-Mg exchange reactions is small (Wood & Fraser 1977).

D- Plagioclase

Plagioclase is typically normally zoned with core to rim changes on the order of five to ten % An. Some crystals exhibit one or two abrupt discontinuities with compositional changes (normal and reverse) on the order of 3 to 5 % An. The average maximum anorthite content of plagioclase is

65.0±6.0 % and the average minimum is 51.9±6.4 % An. The composition of plagioclase in pegmatite (sample F24) is within the range for coarse-grained gabbro.

There are two distinct periods of plagioclase growth separated by a period of resorption. The early plagioclase consists of normally zoned, subhedral crystals that are locally resorbed. Evidence for resorption includes embayments that cut early zoning (see map of zoned plagioclase in Chapter four, section 4-4-1, Fig. 4-1d) and rounded, early plagioclase crystals included in late plagioclase. The late plagioclase is invariably more calcic (by up to ten An mole %) than early plagioclase. The two most calcic plagioclase compositions in Figure 2-9 (samples F4 and F8c) are from late plagioclase. The event of resorption and late plagioclase growth has special inferences (section 2-2-3E) with regard to the intrusive history of the TDL magma. There is also a spatial association between late plagioclase and sulfides that is examined further in section 4-4-1.

E- Significance of two generations of plagioclase

As noted above, there were two distinct periods of plagioclase crystallization separated by an episode of resorption. Early plagioclase is less calcic than the late plagioclase by approximately 10 % An. Late plagioclase is

more calcic than any other plagioclase analyzed in the TDL gabbro. The period of resorption corresponds to an event that resulted in disequilibrium between plagioclase and melt. Two possible causes for such an event are: (a) the movement of crystals into contact with a hotter, more calcic melt, or (b) lowering of the liquidus in the solid solution series.

Possible movement of early plagioclase into a hotter, more calcic melt could have been accomplished by either mixing in a stratified magma chamber, or by mixing of the initial crystals with an influx of more primitive melt. If such an episode of mixing occurred, it probably happened prior to intrusion of TDL magma.

Two possible mechanisms for lowering the liquidus are: (a) a sudden increase in the water content of the magma, and (b) a decrease in confining pressure. It seems unlikely that either a gradual or rapid increase in water content could be responsible for lowering the liquidus in this case. A gradual increase in water content by continued crystallization of anhydrous minerals cannot explain the rapid transition inferred by the 10 % jump in An content, and a sudden influx of water would presumably result in pegmatitic textures. It is more likely that the liquidus was lowered by a decrease in the confining pressure. Therefore, the two generations of plagioclase could

represent crystallization in a deep and shallow magma chamber, respectively, with resorption occurring at the time of magma ascent. The problem with this model is that, contrary to experimental evidence, the late plagioclase in the TDL gabbro is considerably more calcic than the early plagioclase. Experimental work by Smith & Lofgren (1983) showed that increasing the temperature (believed to be similar to decreasing the pressure) will account for discontinuities in plagioclase zonation, but that later plagioclase has lower An contents than initial plagioclase. An alternative explanation for reverse zonation in plagioclase following an intrusive event was proposed by Wiebe (1968). Wiebe inferred that plagioclase crystallizes from a slightly supercooled liquid, so that with intrusion, the amount of supercooling decreased to a point where some resorption occurred. Then, after sufficient cooling the liquid again crystallized plagioclase, but it was more calcic than that prior to intrusion. It should be emphasized that, in this case, there is a range of temperatures over which a single magma composition can crystallize a range of plagioclase compositions.

In conclusion, the interpretation for two generations of plagioclase in the TDL gabbro is equivocal. However, both explanations proposed above are directly related to the timing of intrusion of the TDL gabbro. This

is a significant observation because late plagioclase is intimately associated with sulfide mineralization, and, therefore, it provides direct evidence as to the timing of mineralization. The implication is that a sulfide melt must have been present in the crystal mush at the time of emplacement of the TDL gabbro.

2-2-4 Classification of TDL magma

The Port Coldwell alkalic complex is widely believed to be composed of alkaline intrusive rocks and yet the TDL gabbro does not exhibit features typical of alkaline rocks. Admittedly, the determination of parental magma types for mafic intrusions is difficult due primarily to the effects of crystal accumulation and fractionation in the magma chamber. However, alkaline intrusive rocks can be distinguished from subalkaline rocks by such characteristics as the mineral crystallization history and the composition of the residual magma.

Alkaline igneous rocks are defined by Fitton and Upton (1987) as those which have higher concentrations of alkalis (Na_2O and K_2O) than can be accommodated in feldspars alone, the excess appearing as alkali-rich phases (e.g., feldspathoids, sodic pyroxenes and sodic amphiboles). A result of high alkali content is reduced silica and/or alumina activity in the magma. A magma with low silica

activity will crystallize nepheline, but not orthopyroxene or quartz, and hence generate the major difference between alkalic and tholeiitic magmas. The degree of silica saturation forms the basis of the basalt tetrahedron (Yoder and Tilley 1962, p. 350) and the boundary between alkalic and tholeiitic magmas. The boundary plane (the critical plane of silica undersaturation) is a thermal divide in that fractional crystallization of a magma with a composition that lies on either side of the divide will drive the composition of that magma away from the plane (Yoder and Tilley 1962). Therefore, tholeiitic or alkalic magmas will retain their parental characteristics during fractional crystallization. The importance of the thermal barrier in distinguishing between alkalic and tholeiitic intrusive rocks was highlighted by Irvine (1974). The possible conversion of magma types by separation (or addition) of major mineral phases was ruled out as a viable process by Yoder and Tilley (1962), except by the addition or subtraction of amphibole. Another process for magma conversion is contamination by crustal rocks.

The parental magma that crystallized the TDL gabbro was probably an olivine tholeiite. The tholeiitic nature is based on the following petrographic observations:

- a) the crystallization sequence in order of first appearance is plagioclase, olivine, clinopyroxene, orthopyroxene, and magnetite,
- b) the residual melt crystallized granophyre,
- c) the reaction of olivine with melt to form orthopyroxene,
- d) the absence of sodic amphibole or pyroxene, and
- e) the absence of primary amphibole, except in pegmatite.

There is no petrographic evidence for early amphibole fractionation. Therefore, the possibility that the original magma was alkalic and was subsequently converted to a tholeiitic melt by amphibole separation is unlikely. The possibility that the conversion of magma types occurred by contamination with country rock is beyond the scope of this thesis.

2-2-5 Emplacement of the TDL magma

An interpretation for the emplacement and subsequent crystallization of the TDL magma to form the lower zone of the TDL intrusion must account for the following:

- a) predominant orthocumulate texture of the TDL gabbro,
- b) rare modal layering,
- c) a nearly constant major mineral composition from the base to top of the lower zone,
- d) common textural features of the coarse-grained TDL gabbro throughout, and

e) the presence of pegmatite and granophyre,

A satisfactory model to explain the intrusive history and account for these observations is that the lower zone of the TDL intrusion was emplaced as a crystal mush consisting of plagioclase \pm olivine and silicate melt. The plagioclase crystals \pm olivine formed a framework for crystallization of the interstitial melt and there was little, if any, crystal-free magma in the chamber. There was some minor settling of plagioclase to form rare modal layering. Some interstitial melt migrated through the crystal pile to form granophyre. Migration of volatiles out of the granophyre-forming melt into nearby crystal mush enabled the formation of pegmatite.

2-3 Geology of the Geordie Lake gabbro (MacRae occurrence)

Mineralization at the MacRae occurrence is hosted by the GL gabbro and neighbouring quartz monzonite. The mineralized zone consists of several lenticular zones of disseminated chalcopyrite that are located close to the quartz monzonite contact and trend approximately north, parallel to the contact. A geological map (after Bond Gold Canada Inc., Private Company Report, Assessment File Review Office, Thunder Bay, Ontario) showing all sample locations is found in Figure 2-12. A cross-section along borehole #7 (Fig. 2-12) is located in Figure 2-13.

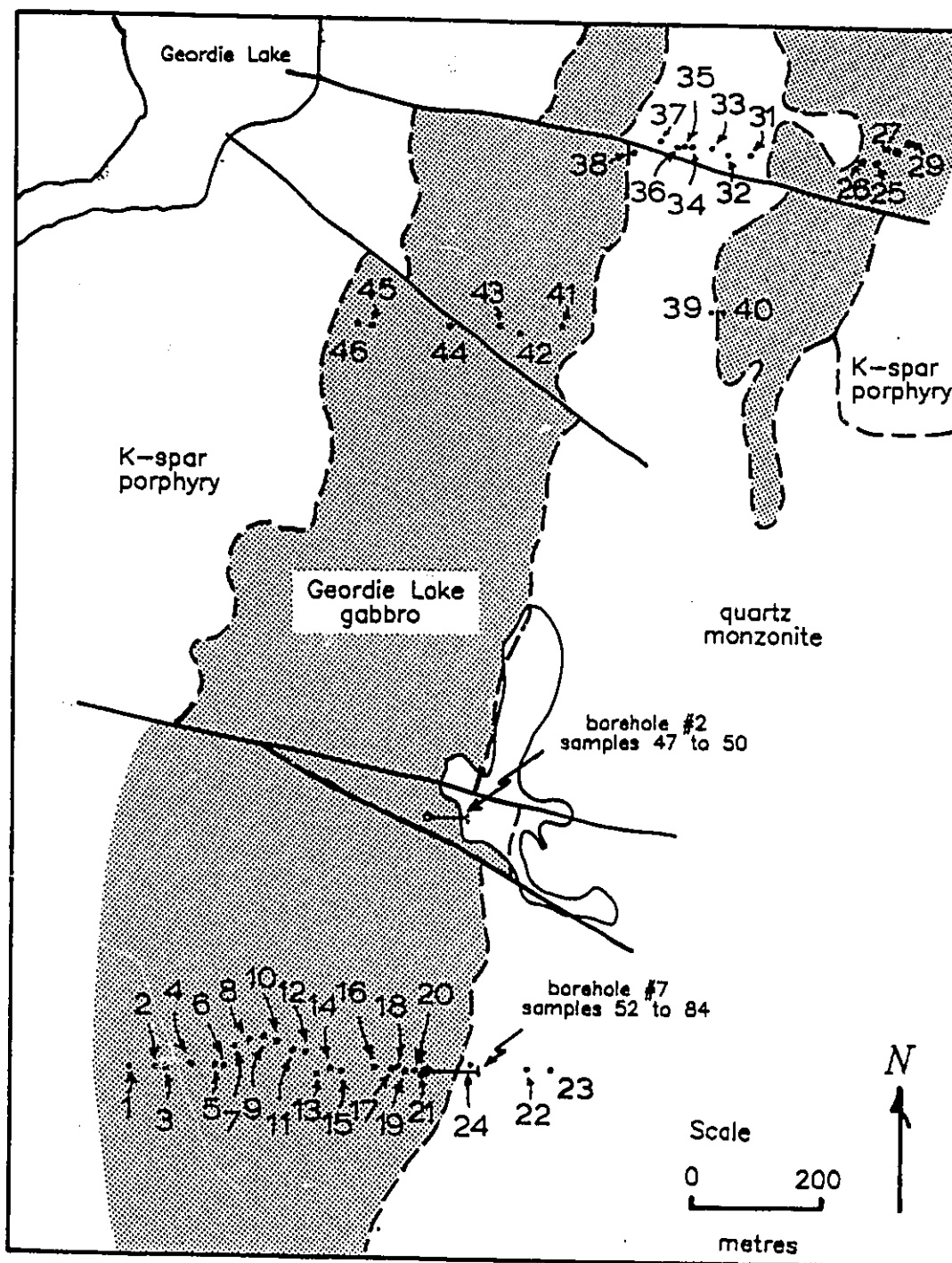
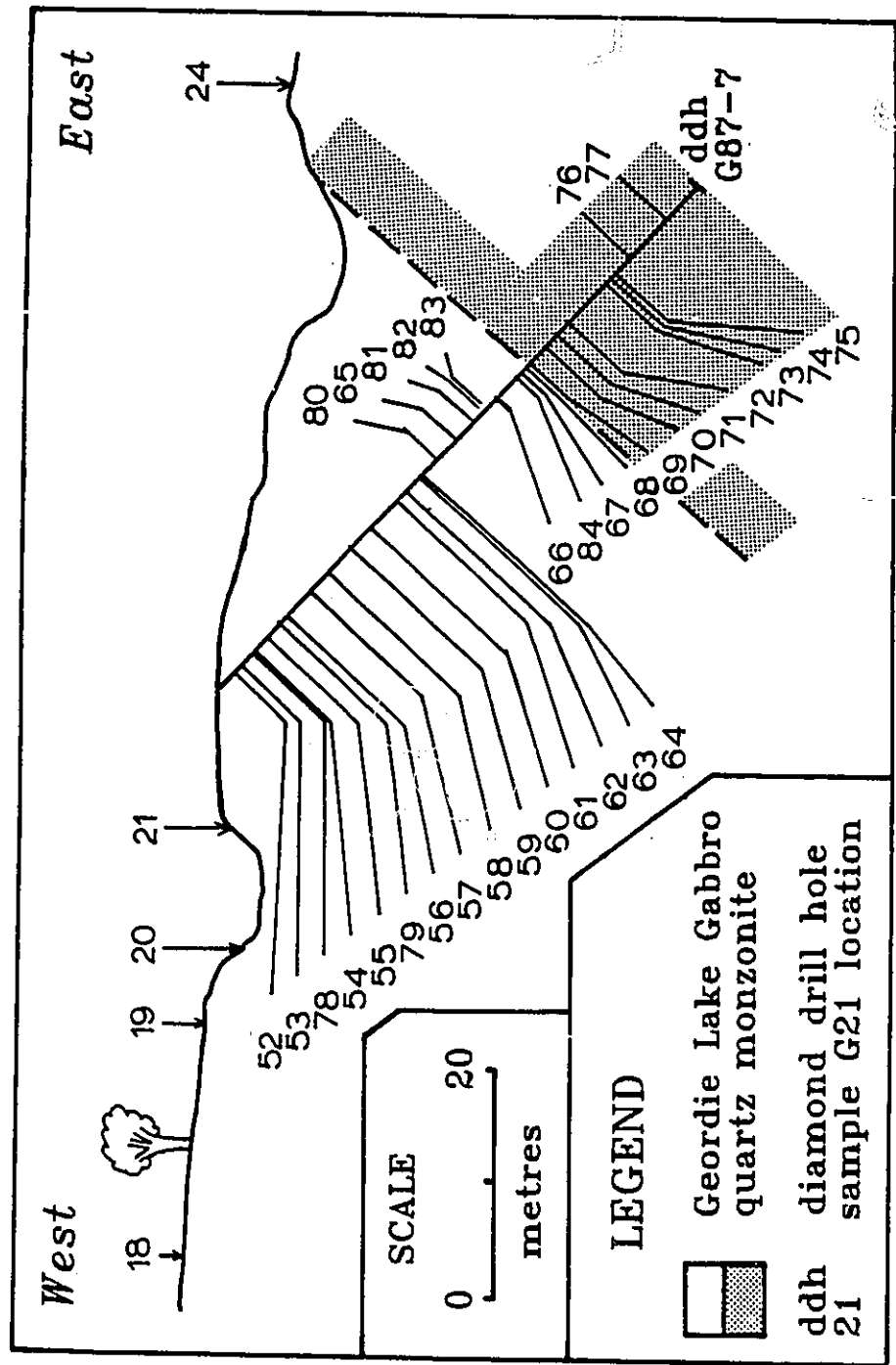


Fig. 2-12: General geology and sample location map of the MacRae occurrence, modified after St. Joe Canada Inc. (now Bond Gold). Samples are referred to with a G prefix in the text.

Fig. 2-13: Geological cross section of the Geordie Lake gabbro along borehole 7 located in Fig. 2-12. Borehole and surface samples are located in Fig. 2-12 and are referred to with a G prefix in the text.



Layering in the GL gabbro has not, as yet, been recognized, and therefore the strike and dip of the intrusion is not positively determined.

2-3-1 Petrography of the GL gabbro

The GL gabbro is subdivided into mineralized and unmineralized zones, based on several significant petrographic features. In general, gabbro in the mineralized zone is heterogeneous with respect to grain size and modal composition and contains abundant albitic pods and microdikelets, whereas gabbro in the unmineralized zone is relatively homogeneous.

Clues as to the origin of sulfide mineralization are sought by examining the mineralized and unmineralized zones separately to recognize fundamental processes that may be related to the deposition of sulfides. Relationships between the albitic pods and the GL gabbro will be emphasized since there is a spatial association between the former and sulfide mineralization.

A- Unmineralized zone

A section of unmineralized gabbro, believed to be located stratigraphically above the mineralized zone, was examined and 18 representative samples (G1 to G18, Fig. 2-12) were collected. The CIPW normative abundance of

minerals is relatively constant in this section (Fig. 2-14). The normative as opposed to the modal composition is shown because the latter is difficult to determine due to widespread deuteric alteration. The norms are in approximate agreement with the estimated mode, but there are some exceptions, e.g., no olivine has been identified in the section.

GL gabbro in the unmineralized zone is coarse-grained and homogeneous, and consists of subhedral plagioclase, euhedral apatite, subhedral to skeletal magnetite and anhedral, interstitial clinopyroxene (Fig. 2-15a). The order of crystallization is plagioclase, apatite, magnetite and clinopyroxene. No orthopyroxene has been identified. The strict classification of the GL gabbro in this zone according to the scheme of Streckeisen (1976) is apatite-bearing magnetite gabbro.

Plagioclase in the unmineralized gabbro forms coarse-grained, weakly zoned, lath-like crystals up to 1 cm in length. The plagioclase crystals are commonly aligned (Fig. 2-15b) and form a lineation that trends westerly and plunges moderately west.

Apatite crystals are euhedral and have 0.1 to 0.2 mm cross sections. Apatite is ubiquitous and is typically included in magnetite, fresh clinopyroxene, hornblende and albitic plagioclase rims.

Fig. 2-14: CIPW normative mineral abundances in Georgie Lake gabbro from the unmineralized zone. Samples 1 to 18 are located in Fig. 2-12, and are referred to with a G prefix in the text.

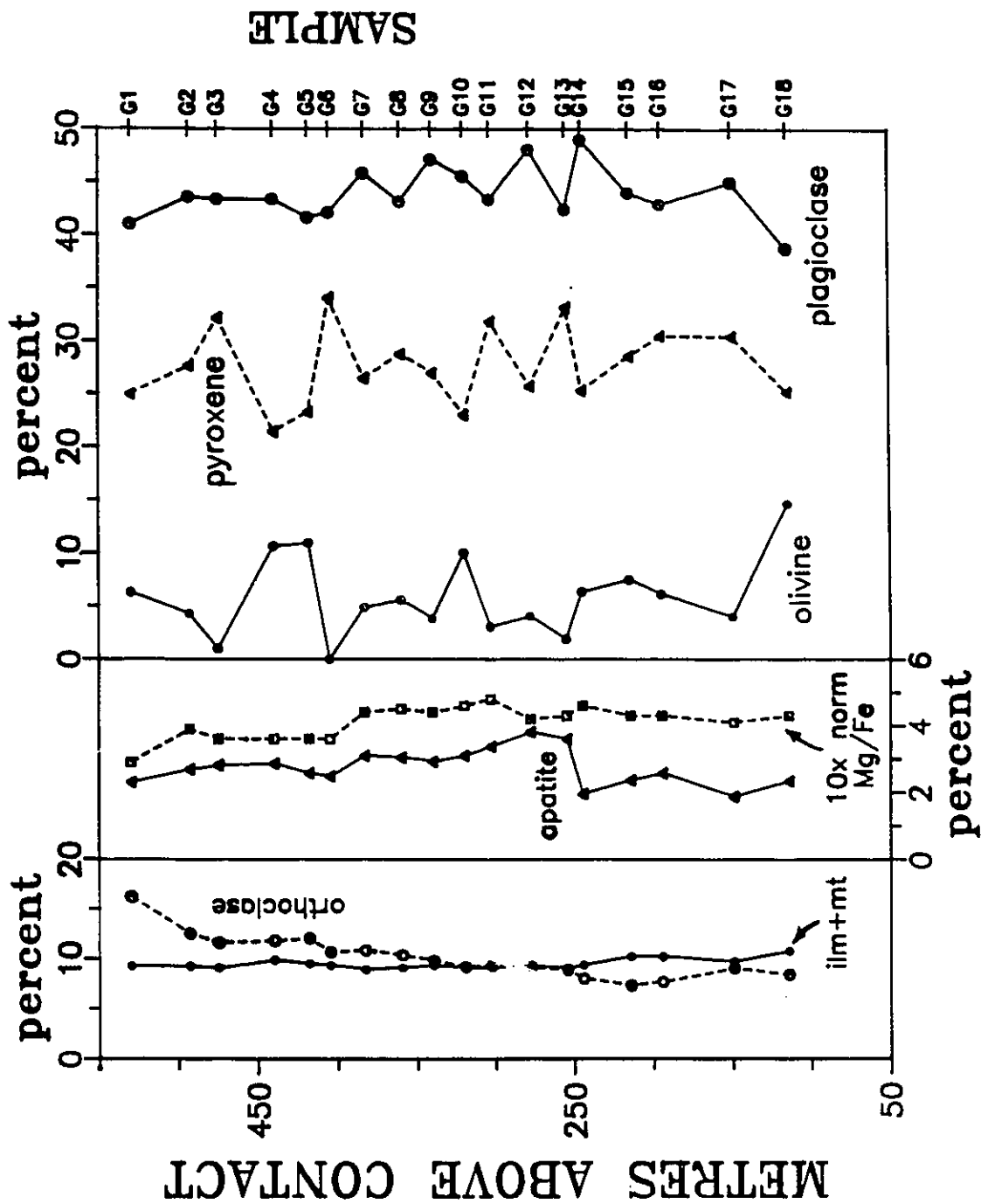
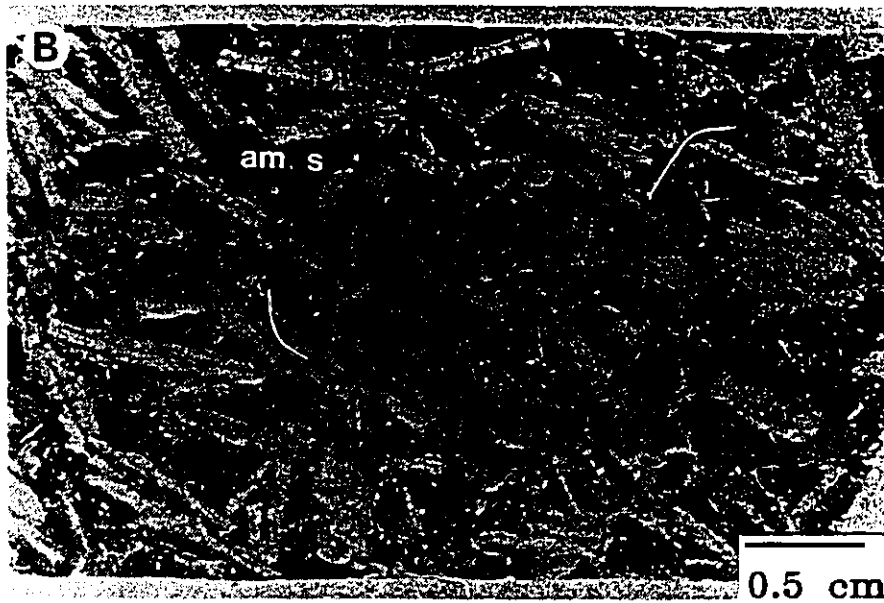
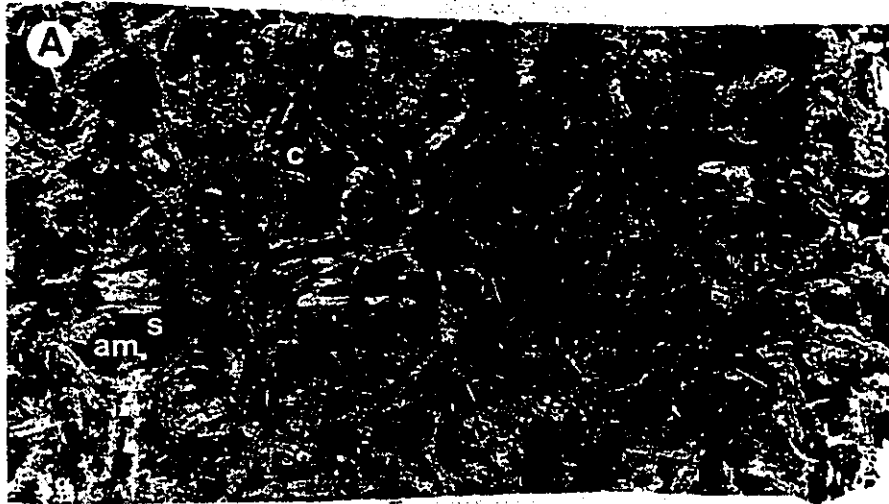


Fig. 2-15: Photographs of thin sections from GL gabbro in the unmineralized zone.

A. Homogeneous gabbro with subhedral plagioclase laths (white), subhedral to interstitial clinopyroxene (c), interstitial spinel (s, opaque), amphibole (am), and very fine-grained, euhedral ubiquitous apatite (white spots). Clinopyroxene is partly altered to actinolite, and plagioclase is rimmed by cloudy albite.

B. Aligned plagioclase laths in homogeneous gabbro. This texture is common in the unmineralized zone and forms a westerly trending lineation or igneous lamination that dips moderately.

C. Intergrowths of amphibole and plagioclase in sample G1 at the furthest point from the mineralized zone. This texture resembles that of partly altered, subhedral clinopyroxene xenocrysts included in albite microdikelets, and is interpreted to be a result of the replacement of primary clinopyroxene by late interstitial melt that infiltrated the crystal pile.



Clinopyroxene is anhedral and interstitial to plagioclase. Throughout the section approximately 50 to 60 % of each clinopyroxene crystal is altered to amphibole, although this may vary from about 10 to 100 %.

The texture of gabbro in sample G1 is significantly different than that in the rest of the unmineralized section. In G1 plagioclase and amphibole are intergrown (Fig. 2-15c). The intergrowths are interpreted as late stage replacement of original clinopyroxene by albitic feldspar, and not as a primary symplectic relationship.

B- Mineralized zone

There are two peculiar features observed in the mineralized zone of the GL gabbro that are not found in the unmineralized zone. The first is compositional and textural heterogeneity as illustrated in photographs (Fig. 2-16a, b and c). The second feature is the occurrence of irregular pale-pink coloured pods of saccharoidal albite.

Whole rock composition heterogeneity across the mineralized zone is shown by the variation of CIPW normative mineral abundances of samples from borehole 7 (Fig. 2-17), located on Figures 2-12 and 2-13. The variations of normative mineralogy do not agree, on the whole, with approximate modal compositions because (1) several samples (circled in Fig. 2-17) contain albite microdikelets, and (2)


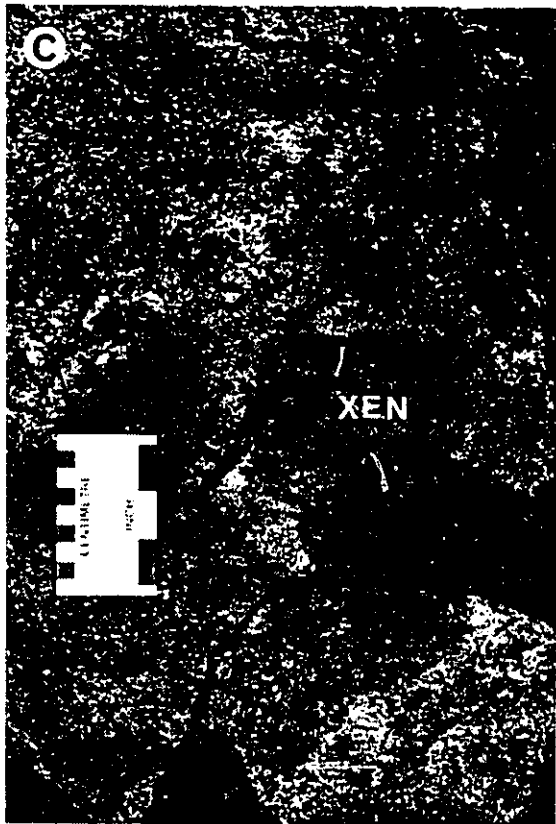
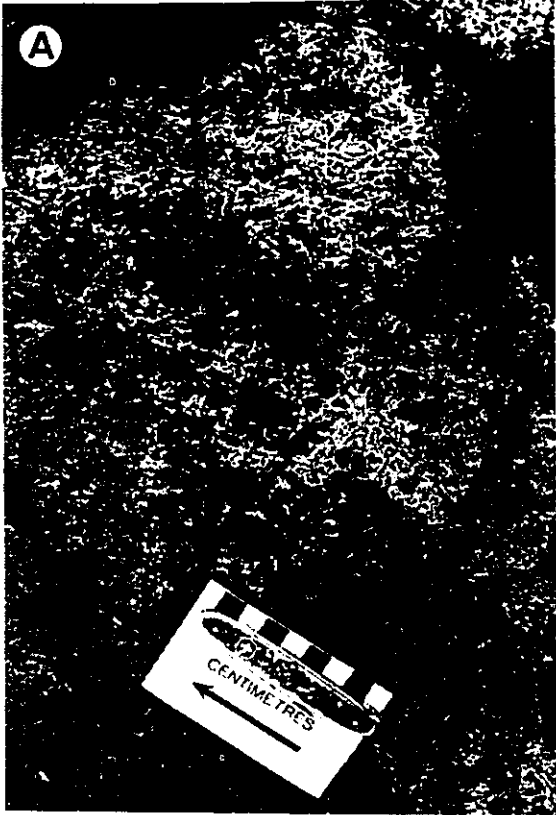


Fig. 2-16: Textures of GL gabbro exhibited in the mineralized zone.

A. and B. Heterogeneous gabbro typical of gabbro in the mineralized zone. Plagioclase forms white, lathlike crystals. The dark minerals are predominantly clinopyroxene, spinel and olivine.

C. Rare xenolith of gabbro within the heterogeneous gabbro. The type and abundance of minerals in the xenolith is the same as that of GL gabbro, therefore, xenoliths are interpreted as autoclastic in origin.

D. A single dendritic olivine crystal intergrown with optically continuous plagioclase from sample G59. This texture is common in heterogeneous gabbro. The subophitic olivine from nearby sample G58 is strongly zoned (see text). The dendritic texture and zoning are interpreted to have originated by rapid crystallization brought about by the injection of the highly evolved, volatile-rich magma into the crystal mush. The injection of evolved melt was forceful and resulted in the mixing of crystals and melt to form the heterogeneous gabbro (A and B), and autobrecciation of crystalline gabbro (C). Mulja (1989) inferred that the dendritic texture formed as a result of quenching of the GL gabbro against the quartz monzonite body, however, some field evidence (e.g., fine-grained chill margins in the quartz monzonite at both east and west contacts) suggests that the quartz monzonite intruded the GL gabbro.



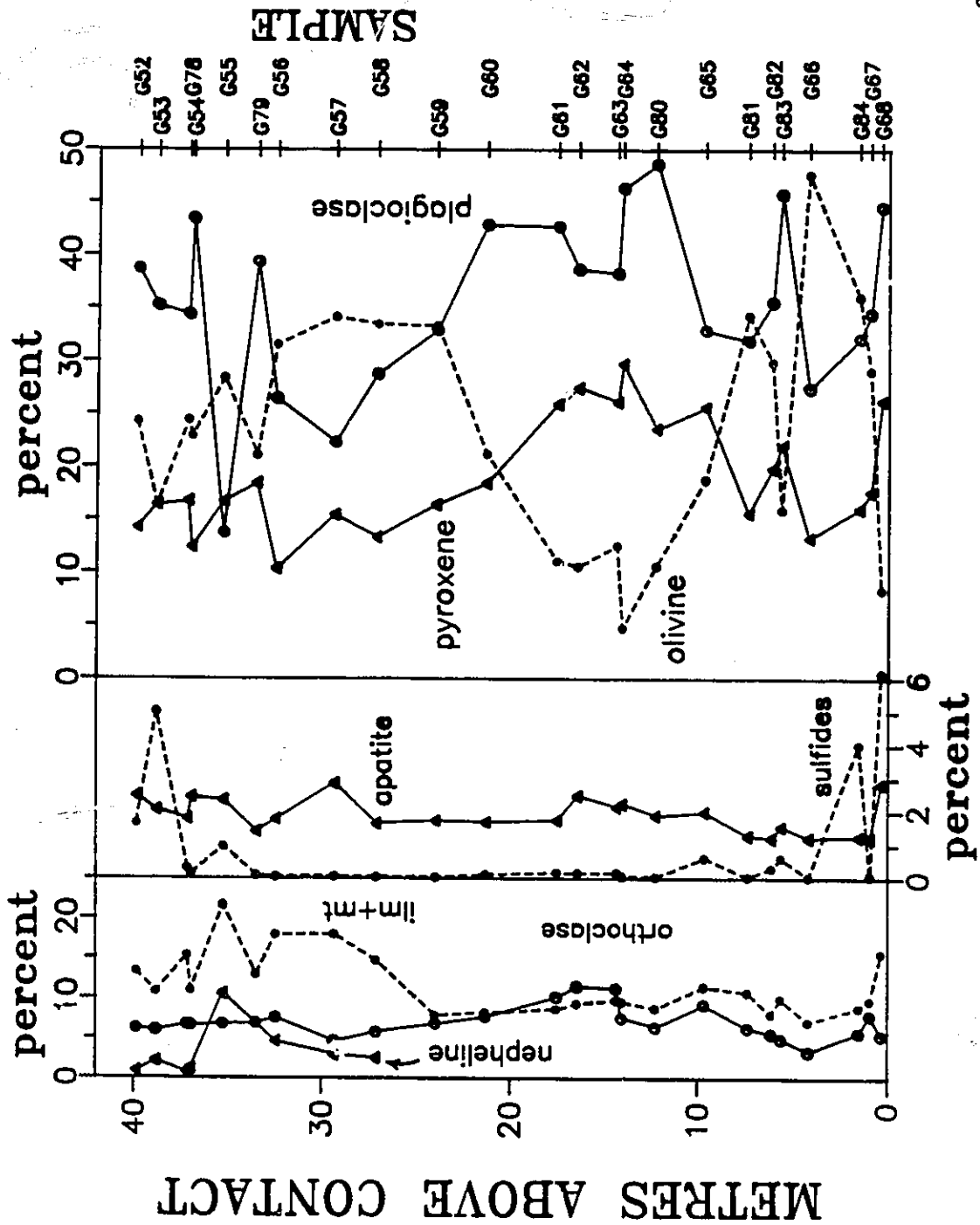


Fig. 2-17: CIPW normative mineral abundance across a section of the mineralized zone in the GL gabbro.

heterogeneity may occur on the centimetre scale so that analyses represent average compositions.

The heterogeneous GL gabbro consists of various proportions of plagioclase, clinopyroxene, olivine and magnetite and includes olivine gabbro, gabbro, mela-olivine gabbro and troctolite as representative rock types. Magnetite and apatite are ubiquitous but the prefix 'magnetite' or 'apatite-bearing' is omitted from rock names as a matter of convenience.

The order of major mineral crystallization is similar to that of unmineralized gabbro. In order of first appearance the crystallization sequence is plagioclase, magnetite, apatite, olivine and clinopyroxene. Note that apatite after magnetite is opposite to the order observed in the unmineralized zone.

The morphologies of plagioclase, magnetite and apatite in the mineralized zone are similar to those in the unmineralized gabbro. Clinopyroxene in the mineralized zone is typically poikilitic whereas in the unmineralized zone it is anhedral and interstitial. Olivine forms several unusual textures. In general, olivine is anhedral and interstitial to subophitic (Fig. 2-20 a and b), but it is also skeletal or hopper shaped and forms branching crystals up to several centimetres in length (Fig. 2-16d).

There are rare, small, angular xenoliths of gabbro unevenly distributed in the mineralized zone (Fig. 2-16c). They are modally and texturally similar to GL gabbro.

2-3-2 Mineral chemistry

Representative clinopyroxene and plagioclase analyses of mineralized and unmineralized gabbro are presented in Table 2-1 b and c. Note that samples analyzed were not intended to represent the entire GL gabbro. Probe work in this study was only intended to supplement the more extensive study by Mulja (1989).

Mulja and Mitchell (1990) state that major mineral compositions across the mineralized zone vary only slightly and non systematically. The composition of olivine varies between Fo₄₄₋₅₆, plagioclase cores between An₄₅₋₅₇ and the Mg/(Mg+Fe) of clinopyroxene between 0.40-0.67. The composition of thick plagioclase rims is considerably more sodic and will be discussed in more detail below.

The composition of plagioclase cores and clinopyroxene in sample G2, located near the top, or western margin, of the unmineralized gabbro section (Fig. 2-14) are within the range determined for the mineralized zone by Mulja and Mitchell (1990). It is likely that the maximum anorthite content of plagioclase in G2 (An₅₁) and Mg/(Mg+Fe) of clinopyroxene (0.66) are near minimum values for the

section from G18 to G1 because the normative Mg/Fe ratio in Fig. 2-14 decreases across the section.

Mulja (1989) stated that olivine is unzoned; however, three strongly zoned subophitic grains in sample G58 were found and analysed in this study. Core and rim compositions on two grains are 49 % and 40 % forsterite, respectively, and 35 % and 29 % on a third grain. The NiO content varied from less than detection limit (300 ppm) to 500 ppm. The olivine zoning is difficult to explain since the mineral is known to reequilibrate easily and is, therefore, rarely zoned. Perhaps the conditions for growth of zoned olivine were also responsible for skeletal and dendritic growth of some olivine crystals (Fig. 2-16d).

2-3-3 Albite rims, microdikelets, and pods

Abundant albite occurs throughout the GL gabbro in (1) thick rims on plagioclase; (2) microdikelets; and (3) albite pods. The plagioclase rims occur throughout the GL gabbro, but the latter two types occur predominantly in the mineralized zones. It should be emphasized that Mulja & Mitchell (1990, 1991) refer to albite pods and microdikelets as zones of intense hydrothermal alteration where original gabbro textures were destroyed and albite deposited; however, evidence described below and in Chapter three

suggests that the origin of albite is more complex than this.

A- Albite rims

Thick rims of albite and/or oligoclase (An_7 to 25) are found surrounding cumulus plagioclase crystals throughout the mapped portion of the GL gabbro, and make up approximately 1 to 5% of any rock. The rims are typically 25 to 50 % as thick as the surrounded crystal (Fig. 2-18c) and fill interstitial positions (lower left in Fig. 2-19a). The albite rims contain abundant micron sized inclusions such as apatite, amphibole and orthoclase (Fig. 2-18b; Fig. 2-19c). In thin section albite rims are cloudy and in hand sample they are pink, whereas cumulus plagioclase is clear, and white, respectively.

The compositional change across a cumulus plagioclase grain and into a surrounding rim is examined by spot analysis using an electron microprobe (micromapping) (Fig. 2-18). The changes in anorthite, orthoclase, BaO, and FeO content across the grain-rim contact near point A in Fig. 2-18c are indicated in Figure 2-18d. The two analyses, separated by a distance of approximately 14 microns, imply that there was a large difference between compositions of the liquids that crystallized the respective minerals.

Fig. 2-18: Examination of an albite/oligoclase rim in sample G52 by micromapping. A and B are scanning electron microphotographs; C is a sketch of A, and B is a close-up of the left-hand-side of A. Note the irregular shaped clinopyroxene crystal (cpx) in all three diagrams. D is a plot of microprobe spot analyses of plagioclase across section A to B in sketch C.

A. Hollow spinel (upper left, white) crystal is filled by plagioclase and biotite, and is surrounded by clinopyroxene (light grey). All clinopyroxene in the photo is optically continuous and is part of a larger ophitic crystal out of the photo. Two cumulus plagioclase crystals (pl) are partly outlined (dashed lines). Euhedral apatite occurs in the upper right corner.

B. Close-up of A (2.5X magnification) showing greater detail. Cumulus plagioclase grains, partly outlined by dashed lines, are clear of inclusions relative to albite/oligoclase rims. Inclusions in the rim are very fine-grained, euhedral apatite (white), amphibole (light grey) and orthoclase (grey, see also Fig. 2-19C). A very thin rim of amphibole (lighter grey than clinopyroxene) separates clinopyroxene from plagioclase rims. The different grain sizes and host minerals for apatite imply that there were two generations of apatite growth.

C. Three optically continuous albite rims are indicated in C., e.g., clinopyroxene at the left-hand-side occurs along the contact between two albite grains. The numbers in plagioclase and clinopyroxene represent An content and molecular $MgO/(MgO+FeO)$, respectively. The plagioclase compositions along line A to B are plotted in D. Note two chalcopyrite grains (x) occur along mineral/albite rim contacts.

D. Plagioclase compositions obtained by microprobe spot analyses. The An, Or, and FeO contents of the cumulus plagioclase are considerably greater, and BaO less, than those of the rims. The contacts are sharp.

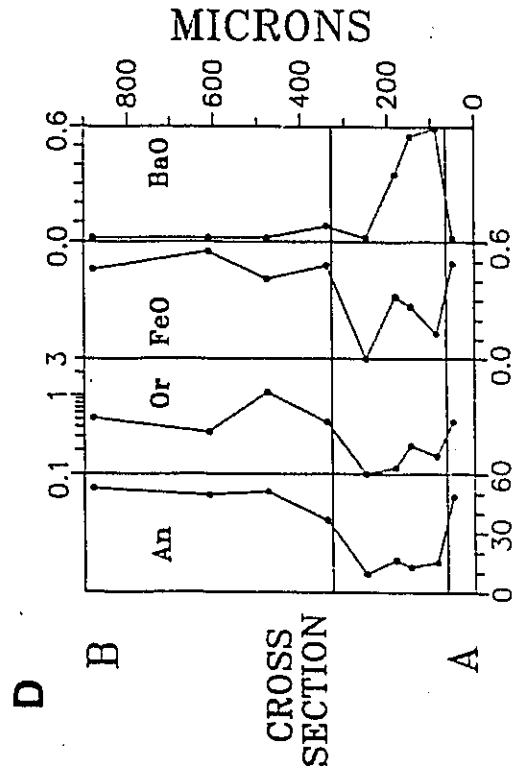
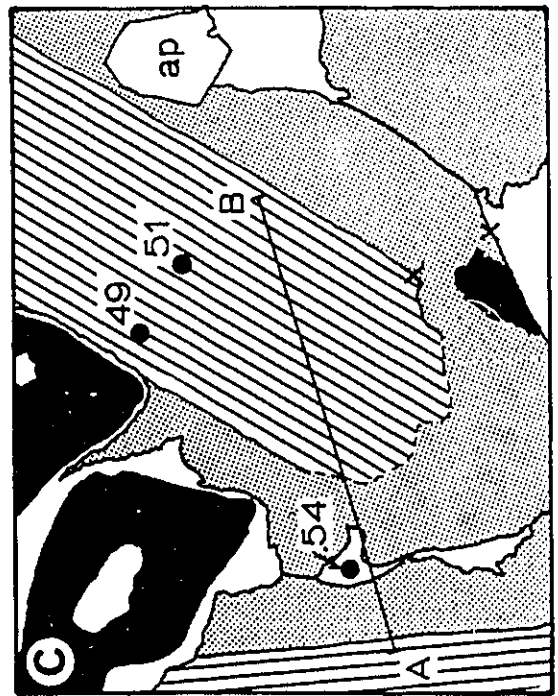
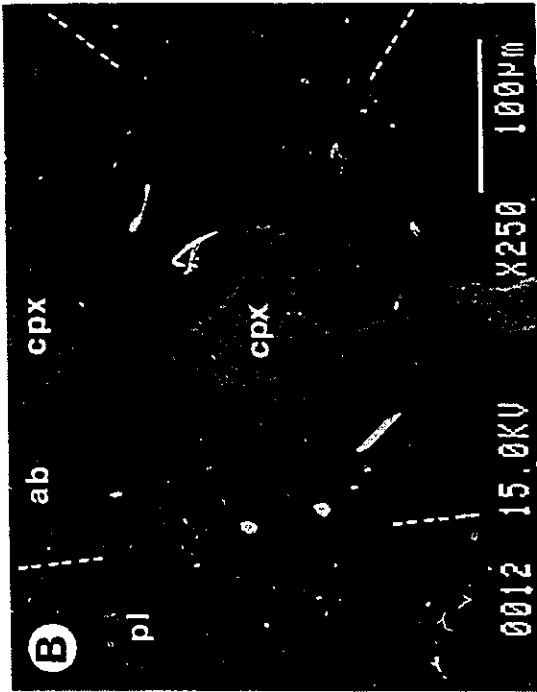
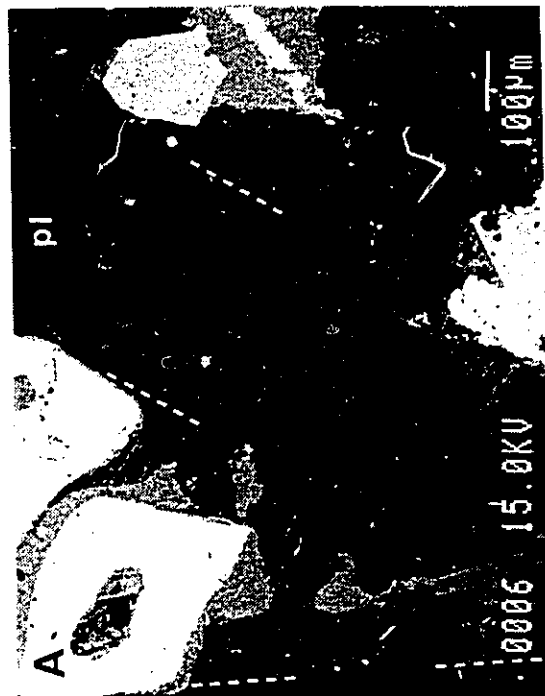


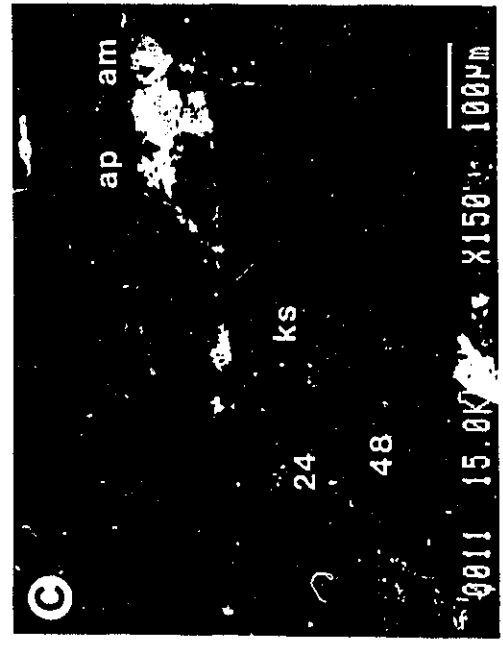
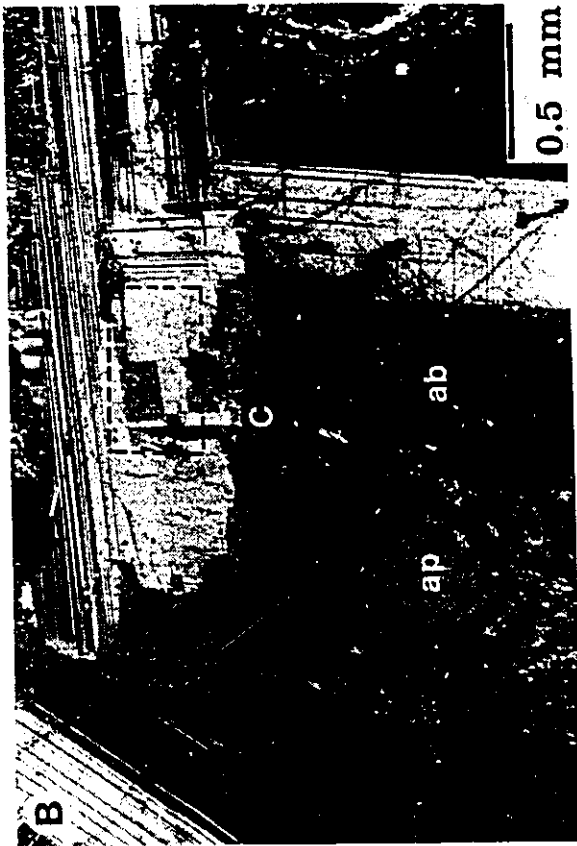
Fig. 2-19: Textural relationships of albite/oligoclase rims in the GL gabbro. A is a photograph of a thin section; B and D are photomicrographs; and, C is a scanning electron microphotograph. Photos A, B, and C are a telescoping series of photos from sample G58 to show increasing detail; C is a close-up of a portion of B (inset), and B is a close-up of a portion of A (inset). D is from sample G65.

A. Gabbro consists of subophitic olivine, subhedral plagioclase (white), subhedral spinel (opaque), interstitial clinopyroxene (light grey) and albite rims (cloudy, grey). The inset in the lower left shows the interstitial nature of albite rim growth.

B. Inset from A showing the cloudy nature of the albite grains (ab), and partial recrystallization of cumulus plagioclase.

C. Inset from B showing apparent crystallographic control on plagioclase recrystallization, and numerous inclusions of anhedral amphibole (am), euhedral apatite (ap), and anhedral K-spar (ks). The numbers in cumulus plagioclase (grey) and recrystallized patch (darker grey) indicate An contents.

D. Albite/oligoclase rim intergrown with clinopyroxene on cumulus plagioclase crystal. The clinopyroxene is optically continuous and forms part of a large, subophitic clinopyroxene grain out of the photo. The clinopyroxene intergrown with feldspar is partly altered to green amphibole. This texture is interpreted to be the result of replacement of the pyroxene. Photo located at the edge of an albite microdikelet. Within the microdikelet, clinopyroxene xenocrysts are partly replaced and exhibit intergrowth textures similar to those shown in sample G1 (Fig. 2-15C). The grey patches on the cumulus plagioclase grain are remnant carbon coating, applied for microprobe analysis.



The liquid that crystallized albite/oligoclase rims underwent limited reaction with initial plagioclase and clinopyroxene crystals. Examples of recrystallized plagioclase are found in Figures 2-19b and c. The clinopyroxene located in albite/oligoclase rims is replaced or partly altered to amphibole. Examples of replaced clinopyroxene are found in Figures 2-18b and 2-19d. In each of the examples, clinopyroxene is optically continuous and forms part of a large poikilitic crystal that continues off of the photo.

B- Albite microdikelets

Albite microdikelets are visible in hand specimen as centimetre sized, pink coloured dikelets of granular material (right-hand-side of Fig. 2-22a). They consist of cloudy, medium-grained, anhedral, granular albite, and interstitial amphibole, chlorite and chalcopyrite. The microdikelets also contain minor clinopyroxene, plagioclase, apatite and magnetite that are interpreted to be xenocrysts obtained from the GL gabbro. Clinopyroxene xenocrysts are partly altered to green amphibole; plagioclase is partly corroded or recrystallized; magnetite grains are embayed and rimmed by brown biotite and brown amphibole, and apatite is typically euhedral.

The major mineral compositions at the contact between a microdikelet and gabbro are examined by micromapping (Fig. 2-20) in a manner similar to that for rims in Fig. 2-19c. The results of mapping across a grain of clinopyroxene and plagioclase that protrude into a microdikelet are shown in Figure 2-20c and d. The contact between cumulus plagioclase and albite is more recrystallized (diffuse) than in the case of albite rims. The anorthite and orthoclase content decrease towards the edge of the cumulus plagioclase grain, BaO is scattered. FeO is approximately constant across the cumulus grain, but decreases rapidly into the albite. The gradational changes in composition across the cumulus grain are attributed to the limited reaction between it and the liquid that crystallized albite.

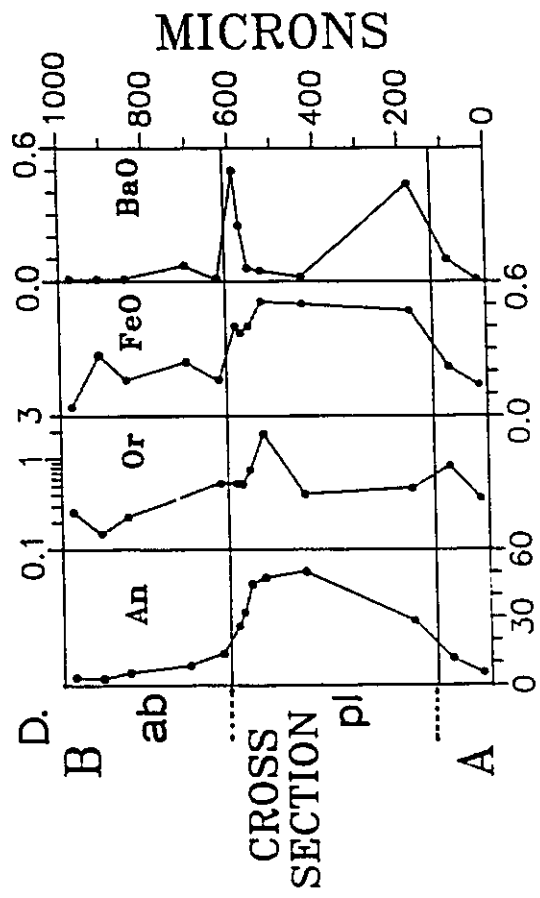
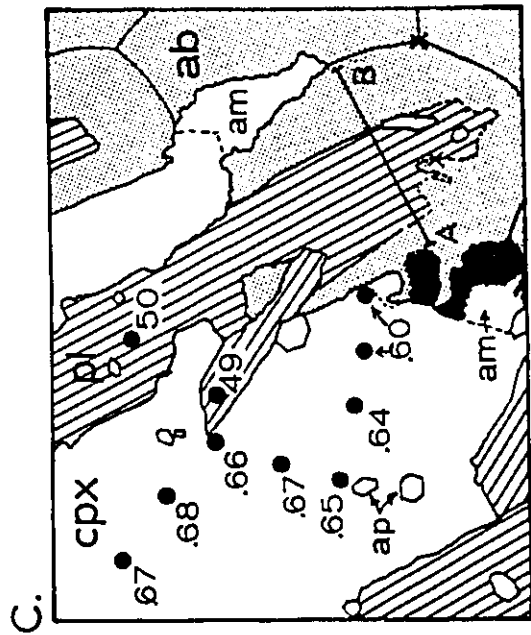
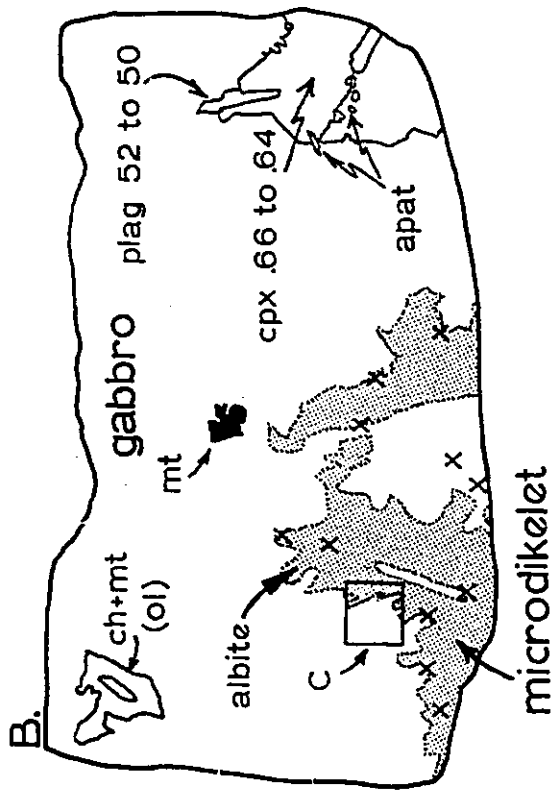
The composition of clinopyroxene was apparently unaffected during the formation of albite. The slight decrease in $Mg/(Mg+Fe)$ towards the contact (Fig. 2-20c) is only slightly greater than that exhibited in weakly zoned clinopyroxene. Clinopyroxene could not have been at equilibrium with the liquid that crystallized the albite and, as was noted in the examples for albite rims above, was partly resorbed.

Fig. 2-20: Examination of plagioclase and clinopyroxene compositions at the contact between gabbro and an albite microdikelet. **A** is a photograph of a thin section (sample G50); **B** is a sketch map of **A** indicating relevant features; **C** is a sketch map of inset in **B**, and; **D** is a plot of microprobe spot analyses of plagioclase across section **A** to **B** in sketch **C**.

A. and B. Olivine gabbro with subhedral plagioclase laths, subophitic clinopyroxene, euhedral apatite, and anhedral interstitial spinel and olivine. Clinopyroxene margins are partly altered to amphibole, particularly where it is in contact with albite. Olivine is altered to very fine spinel and pale green fibrous serpentine or chlorite pseudomorphs. Most grain boundaries in the gabbro are lined with very fine-grained fibrous, brown amphibole or biotite. An albite microdikelet (inset) cuts the gabbro at the bottom centre of the thin section. Note the xenocryst of plagioclase (right of inset in **B**) in the microdikelet. Chalcopyrite (x) is intergrown with amphibole and occurs at albite-albite or albite/mineral contacts. The numbers at the right-hand-side of **B** represent An content and molecular $MgO/(MgO+FeO)$ in plagioclase and clinopyroxene, respectively.

C. Map of inset from **B** at the contact between gabbro and microdikelet. The numbers represent An content and molecular $MgO/(MgO+FeO)$ in plagioclase and clinopyroxene, respectively. Minor amphibole (am) occurs at the clinopyroxene-albite contact. Individual grains of albite (grey) are outlined. Two chalcopyrite grains (x) intergrown with amphibole occur at albite grain contacts. The partial resorption of plagioclase is evident.

D. Plot of microprobe spot analyses in plagioclase from points **A** to **B** in diagram **C**. Note that the scale is magnified 2X. The contact between plagioclase and albite is more gradational than in Fig. 2-19. due to more extensive recrystallization of the cumulus plagioclase.



C- Albite pods

Albite pods range in size from millimetres (microdikelets) to decimetres across, and form discontinuous bodies with irregular shapes (Fig. 2-21a and b). They are easily recognized in outcrop due to their pale pink colour and saccharoidal texture. They consist predominantly of granular to lath-like, fine- to medium-grained, cloudy albite (Fig. 2-22c) and minor subhedral pale brown to olive green amphibole, and, interstitial anhedral, pale-green, fibrous amphibole, chalcopryrite, orthoclase, quartz and calcite. The pods may contain xenocrysts of clinopyroxene, plagioclase, magnetite and chloritic pseudomorphs of olivine. The xenocrysts typically have textures similar to the crystals found in the GL gabbro.

There are two types of contacts between GL gabbro and albite pods. The first type is sharp (Fig. 2-22a) and the second gradational. Gradational contacts exhibit notable coarsening of clinopyroxene and plagioclase (Fig. 2-21b and d) in GL gabbro towards the pod.

To determine relationships near an albite pod, five samples (G47, G48, G49, G49a, and G50) were collected across a 1 metre section of GL gabbro containing a thin albite pod (Fig. 2-22a). The CIPW normative composition and respective mineral compositions for the five samples are shown in Figure 2-23. Sample G47 is free of microdikelets and

Fig. 2-21: Textural relationships at albite pod/gabbro contacts in the mineralized zone. Photo B is a close-up of the albite pod tip, located left of centre at the top of photo A. Photos C and D are of over-sized thin sections.

A. Irregular, discontinuous albite pod.

B. The albite pod (lower right) consists of granular or saccharoidal albite and interstitial amphibole (see Fig. 2-22C). Very coarse-grained plagioclase laths in the albite pod and neighbouring gabbro are rimmed by pink albite.

C. and D. Patches of very coarse-grained plagioclase and clinopyroxene with interstitial chalcopyrite and bornite in gabbro. The plagioclase is rimmed by albite. These sections were selected from zones marginal to albite pods and are analogous to the tip of the albite pod in B. The coarse-grained nature of plagioclase and clinopyroxene is interpreted to be due to crystallization from undercooled GL crystal mush. The undercooling was imposed by the intrusion of evolved, hydrous silicate melt that crystallized the albite pods.



Fig. 2-22: Photos of albite pod and neighbouring gabbro across a 1 m section of core from borehole 2 (Fig. 2-12). The scale for B is the same as for C. See Fig. 2-20 for examination of microdikelet in G50 selected 35 cm to the right of the albite pod.

A. Albite pod and microdikelets (white) in gabbro (dark). Samples G49 (albite pod) and G49a were collected from this core sample.

B. Photograph of thin section from olivine gabbro (sample G47) selected 35 cm to the left of the albite pod in A. Olivine (ol) is subophitic; plagioclase (white) is subhedral; apatite is euhedral (white spots), and; spinel (m) and clinopyroxene (cpx) are interstitial. Albite microdikelets are not visible in the hand specimen and albite rims on plagioclase are rare, therefore effects of albite pod introduction on G47 are considered to be negligible.

C. Photograph of thin section from the albite pod. Albite is cloudy and occurs in both granular and lath like forms, but they have equivalent compositions. Amphibole (dark) is interstitial and intergrown with chalcopyrite. Fresh clinopyroxene occurs in the lower left-hand corner of the photo.

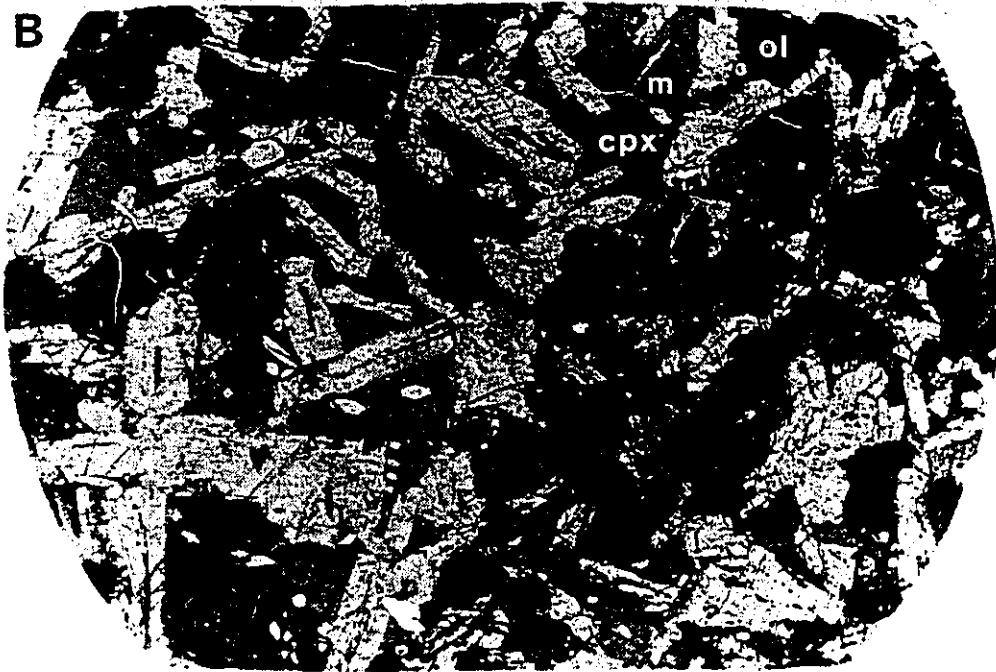
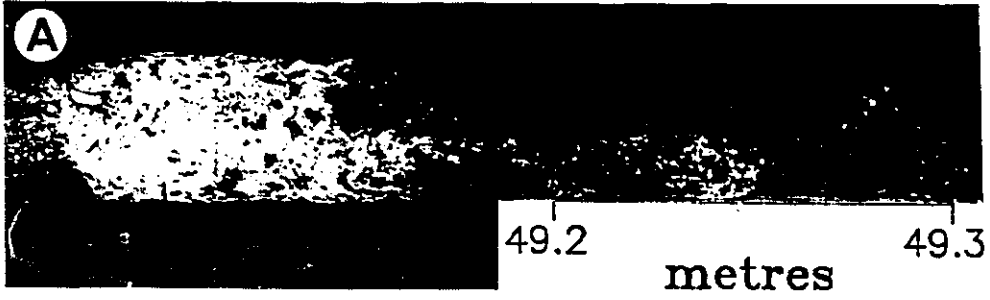
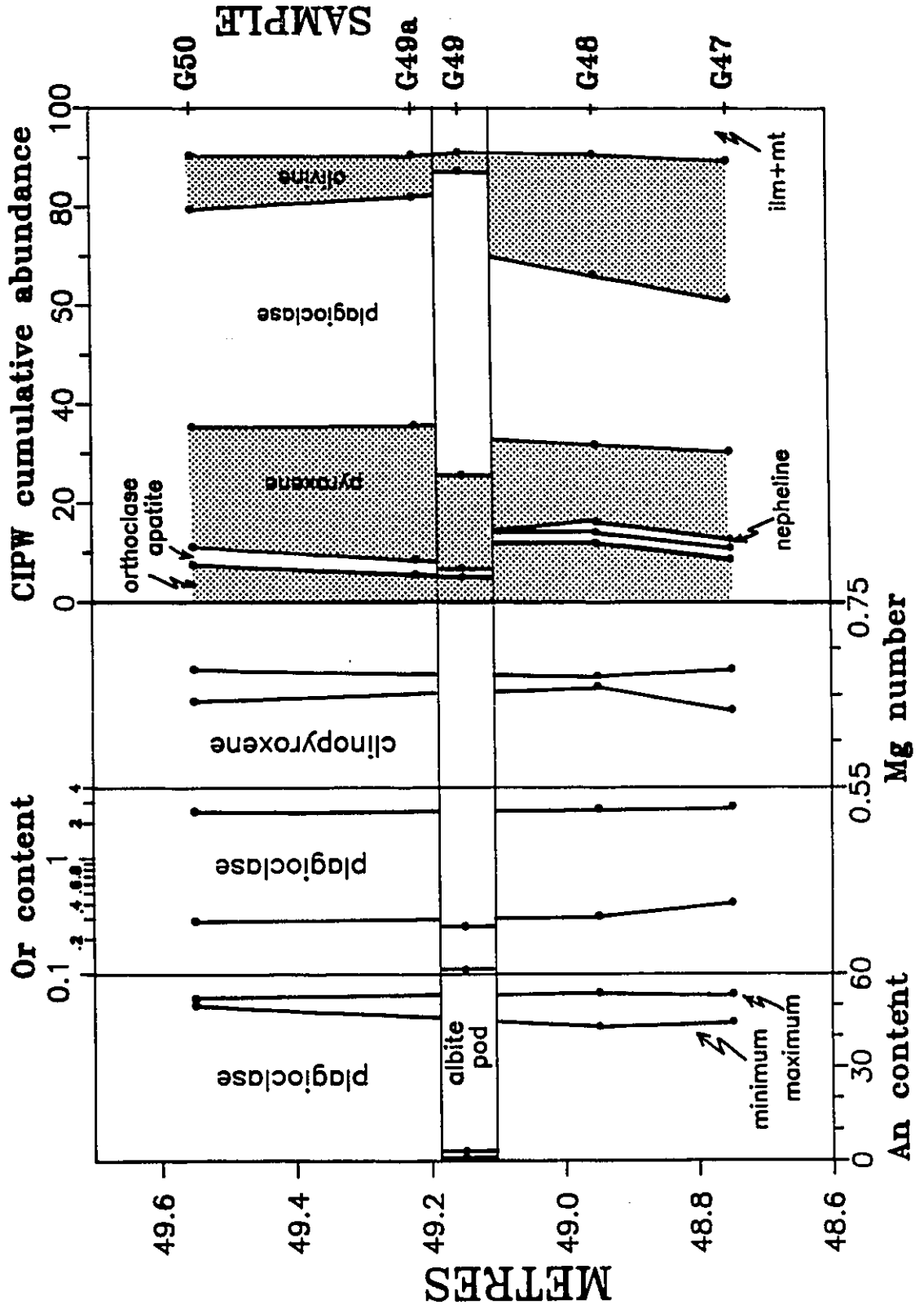


Fig. 2-23: Mineral compositions (plagioclase and clinopyroxene at left) and CIPW normative mineral abundance in an albite pod and neighbouring Geordie Lake gabbro. The samples were collected from a one metre section of drill core shown in Fig. 2-22a. Samples G49 and G50 contain albite microdikelets (see Fig. 2-20); G48 trace microdikelets; and, G47 contains no visible microdikelets, and accessory albite rims on plagioclase. The constant plagioclase and clinopyroxene compositions in the gabbro are consistent with the constant compositions at the contact with a microdikelet (sample G50 in Fig. 2-20) and agrees with the hypothesis that the albite pod intruded the gabbro.



contains less than 1 % albite rims. The normative mineralogy is approximately the same as the mode. Sample G48 contains rare microdikelets. Sample G49 is from the albite pod. Samples G49a and G50 contain microdikelets and the CIPW mineralogy is, as expected, more feldspathic. Contrary to the norm, the modal composition of G50, excluding microdikelets, is approximately the same as that of G47 and G48. The mineral compositions of samples G47, G48 and G50 are approximately the same. The anorthite ($An_{1.1}$ to 3.2) and orthoclase ($Or_{.11}$ to $.26$) contents of plagioclase in the albite pod are considerably lower than in the plagioclase of the surrounding gabbro (An_{45-57}) and are similar to that of albite microdikelets. The composition of the clinopyroxene xenocryst in sample G49 was not determined, but since the composition of clinopyroxene in contact with a microdikelet (Fig. 2-20c) is the same as that in gabbro then the composition of the xenocryst is probably the same as in the gabbro.

2-3-4 Summary of plagioclase features

The cumulus plagioclase crystals are weakly and normally zoned. Discontinuous zonation, excluding albite rims, has not been observed. Individual plagioclase crystals that have not been affected by the addition of

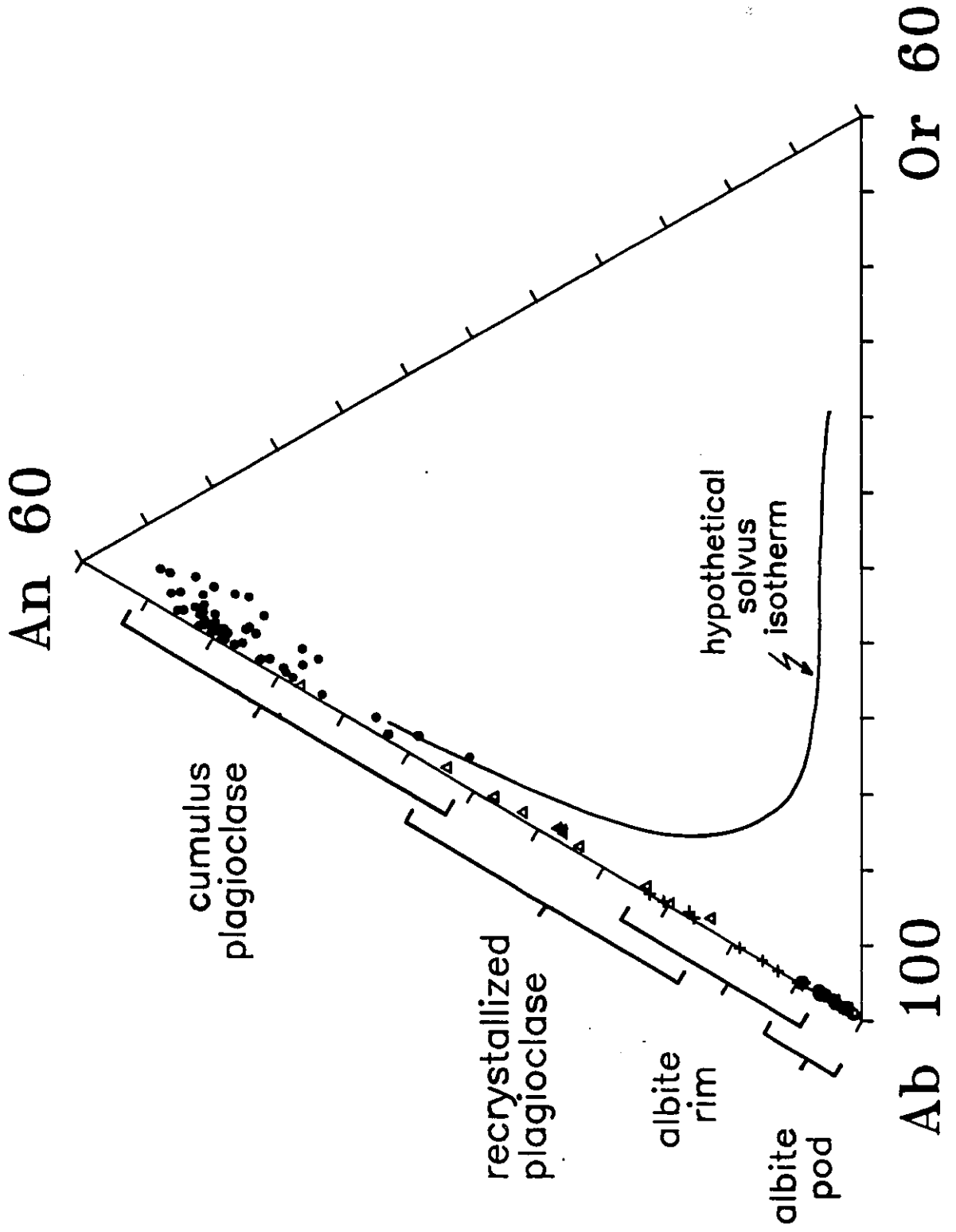
albite/oligoclase rims have core to rim variations less than 5-10 % An.

Plagioclase in albite rims, microdikelets and pods have several features in common that imply they were formed by the same process(es). The common features are:

- (1) pink colour in hand specimen,
- (2) inclusion of very small grains (less than 50 microns in size) of apatite, amphibole and orthoclase,
- (3) interstitial chalcopyrite plus amphibole,
- (4) occurrences in contact with pristine to partly altered clinopyroxene, and
- (5) very low anorthite and orthoclase contents.

The range of all feldspar compositions from various settings within the mineralized zone are plotted in a feldspar ternary diagram (Fig. 2-24). The feldspars are subdivided on the basis of location into early (cumulus) plagioclase, recrystallized plagioclase, albite/oligoclase rims, albite microdikelets, and albite pods. Recrystallized plagioclase can be distinguished optically from primary plagioclase, and is located within the ghost outline of cumulus plagioclase crystals. The plagioclase compositions in Figure 2-24 form a continuum from labradorite to albite and this compositional variation cannot be explained in terms of normal magmatic processes. The trend of decreasing orthoclase with increasing albite is opposite to that

Fig. 2-24: Summary of plagioclase compositions in Geordie Lake gabbro. Examples of K-spar are not plotted. Recrystallized plagioclase is visible in thin section as cloudy feldspar within the ghost outline of original plagioclase crystals. Plagioclase in microdikelets is included along with data for albite pods. The trend of feldspar compositions does not follow that expected from a crystallizing magma. In a fractionating magma the compositions would lie along a trend approximately parallel to the hypothetical solvus isotherm.



expected by either equilibrium or fractional crystallization processes (vide Carmichael et al. 1974).

2-3-5 Discussion

The following three stages are proposed to have occurred during solidification of the GL gabbro:

(1) *Cumulus to early intercumulus stage.* The GL gabbro was emplaced as a crystal mush consisting of plagioclase and silicate melt. The plagioclase crystals formed a framework for crystallization of the interstitial melt and there was little, if any, crystal-free magma in the chamber. Solidification of the interstitial melt generated apatite, magnetite, olivine, clinopyroxene and weakly zoned plagioclase.

(2) *Late intercumulus stage.* Normal post-cumulus crystallization was interrupted by infiltration of an evolved silicate melt into the crystal pile and the flushing out (or dilution?) of original interstitial melt. The late silicate melt migrated through interstices, crystallized sodic plagioclase, recrystallized some of the cumulus plagioclase, partly resorbed clinopyroxene, and reacted with magnetite to form biotite and amphibole. Three prominent features of the mineralized zone generated by presumably forceful injection of late silicate melt are (a) very coarse-grained plagioclase and clinopyroxene at albite pod-

GL gabbro contacts, (b) branching and zoned olivine, and (c) heterogeneous gabbro. The first two features are presumably a result of the gradient in either temperature or volatile content between the two melts and the latter a result of the mixing of crystals and the two magma types.

(3) *Deuteric stage*. During this stage clinopyroxene was partly altered to amphibole, late plagioclase was albitized, and fibrous amphibole was deposited in interstices of all rock types by a hydrous fluid. It is proposed that the hydrous fluid was derived from the evolved silicate melt that infiltrated the crystal pile in stage two. This is an important distinction because there is abundant evidence for the coprecipitation of the hydrous silicates with sulfides (see Chapter four). Therefore, the nature and origin of the infiltrated silicate melt is an integral step in resolving the genesis of sulfide mineralization.

Chapter 3 - Geochemistry

3-1 Introduction

This chapter provides geochemical evidence bearing on the models postulated in Chapter two for the intrusive and subsequent crystallization histories of the Two Duck Lake and Geordie Lake gabbros. The respective models further constrained by the geochemical data provide a framework that can be used to describe the genesis of sulfide and PGE mineralization in chapter four.

3-2 Organization of trace-element data

Trace-element data (Tables AI-6, AI-7 and AI-12 in the appendix) is organized into three groups according to broadly similar geochemical nature and behaviour of the elements analyzed. The groups are as follows:

- a) large ion lithophile elements (LILE): Cs, Rb, K, Ba and Sr,
- b) high field strength elements (HFSE): Sc, V, Zr, Hf, Ta, Nb, and Th, and
- c) Y and rare earth elements (REE): Y, La, Ce, Nd, Sm, Eu, Gd, Yb and Lu.

3-3 Geochemistry of the Two Duck Lake gabbro

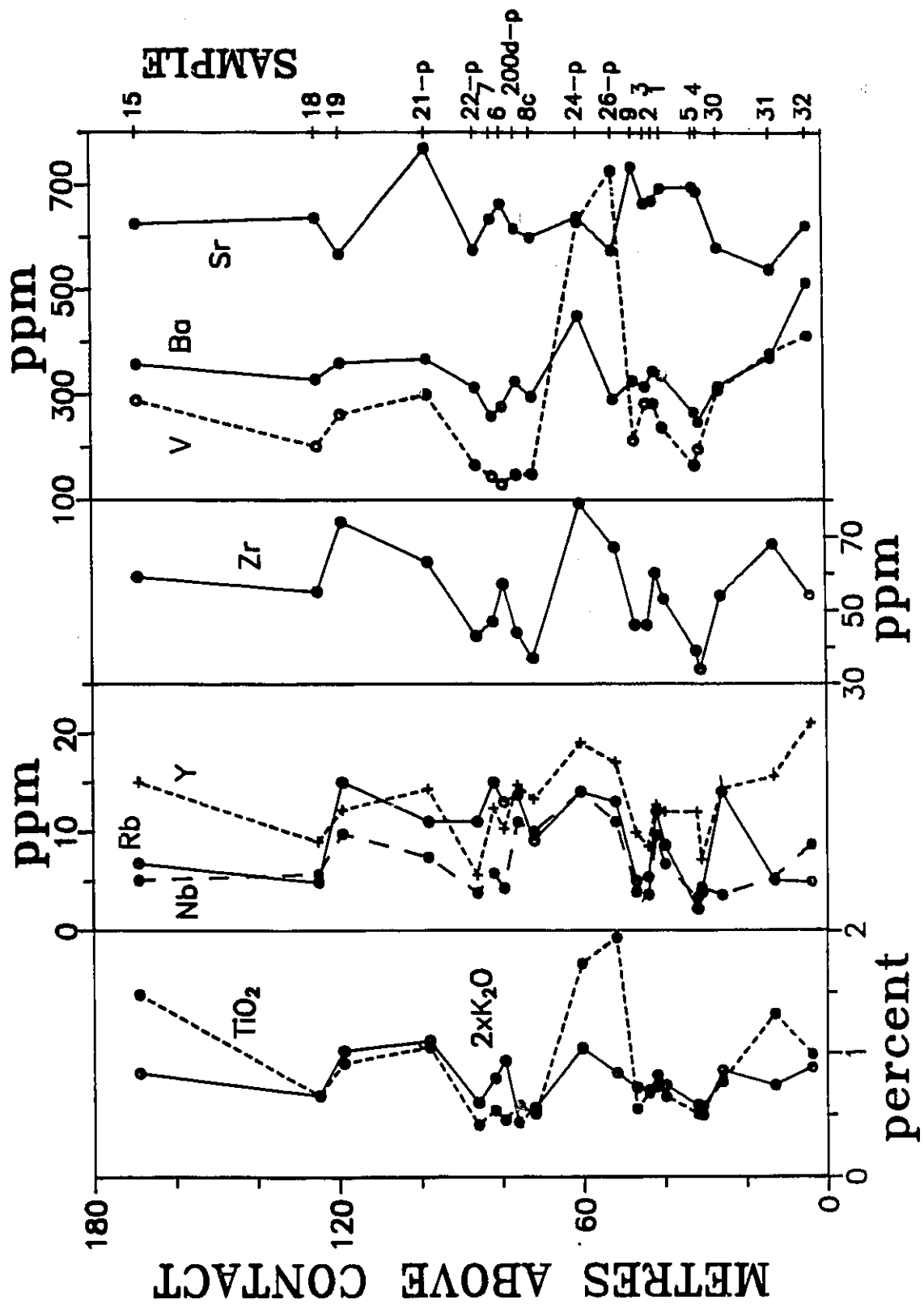
The model proposed in section 2-2-5 for emplacement and subsequent crystallization of the TDL gabbro can be tested with geochemical data by answering the following questions:

- a) do trends for trace-element concentrations in the TDL gabbro agree with those expected for an intrusive body which has not undergone processes of vertical fractional crystallization,
- b) how is pegmatitic TDL gabbro related to coarse-grained TDL gabbro,
- c) is there evidence for settling of plagioclase out of the intruded crystal mush, and
- d) is pegmatite-associated granophyre representative of interstitial melt, and if so, what fraction of the initial TDL magma does it represent?

3-3-1 Compositional cross section

The compositions of coarse-grained and pegmatitic gabbro across the lower zone of the TDL gabbro are shown in Figure 3-1. The trends for trace-elements, except Sr and to some extent Ba, from the base to the top, are similar, i.e., peaks and troughs in the curve for each element tend to line up with those of other elements. This observation is substantiated by calculated inter-element linear correlation

Fig. 3-1: Compositional variation of trace- and minor-elements in coarse-grained and pegmatitic facies across the lower zone of the Two Duck Lake intrusion. Peaks for TiO₂ and V in samples F24 and F26 correspond to high spinel contents. All sample are referred to with an 'F' prefix in the text, and the -p suffix indicates pegmatitic gabbro.



coefficients (Table 3-1) that are significant to highly significant for most element pairs. Rb data are omitted due to analytical uncertainty, and Sr data are omitted because of its compatible behaviour, particularly in plagioclase and apatite.

Table 3-1. Calculated linear correlation coefficients for coarse-grained and pegmatitic TDL gabbro in Figure 3-1, and samples F8 and F8p (n=20). Samples F31 and F32 were omitted since they contain contact-related granophyre. For this number of samples a correlation coefficient greater than 0.4 is probably significant (i.e., 5% level of significance); a value >0.51 is significant (1% level); and, a value >0.65 is highly significant (0.1% level).

	Ba	Y	Zr	TiO ₂	V	Nb
K ₂ O	.54	.33	.86	.55	.48	.35
Ba		.19	.64	.79	.47	.54
Y			.47	.59	.46	.63
Zr				.73	.65	.63
TiO ₂					.92	.55
V						.53

The nearly parallel trends for trace- and minor-element concentrations across the TDL gabbro are consistent with trends for mineral compositions (major-elements) and confirms the hypothesis that the lower portion of the TDL gabbro crystallized with no significant vertical fractional crystallization. It follows, therefore, that (a) concentrations of incompatible trace-elements in any given sample will be a function of the amount of interstitial melt or initial porosity, and (b) the average trace-element

concentrations will be close to that of the initial TDL magma crystal mush.

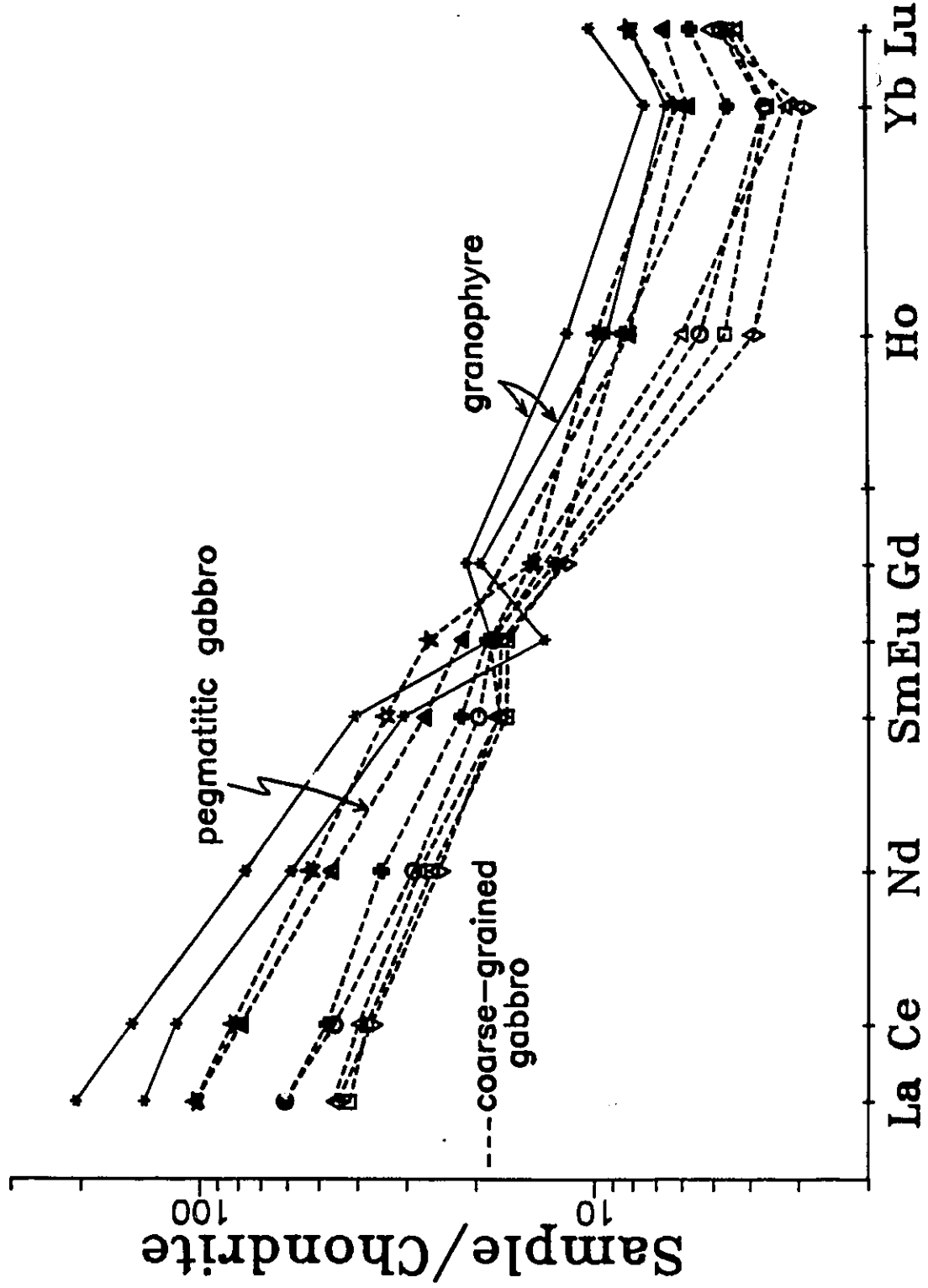
Finally, the concentration of trace-elements in pegmatitic TDL gabbro is similar to that of the coarse-grained TDL gabbro (Fig. 3-1). This feature is consistent with the mineral composition data (specifically olivine and plagioclase), and indicates that pegmatitic TDL gabbro is not more evolved than the coarse-grained type.

3-3-2 Rare earth elements

REE data for samples of coarse-grained, pegmatitic and granophyric TDL gabbro are exhibited in the chondrite normalized plot (Fig. 3-2). Each point on the diagram is determined by dividing the respective REE concentration by that in chondrites (using favoured values in Henderson 1984, Table 1-5, p. 10).

There are two important features of the REE diagram (Fig. 3-2) applicable to the genesis of TDL gabbro and granophyre. Firstly, the REE patterns, excluding La, Ce and Eu, for granophyre are approximately parallel to those for gabbro implying that they were derived from the same parental magma. The divergence from parallelism for La, Ce and Eu can be explained by fractional crystallization in the TDL gabbro (see section 3-3-3). Therefore, REE data is

Fig. 3-2: Chondrite normalized REE for coarse-grained, pegmatitic and granophyre facies of the Two Duck Lake gabbro.



consistent with the hypothesis that granophyre was derived by fractional crystallization of the TDL magma.

The second feature is a weak positive Eu anomaly for samples of gabbro. Unlike other REE, ions of Eu occur in both the 2^+ and 3^+ states in a silicate melt (Philpotts 1970). The former ion substitutes readily for Ca in many minerals, particularly plagioclase, and consequently the partition coefficient of Eu into plagioclase is greater (by at least two orders of magnitude) than that of other REE. Therefore, Eu is a sensitive indicator of plagioclase fractionation. From the positive Eu anomaly exhibited by the TDL gabbro it is inferred that some settling of plagioclase occurred prior to solidification. Alternatively, the melt could have been enriched in Eu.

3-3-3 Origin of granophyre

Based on REE evidence it is apparent that granophyre is genetically related to the TDL gabbro. This premise suggests that the granophyre pods were formed by migration of interstitial melt through the crystal pile to accumulate in pods forming granophyre. This hypothesis can be tested quantitatively by:

(a) determining weighted partition coefficients (D) for trace-element fractionation between the crystal pile and interstitial melt,

(b) comparing D values to measured trace-element concentrations, and

(c) evaluating the process of Rayleigh fractional crystallization and solving for the value F, which in this case would be the fraction of original TDL magma corresponding to granophyre.

A - Determination of partition coefficients

Partition coefficients (k_i) are defined by the equation,

$$k_i = \frac{\text{concentration of element in mineral } i}{\text{concentration of element in liquid}}$$

The partition coefficients for trace-elements between several minerals and a basaltic melt are listed in Table 3-2. The values are from Irving (1978), Henderson (1984), Pearce and Norry (1979), Fujimaki (1986) and Green and Pearson (1987). It should be noted that partition coefficients are typically dependant on melt composition, temperature, pressure and oxygen fugacity. Because not all of these variables have been completely investigated for all of the elements and all of the minerals in Table 3-2, some k_i values are somewhat equivocal. However, for this study, the values listed are deemed to be reasonable estimates.

Weighted partition coefficients are defined by,

$$D = \sum(p_i * k_i) ,$$

Table 3-2: Weighted partition coefficients (D values in left hand columns) for the TDL and GL gabbros, calculated using average modal mineral abundances (bottom rows), and mineral/melt partition coefficients (kd values in the right hand columns).

	D value (TDL gab)	D value (GL gab)	olivine	opx	cpx	amph	plag	phlog	garnet	allanite	apat	sphene	zircon	m/rim
large ion lithophile elements														
Cs	0.001	0.001			0.0036			high						
Rb	0.026	0.024			0.0041		0.05	high						
K	0.100	0.09					0.2	high						
Ba	0.391	0.38	0.005	0.011	0.3		0.6							
Sr	1.120	1.04	0.003	0.013	0.4		2				?			
high charge, high ionic potential elements													high	
U	very low	very low		0.008	0.0025				27.6					1
Th	0.002	0.002			0.005			0.6	0.3		0.636			
Sc	0.923	1.20	0.3	0.5	2.7		0.017		0.53		0.73		958	0.8
Zr	0.034	0.046			0.1									0.7
Hf	0.004	0.007												
Ta	0.180	0.25			0.4		0.05					17.8		
Nb	0.078	0.11	0.01	0.15	0.1		0.01	1	0.1			6.7		
rare earth elements and Y														
La	0.181	0.24			0.08		0.14		0.05	820			3.11	
Ce	0.301	0.41	0.009	0.02	0.34		0.14	0.03	0.05	635		53	3.49	
Nd	0.421	0.60	0.009	0.05	0.6		0.08	0.03		460		88	3.8	
Sm	0.590	0.86	0.009	0.05	0.9		0.08	0.03	0.6	205		102	4.72	
Eu	1.677	1.72	0.008	0.05	0.9		2.5	0.03	0.9	80		101	4.23	
Gd	0.584	0.84	0.012	0.05	0.9		0.1		3.7	130		102	6.77	
Yb	0.453	0.58		0.34	1		0.97	0.07	30	8.9		37.4	254	0.2
Y	0.460	0.63	0.01	0.2	1		1	0.03	2	20		60	60	
Lu	0.371	0.49		0.11	0.8		0.89	0.08	35	7.7		26.9	333	
transition metals														
V	1.1	1.6	0.04	2.8	1.3									12
Ni	3.2	3.9	14	2	4.3									14.7
modal abundance in TDL gabbro			0.075	0.075	0.3		0.5				0.006			0.044
modal abundance in GLG gabbro			0.06		0.4		0.44							0.09

kd values from Irvina 1978; Henderson 1984; Pearce and Norry 1979; Fujimaki 1986; and, Green and Pearson 1987

where p_i is the proportion of mineral i , and by,

$$D = \frac{\text{concentration of element in all solids}}{\text{concentration of element in the liquid}} \quad (1)$$

Weighted partition coefficients (first column in Table 3-2) were calculated with the average modal proportion of minerals in the TDL gabbro assuming that the interstitial melt was in equilibrium with the crystal pile. The average modal proportions used are olivine (7.5%), orthopyroxene (7.5%), clinopyroxene (30%), plagioclase (50%), apatite (.6%) and magnetite (4.4%).

Based on calculated D values the trace-elements can be subdivided into groups according to their degree of compatibility in the crystal pile. For instance, a strongly incompatible element (e.g., Zr) will favour the interstitial melt over the crystallizing gabbro and therefore increase with increasing fractionation. The groups are as follows:

- (a) strongly incompatible elements ($D < 0.1$) - Cs, Rb, K, Th, Zr, Nb and Hf,
- (b) moderate to weakly incompatible elements ($1 > D > 0.1$)
Ba, Sc, Ta, REE (excluding Eu) and Y,
- (c) weakly compatible elements ($1 < D < 2$) - Sr, Eu and V,
- (d) moderately compatible elements ($D > 2$) - Ni.

**B - Comparison of trace-element data to model D values:
element-Zr variation diagrams**

A useful means of displaying trace-element data is by comparing concentrations of individual elements to that of Zr as in Figures 3-3 to 3-5. Zr is selected as the element of reference for the following reasons: a) Zr data are available for the entire suite of samples, b) calculated linear correlation coefficients for Zr (Table 3-1) are moderate to high, and c) the weighted distribution coefficient for Zr is very low (Table 3-2), and therefore serves as an index of the degree of differentiation.

Element-Zr variation diagrams are constructed with log-log axes so that straight line relationships are defined for non-linear (exponential) behaviour. Linear behaviour is shown by data that falls along trends parallel to lines of equal Zr/element ratios (dashed lines). Note that the vertical scales in Figures 3-3 and 3-4 vary by the same number of log units and allow direct comparison between elements.

The element-Zr variation diagrams are used to distinguish element compatibility relative to Zr. In each diagram the data fall in two distinct groups, coarse-grained plus pegmatitic gabbro and granophyre. Related to the sample groups are two trends of interest that are not indicated on the diagrams because of the inherent

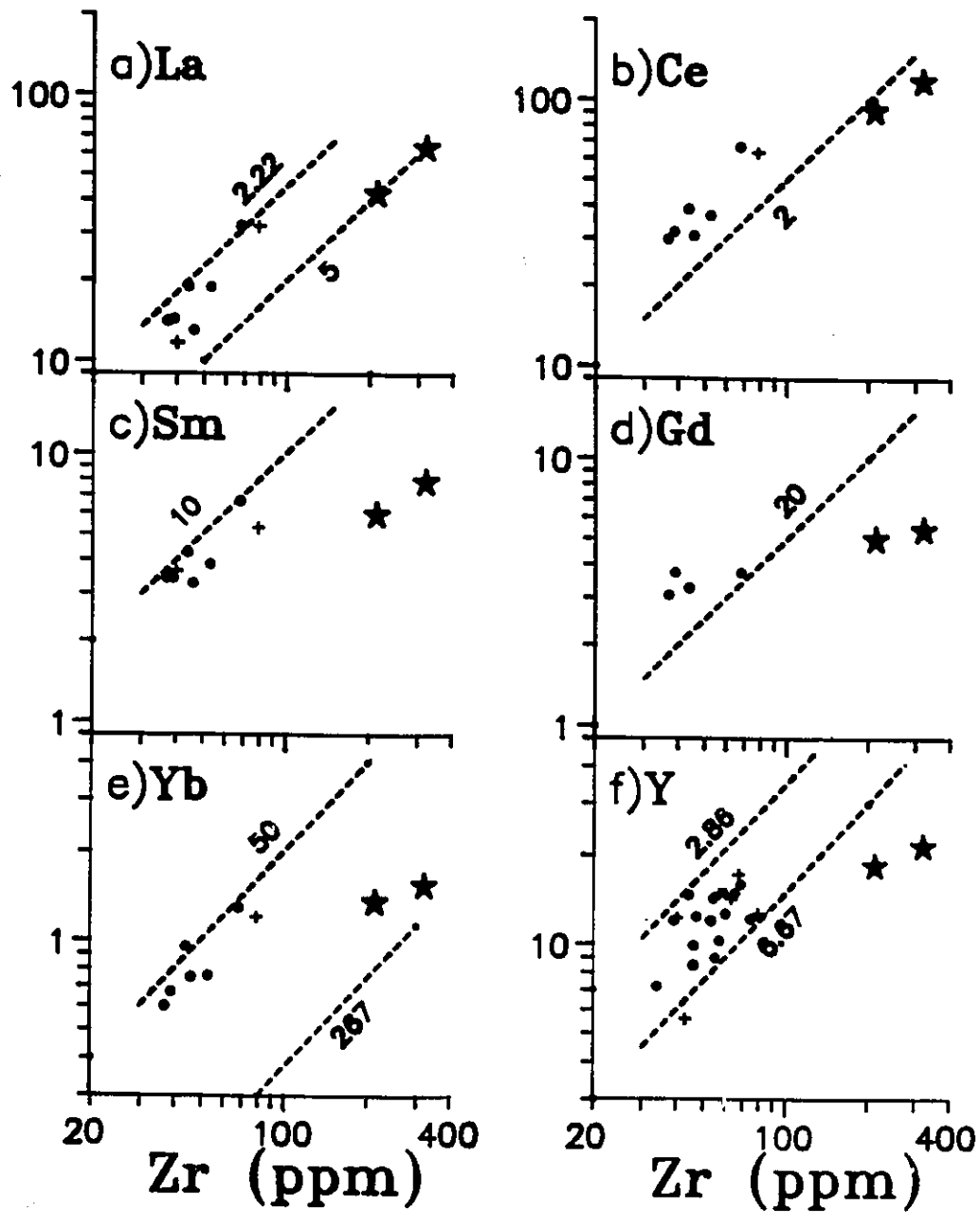


Fig. 3-3: REE-Zr variation diagrams for coarse-grained (dots), pegmatitic (+), and granophyre (stars) facies of TDL gabbro. Lines represent constant Zr/element ratios.

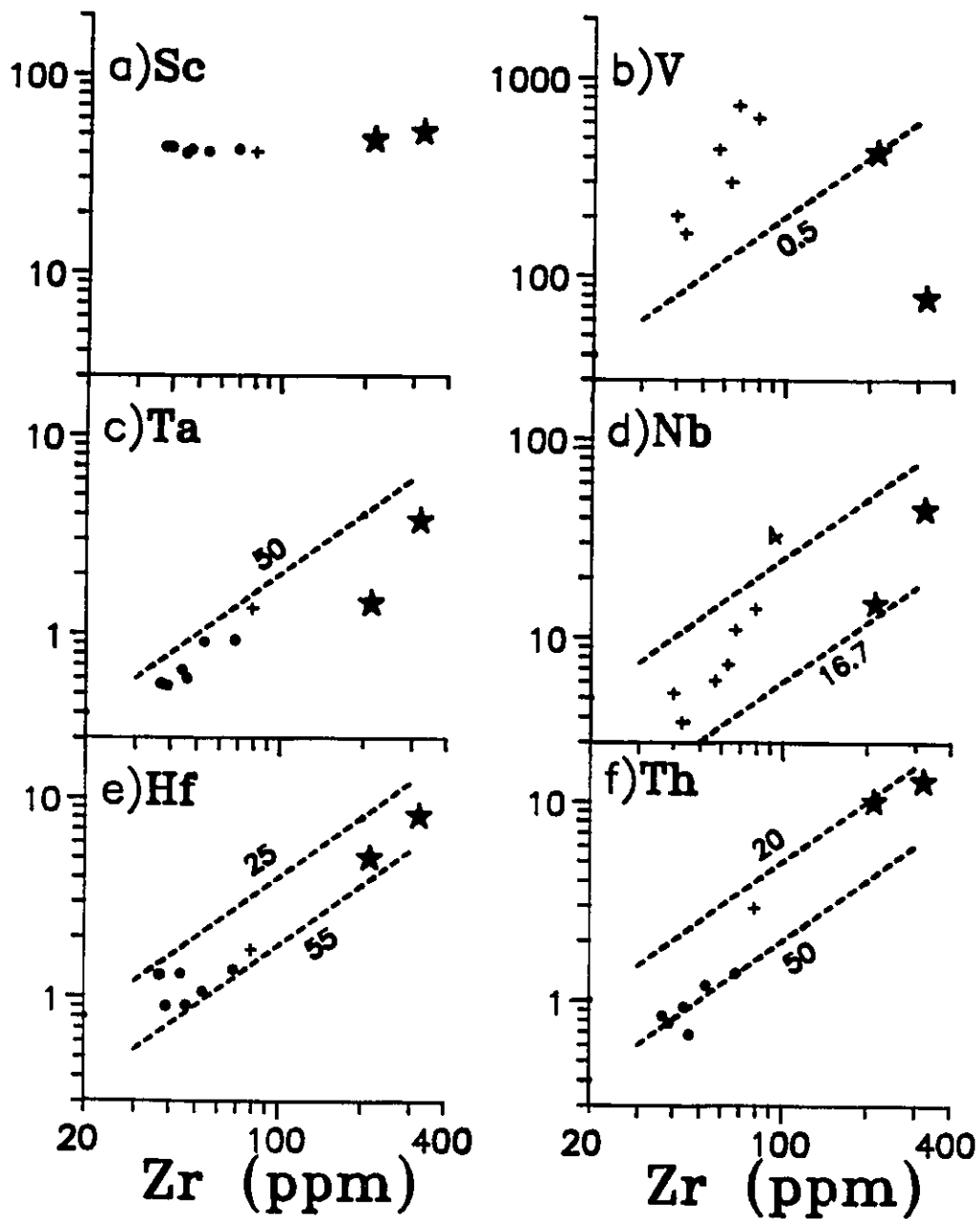


Fig. 3-4: HFSE-Zr variation diagrams for coarse-grained (dots), pegmatitic (+), and granophyre (stars) facies of TDL gabbro. Lines represent constant Zr/element ratios.

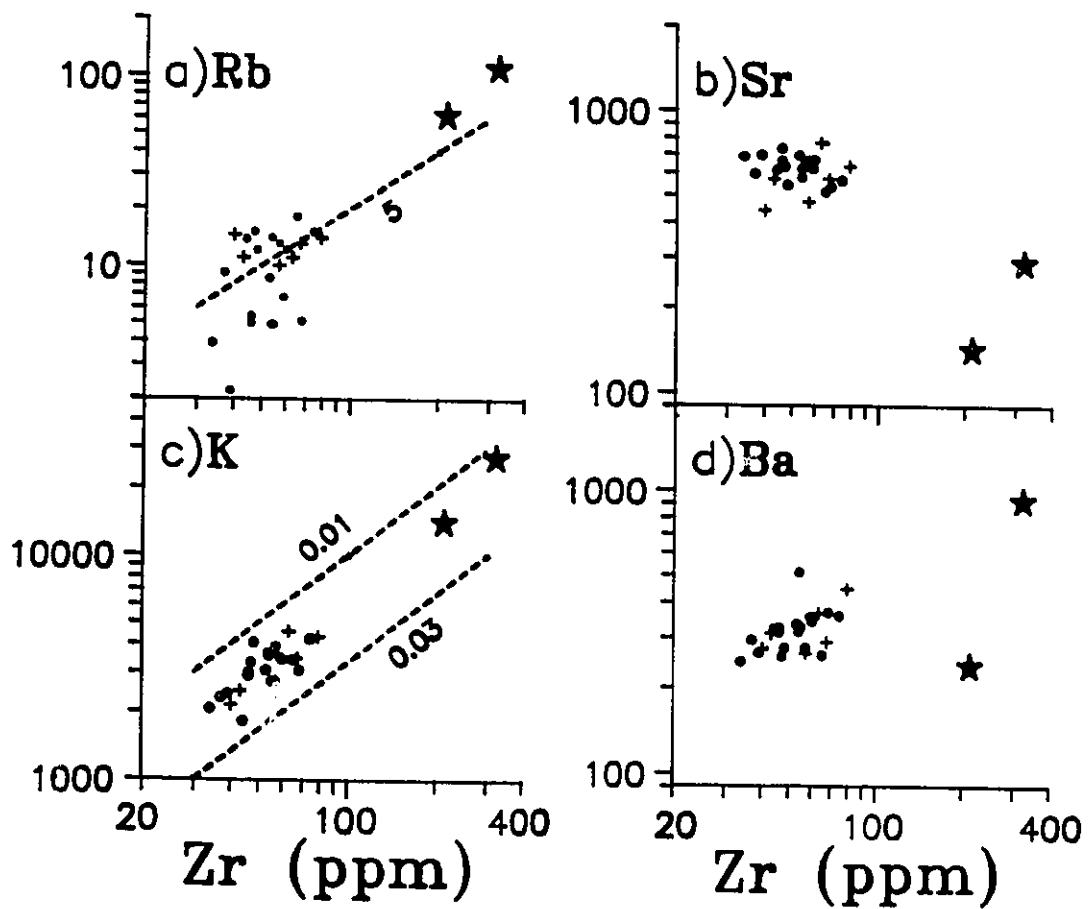


Fig. 3-5: LILE-Zr variation diagrams for coarse-grained (dots), pegmatitic (+), and granophyre (stars) facies of TDL gabbro. Lines represent constant Zr/element ratios.

uncertainty. The first trend is approximately parallel to lines of constant Zr/element ratio and corresponds to the group of gabbro plus pegmatite values. This trend, with the exception of Figure 3-4a (Zr versus Sc) is consistent with the hypothesized control on trace-element concentrations by the initial porosity of the TDL gabbro. The second trend is either parallel to the first trend or exhibits increasing Zr/element ratios, and corresponds to that from average gabbro plus pegmatite values to average granophyre. The value of the diagrams is seen by comparing the two trends. If the two trends are parallel as in Figure 3-4e (Zr versus Hf) and Figure 3-5c (Zr versus K), then the respective elements are considered to have similar weighted partition coefficients. Conversely, if the two trends are not parallel as in Figure 3-3a (Zr versus La) and Figure 3-5b (Zr versus Sr), then the elements have dissimilar weighted partition coefficients. Further, it is possible to distinguish compatible elements ($D > 1$) from those that are incompatible ($D < 1$) by the slope of the gabbro/pegmatite to granophyre trend. For example, the negative slope in Figure 3-4b (Zr versus V) implies that V is compatible. Finally, it is possible to rank the relative compatibilities for elements by comparing gabbro/pegmatite to granophyre trends from one diagram to another. For example, the slope in Figure 3-3a is steeper than in Figure 3-3c and implies that

La behaves more like Zr than does Sm, i.e., La is more incompatible.

With respect to the hypothesized model, observations from Figures 3-3 to 3-5 imply that:

- (a) the weighted partition coefficients of REE are greater than that of Zr,
- (b) the REE are fractionated in the order of decreasing weighted partition coefficients $La=Ce>Yb=Y>Sm=Gd$,
- (c) the weighted partition coefficients of Ta, Nb and Ba are greater than that of Zr, but are similar to those of REE,
- (d) the weighted partition coefficients of Hf, Th, Rb and K are similar to that of Zr, and
- (e) the weighted partition coefficients of Sr and V are significantly greater than that of Zr, and are greater than unity.

The observations from Figures 3-3 to 3-5 are consistent with the model weighted partition coefficients calculated in Table 3-2 and summarized in section A above. Therefore, the proposed model for the origin of granophyre is believed to be relevant.

C - Rayleigh fractionation of the interstitial melt

Assuming that Rayleigh fractional crystallization is a realistic description of interstitial melt crystallization

in the TDL magma then the composition of the interstitial melt will follow the equation:

$$C_L = C_o * F^{D-1}$$

where C_L is the concentration of an element in the interstitial melt, C_o is the initial concentration of an element in the magma, F is the fraction of melt remaining (e.g., $F=0.1$ corresponds to 90% crystallized) and D is the weighted partition coefficient.

It is possible to model the changing trace-element concentrations of interstitial melt using C_o , taken as the average concentration in the TDL gabbro, and D values listed in Table 3-2, and solving for C_L at specific values of F . For simplicity, individual mineral/melt partition coefficients (k_i) and the modal proportion of minerals in contact with the liquid remain constant throughout crystallization. The assumption that C_o is the average composition of TDL gabbro is reasonable because: (a) it was shown in section 3-3-1 that gabbro underwent little vertical fractional crystallization, and (b) the volume of granophyre is negligible compared to the volume of TDL gabbro.

The results of the calculations are shown in Figures 3-6a and b. The diagrams are drawn by joining solutions for C_L at different values of F for each element (lines). Note that the greater the negative slope of the line, the lower the D value of the element, and the intersection of each

line with $F=1$ corresponds to the average content of the respective element in the TDL gabbro (Co).

The approximate fraction of TDL magma corresponding to granophyre is demonstrated graphically by plotting the average of trace-element concentrations from samples F200w and F25 on the appropriate line in Figure 3-6a and b. The spread of values over a range from .08 to .23, excluding heavy REE, is likely due to analytical error and uncertainty in the determination of D values. The results indicate that granophyre corresponds to TDL magma after it was approximately 80 to 90 % crystallized ($F=.1$ to $.2$, excluding heavy REE). The actual fractions are probably closer to the lower limits of the range because the equation:

$$C_L = C_o F^{D-1}$$

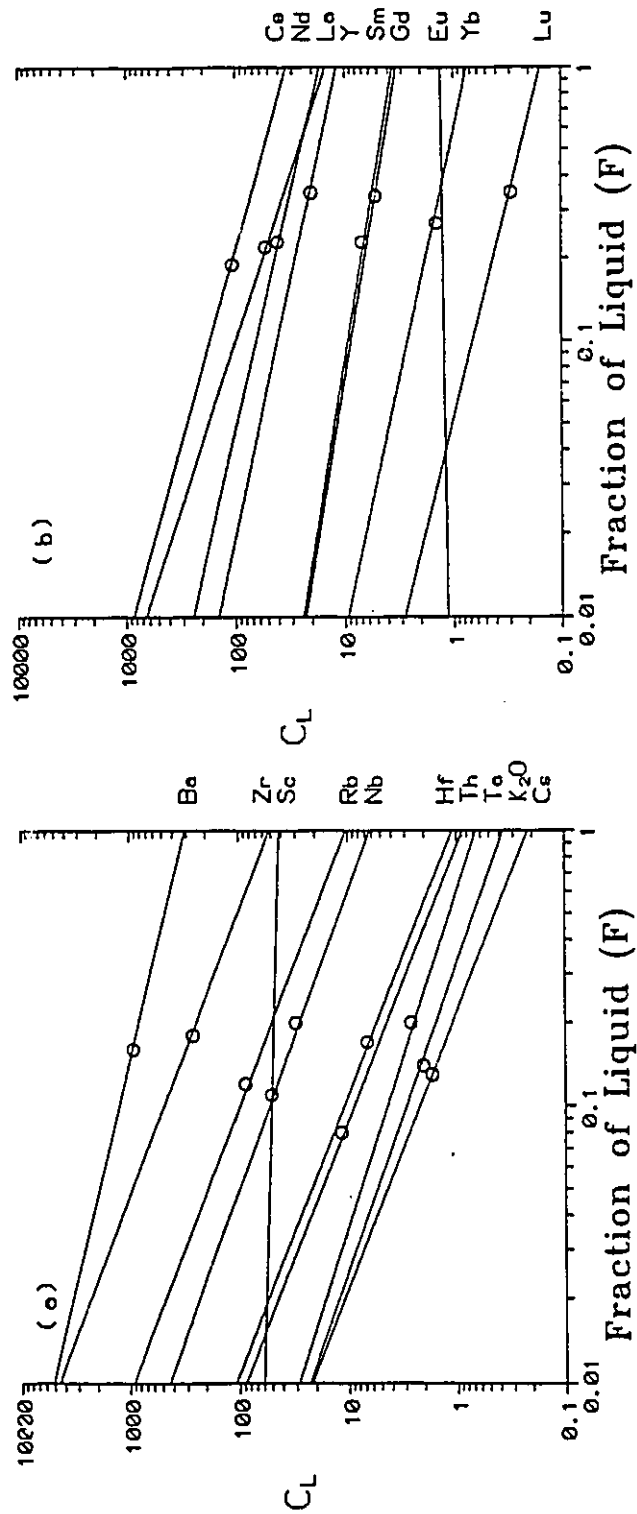
approaches the equation:

$$C_L = C_o / F$$

as D approaches zero. Therefore, the errors inherent to the calculation of weighted partition coefficients become insignificant if D is very small. Consequently, the solutions for Th, Zr and K ($F=.07$, $.15$ and $.09$ for sample F200w, respectively) are probably closer to the true fraction of the TDL magma that crystallized granophyre.

There is a bimodal distribution of F values for the light and heavy REE (Fig. 3-6b). F values for La, Ce, Nd and Sm are distinctly lower than those for Gd, Yb, Y and Lu.

Fig. 3-6: Modelled variation of interstitial melt composition (C_L) during crystallization of the TDL magma. Model assumes Rayleigh fractional crystallization and applies weighted partition coefficients calculated in Table 3-2. F is the fraction of liquid remaining in the crystal mush, e.g., $F=0.1$ corresponds to 10% liquid and 90% crystals. Each line corresponds to the element indicated at the right, and the circles are observed concentration in granophyre.



This discrepancy can be alleviated if the proportion of minerals used to calculate D is changed by reducing the amounts of olivine and plagioclase and increasing the amount of orthopyroxene. This adjustment would increase D values for the heavier REE but not for the lighter REE, and correspond to a reduction of F. Such an increase in the proportion of orthopyroxene in the final stages of crystallization is in general agreement with petrographic observations. However, such fine tuning of the model is not made since increasing its complexity will not change the conclusion that granophyre is representative of approximately 10 % of the TDL magma.

3-3-4 Summary

The following is a summary of the emplacement and subsequent crystallization history of the lower portion of the TDL gabbro, based on geochemical and petrographic observations.

- (1) the lower portion of the TDL gabbro was emplaced as a crystal mush that subsequently crystallized in situ,
- (2) it follows from (1) that concentrations of trace-elements in any given sample will be a function of the amount of interstitial melt (initial porosity), and average trace-element concentrations in all of the gabbro samples will be close to that of the initial TDL magma,

- (3) there was some settling of plagioclase after intrusion, but this is not believed to have any significant affect on the above conclusions,
- (4) the composition of pegmatitic TDL gabbro is not more evolved than the coarse-grained type,
- (5) pegmatite-associated granophyre is genetically related to the TDL magma, and probably formed by the accumulation of TDL magma that was about 90 % crystallized.

3-4 Geochemistry of the Geordie Lake gabbro (MacRae occurrence)

The three stage model proposed in section 2-3-5 for the emplacement and crystallization of the GL gabbro is tested by answering the following questions:

- (a) how does each trace-element behave during crystallization of the GL gabbro,
- (b) are albite pods in the mineralized zone related to the residual melt of the GL magma, and
- (c) was the mineralized zone subjected to metasomatism during the proposed third stage of crystallization?

The first two problems will be approached in a manner similar to that for determining the origin of granophyre in the TDL gabbro. That is, measured trace-element concentrations will be compared to model weighted partition coefficients. The intent is to determine whether

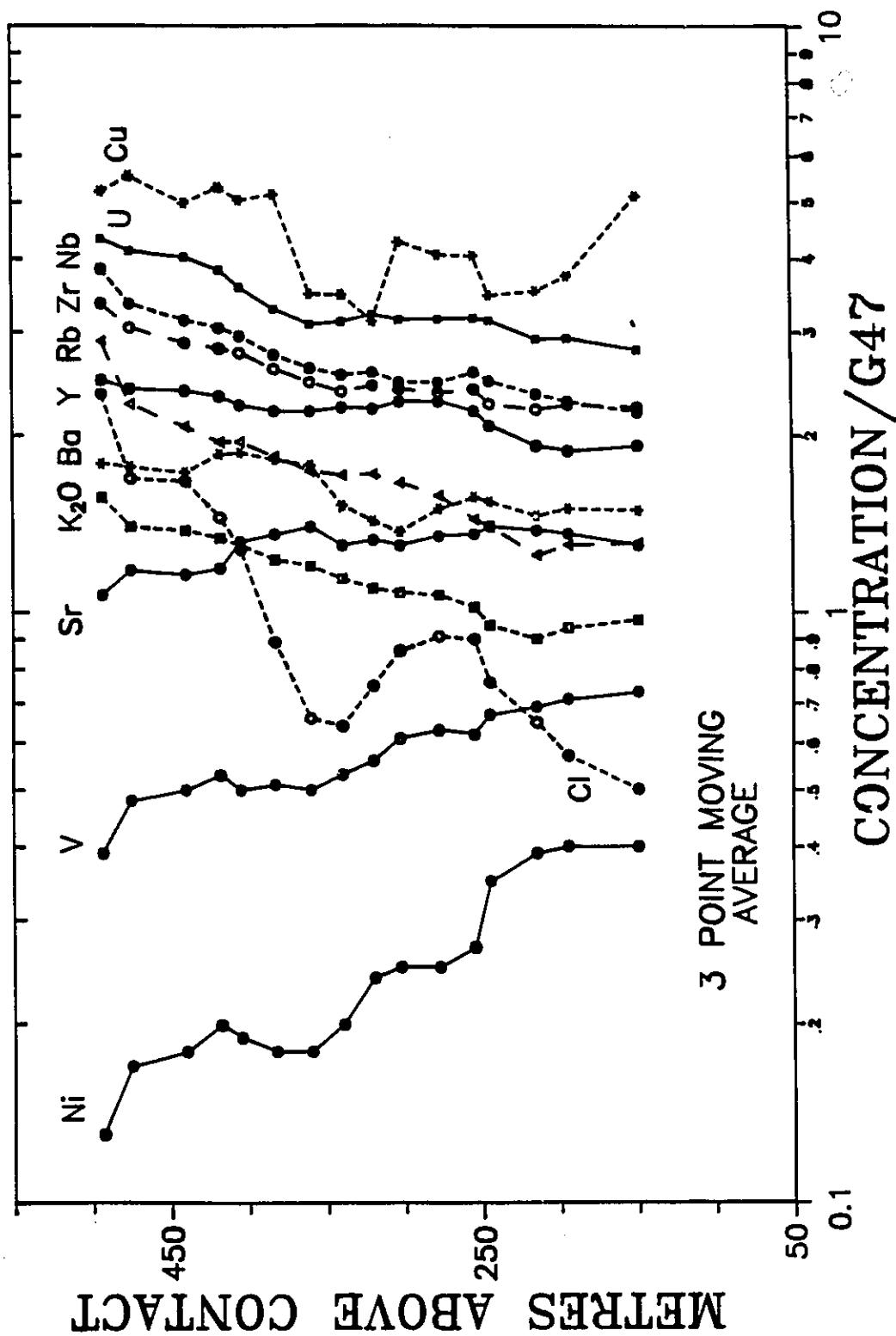
magmatic processes involved in the crystallization of the GL gabbro might be related to the formation of the albitic pods. To recognize such processes a study of unmineralized gabbro is necessary because complexity in the mineralized zone due to modal heterogeneity and overprinting by possible hydrothermal alteration is likely to obscure trace-element trends.

Trace-element data is presented in Tables AI-7 and AI-12 in the appendix and is organized in a manner similar to that used in the description of the TDL gabbro. That is, reference to the elements will be made using the following categories: large-ion lithophile elements (LILE), high field strength elements (HFSE), and Y and rare earth elements (REE).

3-4-1 Cross-section of unmineralized gabbro

A geochemical cross-section of unmineralized gabbro (Samples G1-G18) is presented in Figure 3-7. The elemental trends in Figure 3-7 are 3 point moving average values, i.e., each point is the average of itself plus two neighbouring values. This is done to smooth out the curves and make the trends more prominent. Each value is divided by the respective concentration in sample G47 because G47 appears to have been minimally affected by late silicate melt infiltration. That is, sample G47 has a low concentration

Fig. 3-7: Compositional variation of trace- and minor-elements for Geordie Lake gabbro in the unmineralized zone. Each point is a 3 point moving average. Data are normalized (divided) by the amount in sample G47.



of trace-elements, minimal albite rims on plagioclase, and no visible albite microdikelets.

Based on the slope of the trends in Figure 3-7 it is possible to subdivide the elements into six groups. Each group of elements presumably defines a particular manner of geochemical behaviour. The groups are as follows:

- (a) Cl - the concentration increases significantly up section from sample G18 (520 ppm) to G1 (5140 ppm),
- (b) U, Nb, Zr, Rb and K_2O - concentrations increase up section by 50 to 100 %,
- (c) Cu - the concentration increases up section, however, the trend is more erratic than for the elements in group (b),
- (d) Ba and Y - concentrations increase slightly up section,
- (e) Sr - the concentration is approximately constant through much of the section but decreases near the top,
- (f) Ni and V - concentrations decrease rapidly from the bottom to top of the section.

3-4-2 Genesis of the unmineralized gabbro

The trace-element trends are consistent with decreasing normative Mg/Fe in Figure 2-14, and resemble those of a fractionating silicate magma. The trends cannot have been caused by the emplacement and in-situ crystallization of a plagioclase crystal mush. Such a

process would result in the near parallel trends for all elements. It is also unlikely that the patterns are a result of metasomatism by a migrating hydrothermal fluid because trends for elements that are typically mobile in hydrothermal fluids (K_2O and Rb) closely match those for elements that are relatively immobile (e.g., Nb and Zr).

There are two possible sequences of events that could account for the trace-element behaviour in the unmineralized zone. The first is the formation of gabbro by settling out of plagioclase, magnetite, apatite and clinopyroxene from a magma column. In this case the residual melt becomes progressively fractionated and major minerals less basic. A second scenario involves two subsequent steps. In the first step gabbro formed by intrusion of a plagioclase crystal mush and subsequent crystallization without settling out of minerals. In the second step significant amounts of interstitial melt moved upward through the crystal pile and reacted with the crystal pile, thereby becoming progressively fractionated. Eventually, porosity gets too low and migration of interstitial melt ends. The latter hypothesis is favoured because textural evidence in Chapter two suggests that the original interstitial melt was affected by a late event of silicate melt infiltration. In either case the behaviour of trace-elements is a function of the crystallization of the

GL gabbro and, therefore, model weighted partition coefficients can be derived and then used to predict the composition of the residual magma. In this way it is possible to determine whether albitic pods in the mineralized zone are representative of residual GL magma.

3-4-3 Mineralized zone

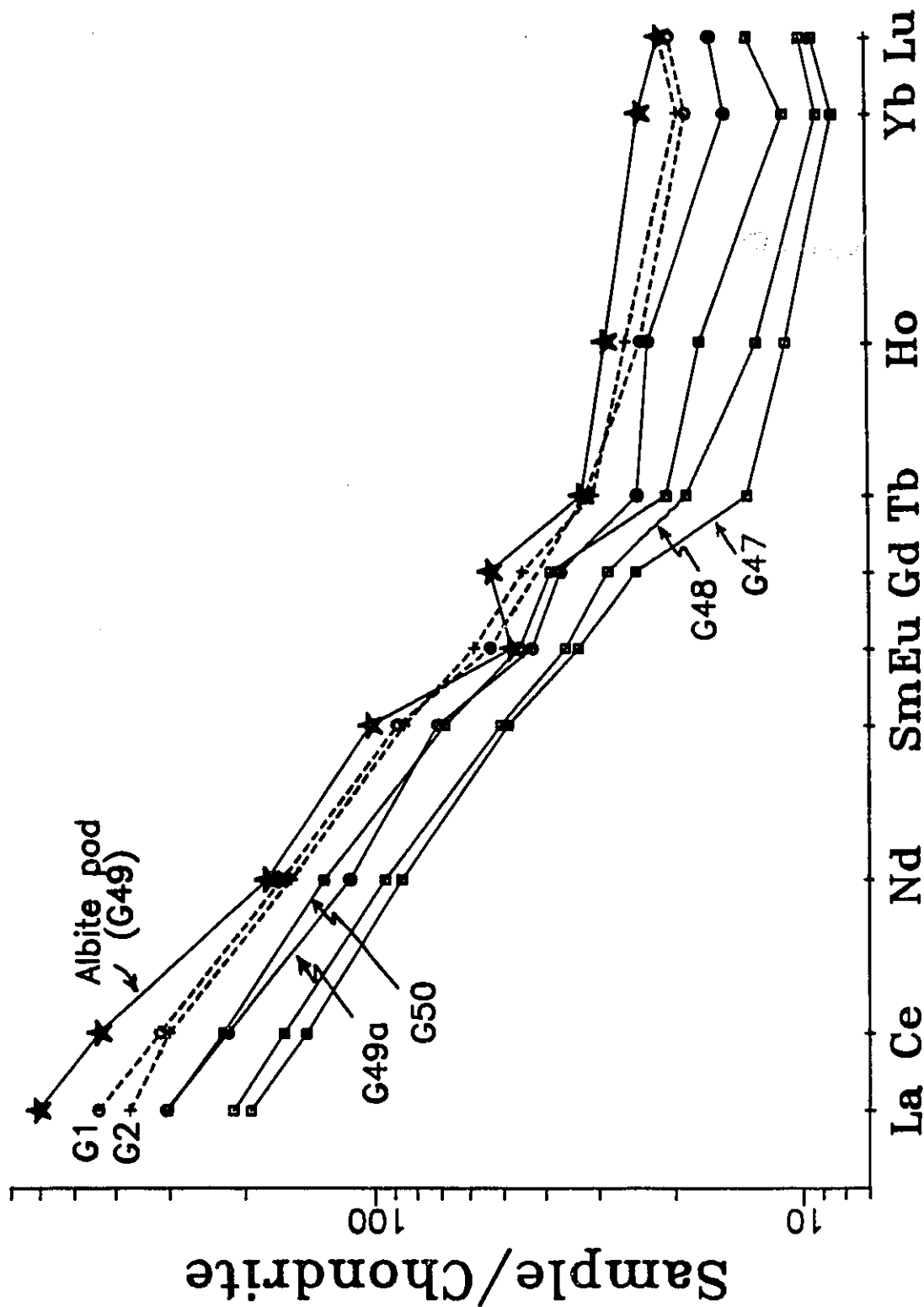
It was proposed in section 2-3-5 that albite microdikelets and pods in the mineralized zone represent accumulations of interstitial melt that migrated through the crystal pile. This hypothesis will be tested by describing the geochemistry of the mineralized zone in terms of the relative compatibilities of trace-elements defined in the unmineralized gabbro.

3-4-4 Rare earth elements

Four types of rocks from the GL gabbro are depicted in the chondrite normalized REE diagram (Fig. 3-8): (a) gabbro from the unmineralized zone (samples G1 and G2), (b) gabbro from the mineralized zone that contains no visible albite microdikelets (G47), (c) gabbro from the mineralized zone that contains visible albite microdikelets (G48, G49a and G50), and (d) an albite pod (G49).

The similar patterns for samples in Figure 3-8 indicate that the residual melt in the unmineralized zone is

Fig. 3-8: Chondrite normalized REE for Geordie Lake gabbro and albite pod (G49). Samples G49a and G50 contain albite microdikeylets.



indeed, as hypothesized, similar to that which crystallized the albitic microdikelets and pods. There are, however, two differences between the sample groups. The first is the negative Eu anomaly shown by the albitic pod. The second is the apparent enrichment in La and Ce over the middle REE in the albitic pod relative to gabbro. These observations are accounted for by fractionation in section 3-4-5 and are consistent with the initial hypothesis.

3-4-5 Origin of albite pods

Based on evidence from REE data it is apparent that albite pods are genetically related to the GL gabbro. This observation is consistent with the premise that albite pods were formed by migration of the interstitial melt through the crystal pile to accumulate in pods. This hypothesis can be tested semi-quantitatively by:

- (a) determining weighted partition coefficients, and
- (b) comparing D values to measured trace-element concentrations.

A Determination of partition coefficients

If interstitial melt migrates through the crystal pile then its composition will be controlled by the minerals present in the crystal pile. Therefore, melt-gabbro weighted partition coefficients for trace-elements can be

derived. The model weighted partition coefficients are calculated (column 3 in Table 3-2) in a similar manner as described for the TDL gabbro in section 3-3-3A, assuming the proportions of crystals are 6% olivine, 40% clinopyroxene, 44% plagioclase, 1% apatite and 9% magnetite plus ilmenite. This composition is similar to the normative abundance of minerals in unmineralized gabbro (Fig. 2-12), except it excludes K-feldspar and increases the abundance of pyroxene from about 30% to 40%.

Based on the calculated weighted partition coefficients (Table 3-2) the elements can be subdivided into four groups. The groups are as follows:

- (a) strongly incompatible elements ($D < 0.1$) - Cs, Rb, K, U, Th, Zr, and Hf,
- (b) moderate to weakly incompatible elements ($1 > D > 0.1$)
Ba, Nb, Ta, REE (except Eu), and Y,
- (c) weakly compatible elements ($1 < D < 2$) - Sr, Eu, V and Sc,
and
- (d) moderately compatible elements ($D > 1$) - Ni.

The results of this exercise are important because the calculated D values approximately describe the behaviour of elements in the unmineralized gabbro (section 3-4-1).

B Comparison of trace-element data to model D values:

Element-Zr variation diagrams

Element-Zr variation diagrams are used extensively in the description of the TDL gabbro in section 3-3-3B, and the reader is directed to the opening remarks there on the usefulness of these diagrams.

Element-Zr variation diagrams for samples of GL gabbro and albite pod are shown in Figures 3-9 to 3-11. Many of the observations noted from element-Zr variation diagrams for TDL gabbro (section 3-3-3B) also apply to the GL gabbro. With respect to the hypothesized model, observations from Figures 3-9 and 3-10 imply that:

- (a) the weighted partition coefficients of REE are greater than that of Zr,
- (b) the REE are fractionated in the order of decreasing weighted partition coefficients $La=Ce>Yb=Y>Sm=Gd$,
- (c) the weighted partition coefficients of Ta and Ba are greater than that of Zr, but are similar to those of REE,
- (d) the weighted partition coefficients of Nb, U, Hf, and Th are similar to that of Zr, and
- (e) the weighted partition coefficients of Sc and V are significantly greater than that of Zr, and are greater than unity.

The observations from Figures 3-9 and 3-10 are consistent with the model weighted partition coefficients

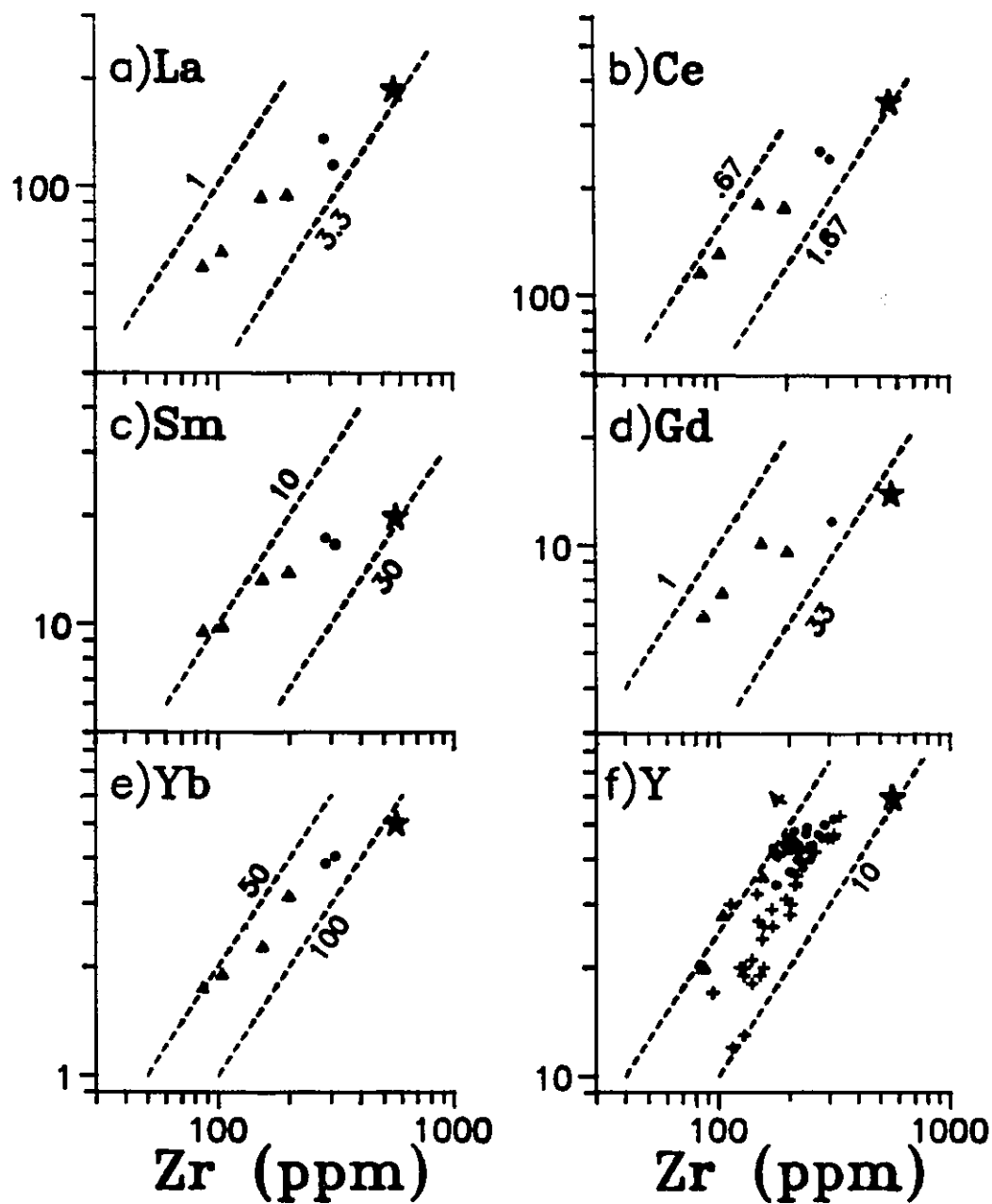
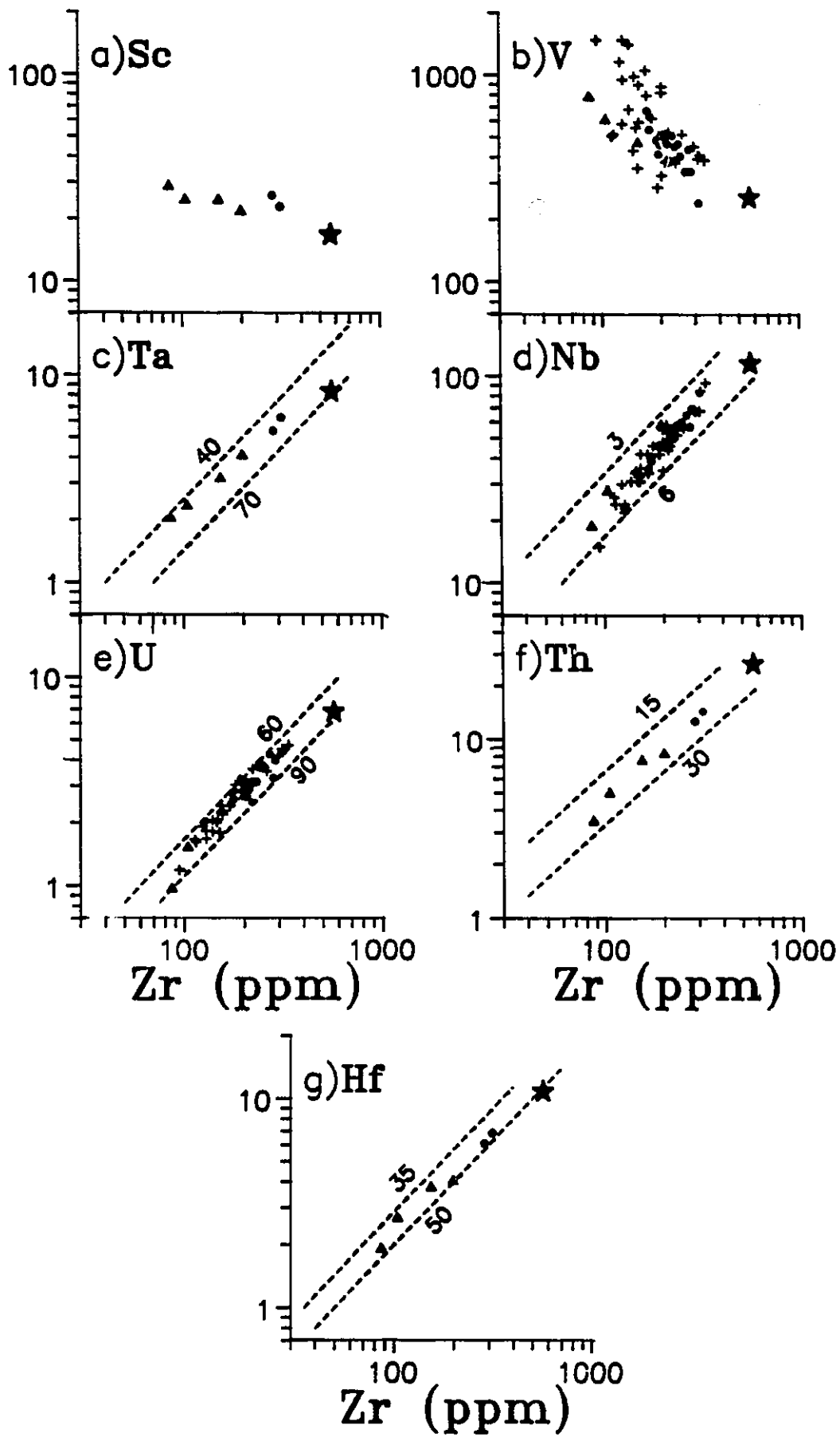


Fig. 3-9: REE-Zr variation diagrams for GL gabbro in unmineralized zone (dots); GL gabbro in mineralized zone (+); GL gabbro with rare (G47 and G48) to abundant (G49a and G50) albite microdikelets (triangles); and, albite pod (star). Lines represent constant Zr/element ratios.

Fig. 3-10: HFSE-Zr variation diagrams for Geordie Lake gabbro in unmineralized zone (dots); GL gabbro in mineralized zone (+); GL gabbro with rare (G47 and G48) to abundant (G49a and G50) albite microdikelets (triangles); and, albite pod (star). Lines represent constant Zr/element ratios.



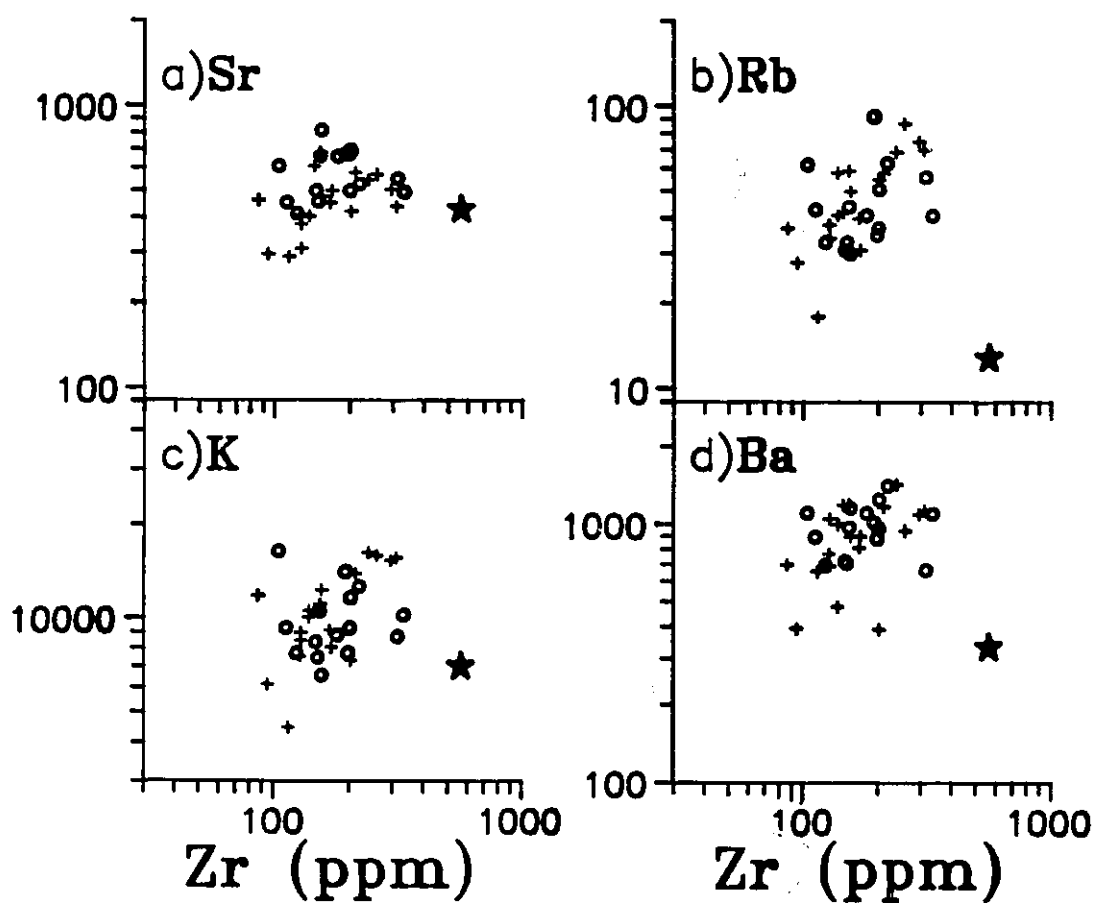


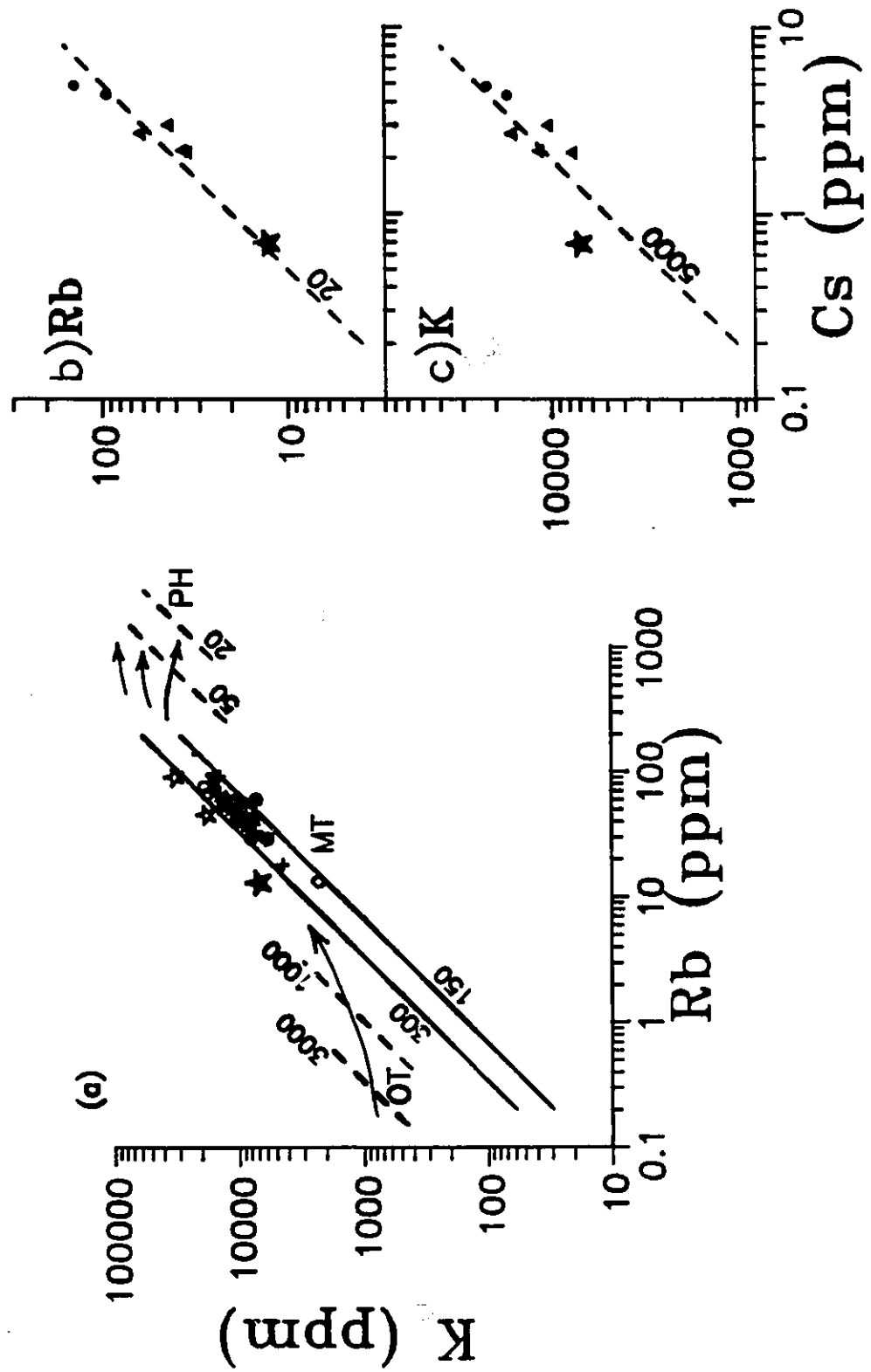
Fig. 3-11: LILE-Zr variation diagrams for GL gabbro in the mineralized zone **only**. Symbols: gabbro, +; gabbro with visible albite microdikelets, circles; and, albite pod, star.

calculated in Table 3-2 and summarized in section A above. Therefore, the proposed model for the origin of albite pods is believed to be relevant. However, observations from LILE-Zr variation diagrams for samples of gabbro in the mineralized zone (Figure 3-11) are inconsistent with this hypothesis. In Figure 3-11b and c, there appears to be a weak positive correlation between Zr and Rb, and Zr and K for samples of gabbro without albite microdikelets (+ symbols), but similar relationships do not exist for samples that contain albite microdikelets (circles). Further, the albite pod sample is depleted in Rb and K, relative to gabbro. Therefore, the concentrations of Rb and K are inconsistent with model D values. One possible explanation for this inconsistency is that albite pods and gabbro with albite microdikelets were affected by metasomatism. This is reasonable since LILE are typically more mobile in hydrothermal fluids than HFSE or REE, and are, therefore, more susceptible to redistribution during hydrothermal alteration.

C K-Rb fractionation

The behaviour of alkali metals is further examined in the Figure 3-12a to c. In Figure 3-12a data for all of the GL gabbro samples, excluding albite pods, fall along the main trend for igneous rocks as defined by Shaw (1968), and

Fig. 3-12: LILE-Zr variation diagrams for Geordie Lake gabbro in unmineralized zone (dots); GL gabbro in mineralized zone (+); GL gabbro with visible albite microdikelets (circles); GL gabbro samples G47 to G50 (triangles); albite pod analysed in this study (filled star); and, albite pod analysed by Mulja (1989) (hollow star).



the K/Rb ratio is approximately constant. A smaller set of samples shown in Figures 3-12 b and c indicates that Rb/Cs and K/Cs for the GL gabbro, excluding the albite pod, are also approximately constant. Therefore, it appears that K, Rb and Cs in the GL gabbro, excluding albite pods, are behaving coherently.

Three samples of albite pod are shown in Figure 3-12a: the solid star is from this study and the two hollow stars are from Mulja (1989). Data from Mulja (1989) are used to verify the results of the single sample (G49) analysed here. These data clearly show that K:Rb and K:Cs ratios for albite pod samples are greater than those for gabbro, and Rb:Cs is approximately constant. This implies that Rb and Cs are fractionated from K during the formation of the albite pods. The high K:Rb ratio of albitic pods is unusual in that it typically decreases with increasing fractional crystallization following the pegmatitic and hydrothermal trend as defined by Shaw (1968).

D Discussion

Based on the composition of feldspar (98-100% albite, section 2-3-4) it is unlikely that the feldspar in albite microdikelets and pods crystallized from a silicate melt. On this basis, a hydrothermal origin for albite pods was proposed by Mulja and Mitchell (1990). They proposed

that albite pods were formed by the destruction of original textures of the GL gabbro and the deposition of albite plus amphibole during intense metasomatism. However, the origin of albite pods is probably more complex than this for several reasons: (a) the high concentrations of, and linear correlations between, relatively immobile trace-elements, such as Nb, U, Th, Zr and Hf are consistent with an origin of albite pods from a highly evolved silicate melt, and (b) textural evidence described in section 2-3-3 suggests that albite pods formed by emplacement of a silicate melt into a crystal mush. Therefore, it is concluded that albite pods must have formed by a multiple stage process.

The following is a proposed two stage process to form albite pods. In the first step sodic plagioclase crystallized from the infiltrated, highly evolved volatile-rich silicate magma. At some point during crystallization, an immiscible vapour phase separated from the silicate magma. In step two the immiscible vapour equilibrated with early formed plagioclase, thereby removing K, Rb, Cs and, probably, Ca and Ba, leaving nearly pure albite. Based on K-Rb and K-Cs fractionation (section C), the order of fractionation of the alkali metals from feldspar into the vapour is, in descending order, Cs=Rb>K>>Na. This order of partitioning is consistent with experimental work by Beswick (1973). Beswick (1973) determined that in experimental

studies of the distribution of Rb and K between sanidine and vapour, K favours the feldspar and Rb the vapour, i.e., for Rb-K exchange, $K_D^{S/V} < 1$. Although the experimental partition coefficients were found to vary with temperature and the Rb/K ratio in sanidine, the above relationship still held. It should be emphasized that the above experiment applied to sanidine and not albite; however, the order of increasing ionic radii from Na to Cs imply that similar experiments with albite would yield similar results.

3-4-6 Summary

From the observations above and in Chapter two, the following conclusions are reached with respect to the emplacement and subsequent crystallization of the GL gabbro.

- (1) the GL gabbro was emplaced as a crystal mush, probably having a homogeneous composition, and began to crystallize in situ,
- (2) the normal crystallization sequence was interrupted by the infiltration of a highly evolved, possibly volatile-rich silicate magma into the interstices of the original minerals,
- (3) in some locations the infiltration was forceful and resulted in the formation of heterogeneous textures and composition,

(4) local accumulations of infiltrated melt crystallized microdikelets and pods consisting of saccharoidal sodic feldspar,

(5) a vapour phase separated from the infiltrated magma during feldspar crystallization and reacted with the feldspar, thereby removing K, Rb, Cs and, probably, Ba and Ca, leaving feldspar with a composition of 98-100 % albite,

(6) migration of the evolved vapour into the crystal pile resulted in the formation of interstitial amphibole and amphibole alteration rims on clinopyroxene.

CHAPTER 4 - Sulfides and PGE Distribution

4-1 Introduction

Previous work at both the Marathon deposit and the MacRae occurrence by Ohnenstetter et al. (1989), Ohnenstetter & Watkinson (1991), Mitchell et al. (1989), and Mulja & Mitchell (1990) showed that platinum-group elements (PGE) occur in a complex suite of platinum-group minerals (PGM) that are spatially associated with sulfides, predominantly chalcopyrite. It appears, therefore, that the genesis of PGE mineralization is related to that of sulfides. In this chapter sulfide-silicate textural relationships, and the distribution of ore-forming elements (S, Ni, Cu, PGE and Au) at the two deposits are described. The objective is to determine the most probable mode of PGE deposition in each deposit.

4-2 Data

Forty-one samples from the Marathon deposit and eighty-four samples from the MacRae occurrence were analysed for Pb, Zn, Ni, Cu, S, Ir, Rh, Pt, Pd and Au. Lead, Zn, Ni, Cu and S were analysed by XRF. The PGE and Au were analysed by a method of fire assay preconcentration and instrumental neutron activation analyses after Hoffman et al. (1978). Details of analytical methods are found in Appendix I.

Sulfur, Pb, Zn, Cu, Ni, Ir, Rh, Pt, Pd, and Au concentrations, and estimated Ni concentrations in sulfides (see below) in samples from the Marathon deposit are listed in Table 4-2. Sulfur, Pb, Zn, Cu, Ni, Ir, Rh, Pd, and Au concentrations in mineralized GL gabbro samples and average values for unmineralized samples are listed in Table 4-5.

4-3 Platinum-group minerals

The suites of PGM found in the Marathon and MacRae properties (Ohnenstetter et al. 1989; Ohnenstetter & Watkinson 1991; Mitchell et al. 1989; Mulja and Mitchell 1990) are summarized in Table 4-1. In general, the suite of platinum-group, Au and Ag minerals for the Marathon deposit is different from that of the MacRae occurrence, although there are six minerals common to both deposits. Te-, Sb- and As-bearing PGM occur in both deposits, but only the MacRae occurrence contains Bi-bearing minerals. Other minerals present include clausthalite (PbSe) (Ohnenstetter et al. 1989) and $\text{Re}(\text{Mo,Cu,Fe})\text{S}_3$ (Mitchell et al. 1989) in the Marathon deposit, and Pd-bearing (up to 10%) melonite (NiTe_2) in the MacRae occurrence (Mulja and Mitchell 1990).

The PGM assemblages in both deposits are characterized by complex intergrowth relationships. This feature suggests that PGM growth follows an intricate paragenesis, as shown by Mulja & Mitchell (1990) for the

MacRae occurrence. The complex paragenesis for PGM at the Marathon deposit, strong zonation (Ohnenstetter et al. 1989), and extensive solid solution (Ohnenstetter & Watkinson 1991) for some PGM led Ohnenstetter & Watkinson (1991) to suggest that the origin of PGM is inconsistent with simple exsolution from magmatic sulfides.

TABLE 4.1. Comparison of platinum-group minerals from the Marathon deposit and MacRae occurrence.

Mineral	Formula	MARATHON DEPOSIT ¹	MACRAE OCCURRENCE ²
Temagamite	Pd ₃ HgTe	X	
Altaite	AgTe	X	
Isomertierite	Pd ₁₁ Sb ₂ As ₂	X	
Mertierite II	Pd ₈ Sb ₃	X	
Atokite	Pd ₃ Sn	X	
Zvyagintsevite	Pd ₃ Pb	X	
Hollingworthite	RhAsS	X	
Electrum	Au, Ag	X	
Clausthalite	PbSe	X	
Kotulskite	PdTe	X	X
Merenskyite	Pd ₂ Te	X	X
Sperrylite	PtAs ₂	X ₃	rare
Hessite	Ag ₂ Te	X ³	X
Paolovite	Pd ₂ Sn	X ³	X
unnamed PGM	Pd _{1.6} As _{1.5} Ni	X ²	X
Michenerite	PdBiTe		X
Pd-Bismuthotelluride	Pd ₈ Bi ₆ Te ₃		X
Sopcheite	Ag ₄ Pd ₃ Te ₄		X
Guanglinite	Pd ₃ As		X
Palladium Arsenide	Pd-As		X
Palladium Antimonide	Pd-Sb		X
unnamed Ag telluride	Ag ₃ Te ₂		X

¹ Ohnenstetter et al. 1989, ² Mulja and Mitchell 1990,
³ Mitchell et al. (1989)

4-4 Petrography of sulfides at the Marathon deposit

Sulfides at the Marathon deposit consist of chalcopyrite, pyrrhotite, minor pentlandite and accessory pyrite and cubanite. They occur predominantly in the lower zone of the Two Duck Lake gabbro, but also in old gabbro xenoliths and locally within the Archean basement.

Within the TDL gabbro sulfides occur in two discrete zones of disseminated mineralization. The main sulfide zone is in the central portion of the TDL gabbro and is the prominent host of Cu and PGE in the deposit. The second sulfide zone is thinner than the main zone and occurs near the base of the intrusion. It is referred to as the basal zone.

4-4-1 Main sulfide zone

The sulfides in the main zone consist of chalcopyrite \geq pyrrhotite \gg pentlandite $>$ cubanite \geq pyrite, and occur in disseminated lenses within coarse-grained to pegmatitic gabbros. The total sulfide content of the rocks ranges up to approximately 8 %. The sulfides occur in angular, interstitial monomineralic blebs or polycrystalline aggregates that are generally less than .3 to .5 cm in size, but some are up to 1 or 2 cm across.

The proportions of the main minerals chalcopyrite and pyrrhotite is highly variable in the small,

polycrystalline sulfide blebs and may range from pure chalcopyrite to pure pyrrhotite, whereas larger blebs are somewhat more homogeneous and have roughly equal amounts of each mineral. Based on whole rock data, the chalcopyrite/pyrrhotite ratio (weight %, calculation follows that in section 4-5-5) varies between 0.8 and 2.8, and the average is 1.2 ± 0.6 for 12 samples with greater than two wt. % sulfides or 0.75 wt % sulfur. Therefore, although the chalcopyrite/pyrrhotite ratios are locally erratic at the thin section scale, the average ratio of samples are relatively constant.

There are three prominent features exhibited by the sulfides that are relevant to their paragenesis. The first is the association of sulfides with a large variety of silicate minerals and magnetite. In coarse-grained gabbro the associated silicates are, in decreasing order of abundance, plagioclase, clinopyroxene, biotite, amphibole, olivine, and chlorite. The order in pegmatitic TDL gabbro is amphibole, plagioclase, altered plagioclase, biotite, chlorite, and clinopyroxene. Magnetite and calcite are also found in contact with sulfides in pegmatite. The sulfides are interstitial to anhydrous silicates and magnetite, but are commonly intergrown with hydrous silicates. The association with hydrous minerals led Watkinson et al. (1986) to infer that sulfides were deposited from a hydrous

phase at subsolidus temperatures. However, this seems unlikely given that the majority of sulfides are in contact with primary, anhydrous minerals that are typically unaltered. It is more likely that an interstitial, immiscible sulfide liquid was present during crystallization of the TDL gabbro.

The second feature is that large aggregates of sulfide are typically zoned with cores of pyrrhotite and rims of chalcopyrite (Fig. 4-1b). An important feature of these aggregates is the embayment and corrosion of pyrrhotite by chalcopyrite (Fig. 4-1b), suggesting disequilibrium. Therefore, it appears that a Cu-rich sulfide liquid, locally not at equilibrium with pyrrhotite, migrated through the gabbro after the deposition of pyrrhotite. This feature is consistent with local, erratic variations of chalcopyrite/pyrrhotite ratios.

The third important feature is the inclusion of chalcopyrite in the margins of plagioclase crystals (Fig. 4-1 a to d). In Figures 4-1c and d the chalcopyrite-rich inclusions are clearly associated with resorption of early plagioclase and deposition of later, more calcic plagioclase. It was proposed in section 2-2-3E that resorption and late plagioclase was coincident with, or occurred prior to, intrusion of the TDL magma into its present site. It is suggested, therefore, that the

Fig.4-1: Examples of common sulfide-sulfide and sulfide-plagioclase textures in main zone sulfides of coarse-grained TDL gabbro.

A. Photograph of thin section from sample F8c. Gabbro exhibits orthocumulate texture, and consists of plagioclase (white), olivine (ol), clinopyroxene (px), minor amphibole and biotite (< 2 or 3%). The opaques consist predominantly of approximately equal proportions of chalcopyrite and pyrrhotite, and minor spinel.

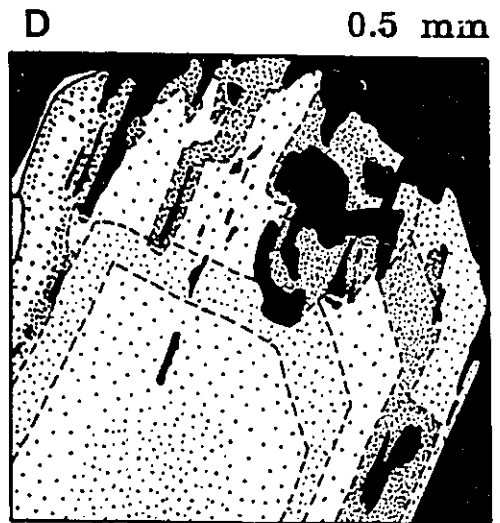
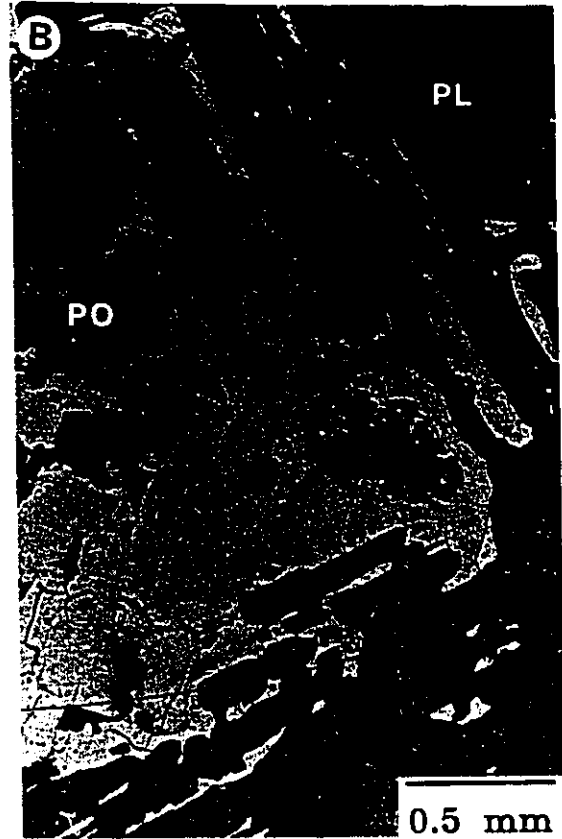
B. Photomicrograph of inset from A in reflected light showing two important textures. The first texture is pyrrhotite (grey) surrounded and partly resorbed by chalcopyrite (light grey). The two grains of pyrrhotite are optically continuous (based on pleochroism), and, therefore, formed part of a single grain that was cut by chalcopyrite. A third pyrrhotite grain located in the lower left is rotated away from darker pleochroic position and is difficult to distinguish from chalcopyrite. The second important texture is the inclusion of chalcopyrite in the margins of neighbouring plagioclase. This texture is examined more closely in C and D.

C. Photomicrograph of zoned plagioclase crystal, located immediately to the left of cpy label in A, in transmitted light. The crystal exhibits an embayment in the plagioclase that is filled with later plagioclase (white) intergrown with chalcopyrite (black). The embayment was formed by resorption that cuts across pre-existing zoning in the plagioclase. A late chloritic veinlet (white) cuts chalcopyrite near the top of the photo and continues along the contact between plagioclase and chalcopyrite.

D. Composition map of plagioclase crystal from C and A, determined by microprobe spot analyses. The composition is indicated by dot density with higher density indicating higher An content, e.g., the inner zone grades from An₆₅ in the core to An₆₁. The lowest An content in the crystal is An₅₇, and the highest, located in embayments, is An₇₆.



C



chalcopyrite mineralization must have been deposited at about the same time. This hypothesis is important because it negates the possibility that chalcopyrite mobilization after solidification of the TDL gabbro was an important process in concentrating sulfides and PGE.

4-4-2 Basal sulfide zone

The sulfides in the basal zone (samples F29 to F32) are compositionally and texturally different than those in the main zone. These sulfides consist of pyrrhotite > chalcopyrite >> pyrite > pentlandite. The calculated chalcopyrite/pyrrhotite ratio (in weight %) is $0.28 \pm .04$, a value that is approximately four times lower than the average value calculated for samples in the main zone. This ratio and the order of abundance of sulfide minerals indicates that the basal zone sulfide melt contained more S and Fe, and less Cu and Ni than that which formed the main zone.

Pyrrhotite and chalcopyrite in the basal zone are interstitial and anhedral, but show only minor core-to-rim zonation, a feature that is common in the main zone. Silicates in contact with sulfides are similar to those of the main zone. Chalcopyrite is included in plagioclase rims, although less commonly than in the main zone.

4-4-3 Other sulfides

Low concentrations of disseminated sulfides occur locally in Eastern gabbro xenoliths and also in association with microdikelets of TDL gabbro intruding xenoliths. The sulfides in the former are fine-grained, subhedral, interstitial, disseminated grains with pyrrhotite > chalcopyrite ≥ pyrite. Sulfides associated with dikelets of TDL gabbro consist predominantly of chalcopyrite.

Minor sulfides occur in the Archean country rock, and consist predominantly of pyrite and pyrrhotite. They are not considered further.

4-4-4 Phase relationships and temperatures of sulfide formation

Sketches of phase relationships in the Cu-Fe-Ni-S system at 1000°C (after Craig & Kullerud, 1969), and in the Cu-Fe-S at 300°C (after Craig & Scott, 1974) demonstrate a possible sequence of crystallization for the TDL sulfide liquid (Fig. 4-2 a and b). The average composition of the TDL sulfide liquid, 11.4 mol% Cu, 0.3 mol% Ni, 34.8 mol% Fe and 53.5 mol% S, is located on both diagrams.

A proposed paragenesis, including respective temperatures (references cited in Craig & Kullerud 1969, or Craig & Scott 1974) for solidification of the TDL bulk sulfide liquid is as follows:

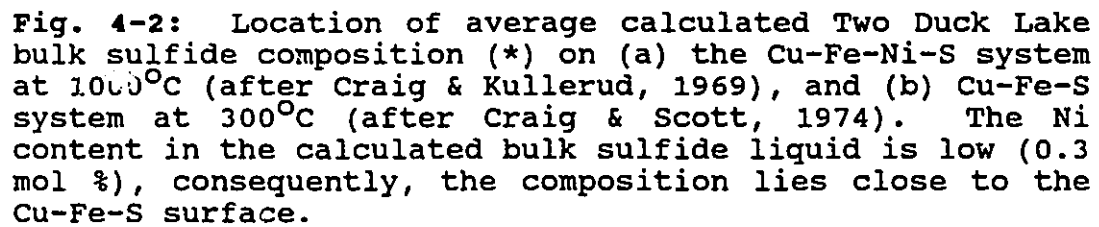
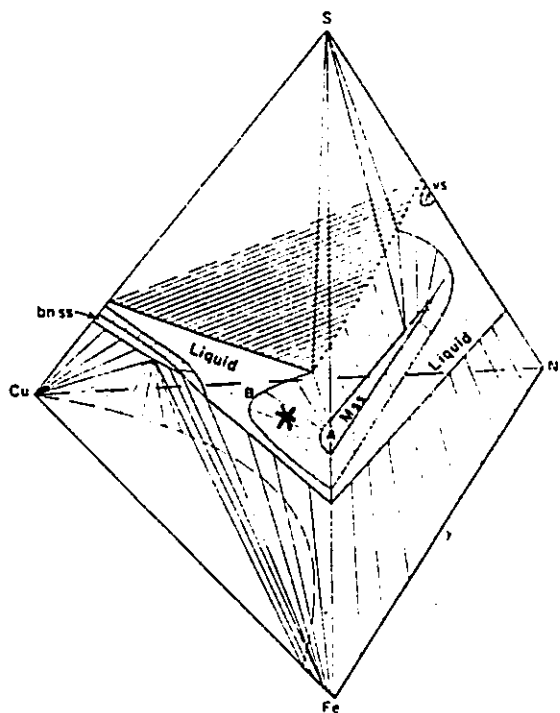
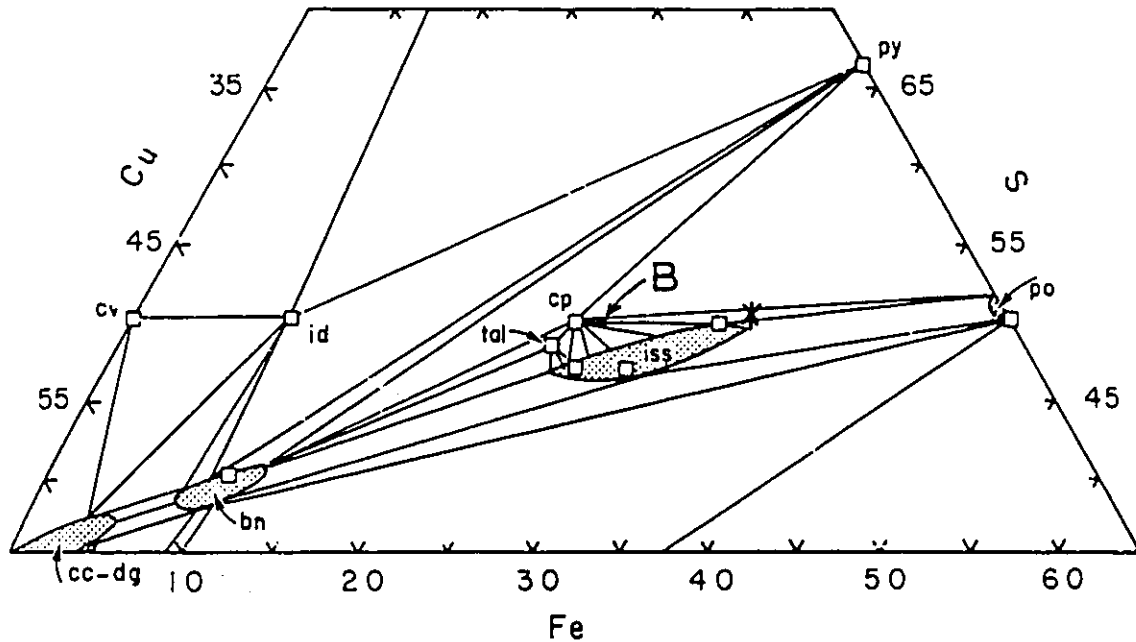


Fig. 4-2: Location of average calculated Two Duck Lake bulk sulfide composition (*) on (a) the Cu-Fe-Ni-S system at 1000°C (after Craig & Kullerud, 1969), and (b) Cu-Fe-S system at 300°C (after Craig & Scott, 1974). The Ni content in the calculated bulk sulfide liquid is low (0.3 mol %), consequently, the composition lies close to the Cu-Fe-S surface.

(a) ATOMIC % 1000°C



(b) ATOMIC % 300°C



- (1) Monosulfide solid solution (mss) starts to crystallize at temperatures between 1191 and 1100°C resulting in formation of Cu-rich liquid,
- (2) intermediate solid solution (iss) begins to crystallize at about 970°C and continues until the liquid is used up, presumably above 912°C,
- (3) prior to, and during iss formation it is likely that the Cu-rich sulfide liquid migrated locally, into such locales as plagioclase embayments,
- (4) subsolidus transformation of mss to pentlandite and pyrrhotite occurs at about 610°C,
- (5) subsolidus transformation of iss to chalcopyrite begins at about 557°C and to cubanite at about 200°C; the composition of iss is probably very close to that of chalcopyrite and therefore only minor cubanite is formed.

4-5 Distribution of ore-forming elements

The distribution of S, Cu, Ni, PGE and Au across the TDL gabbro shown in Figure 4-3 demonstrates two important features. Firstly, the trends for all metals are approximately parallel to that of S. This reflects the observed association between PGM and chalcopyrite. Secondly, the metal concentrations in the basal zone (samples F29 to F32) are considerably lower than those in samples of the main zone with similar S content.

Table 4-2: Sulfur, Ni, PGE, Au, Cu, Pb and Zn data for the Marathon deposit (TDL gabbro).

sample	rock type	S whole rock		Ni in		Ir	Rh	Pt	Pd	Au	Cu	Pb	Zn
		wt%	nickel	sulfides									
F1	tdl	0.02	117			0.09	1.5	20	1	3.7	239	7.8	68
F2	tdl	0.03	114			0.3	3.4	104	102	3.3	398	7.7	68
F3	tdl	1.96	325	214		1.46	34	611	1496	108	8897	11	83
F4	tdl	2.4	464	318		2.31	64	1235	3896	362	17172	13	83
F5	tdl	0.1	189	85		1	2.3	28	123	6.1	1297	11	64
F6	tdl	2.44	342	271		2.36	55	984	2410	213	13551	4	109
F7	tdl	1.03	240	149		1.25	27	435	869	112	5522	2	78
F8	tdl	2.76				1.59	52	638	3560	173	15173	8	103
F9	tdl	0.1	147	41		0.42	6.5	140	215	14	1092	4	69
F15	tdl	0.01	77			0.1	1.2	18	8	9.7	131	8.2	67
F18	tdl	1.35	211	105		0.78	10	317	372	102	4763	10	78
F19	tdl	0.13	110	21		0.32	2.5	32	47	3	392	7.4	91
F20	tdl	1.27	231	159		1.85	23	247	690	48	3674	5.8	88
F21	peg tdl	1.39	184	135		1.61	32	593	2410	162	7885	10	73
F22	peg tdl	0.9	162	129		0.83	14	246	627	61	3838	7.7	110
F23	peg tdl	0.32	141	88		0.5	7.4	107	184	15	1915	7.3	81
F24	peg tdl	0.14	73			0.08	0.9	9.4	1	2.3	718	6	86
F25	peg tdl	0.02	52			0.07	0.6	9.3	8	2.5	293	11	67
F26	peg tdl	0.15	70			0.15	0.7	17	1	13	472	7.8	85
F29	basal tdl	1.46	133	85		0.23	4	55	113	14	2476	2	101
F30	basal tdl	2.57	248	202		0.62	9.8	152	390	32	5323	17	110
F31	basal tdl	3.11	302	238		0.68	15	300	770	87	6948	13	119
F32	basal tdl	2.09	194	143		0.41	6.4	105	267	26	4805	15	125
F8c	tdl	2.8	406	340		1.89	40	942	1080	78	11800	13	131
F8p	peg tdl	3.17	458	399		2.26	52	620	4370	136	12600	10	152
F200d	tdl	1.97	298	262		2.43	41	714	1930	141	7600	4	131
F200w	gran tdl	0.87	45	33		0.16	3.7	91	276	9.8	3200	25	90
F12	x2	0.01	129			0.2	1.4	14	26	2.5	132	2	65
F13	x3	nd	132			na	3.7	nd	nd	2.8	36	3.4	50
F14	x4	nd	203			na	2.8	nd	nd	4.8	95	13	119
F16	x5	0.21	224			1.1	2.8	44	54	5.1	62	8.6	56
F17	x5	0.42	215			1	2.4	37	56	2.8	86	6	59
F27	x7	0.03	50			0.17	1.8	32	34	4.9	203	8.5	65
F34	x6	0.01	152			0.45	1	5	8	0.9	217	5.6	51
F35	x6	0.01	180			0.18	0.7	nd	10	0.16	97	2.4	56
F36	x4	0.01	365			0.66	1.3	13	18	0.9	151	3.8	54
F37	x1	0.01	147			0.35	1.1	14	13	1.6	165	5	52

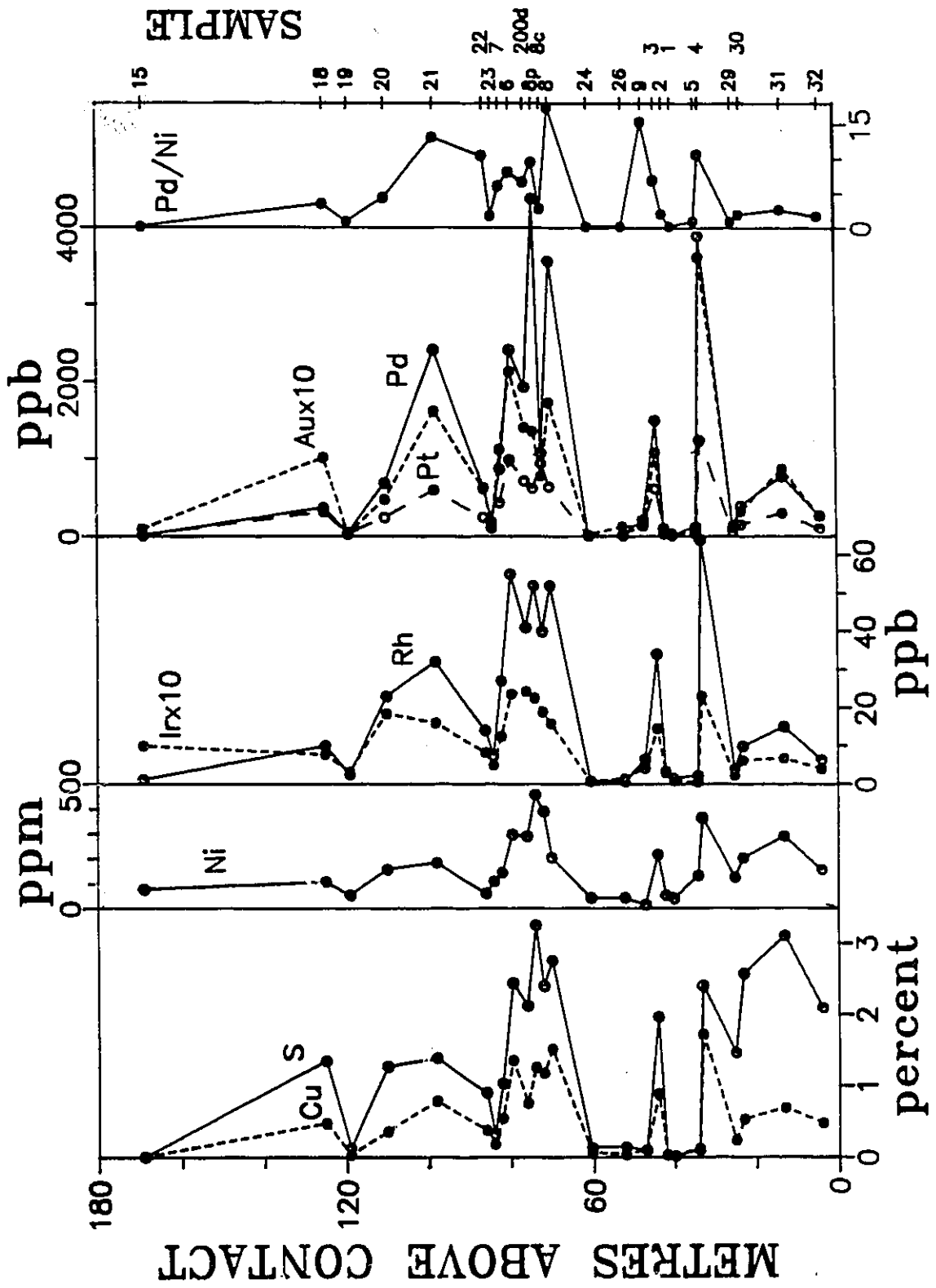
Mantle values (after Barnes et al. 1988)

2000	4.4	2.9	9.2	4.4	1.4	28
------	-----	-----	-----	-----	-----	----

Symbols: na, not analysed; nd, not detected; tdl, Two Duck Lake gabbro; peg, pegmatitic TDL gabbro; basal, basal sulfide zone; gran, granophyre; x2, xenolith type 2 (see text).

Note: Nickel, Cu, Pb and Zn in ppm; PGE and Au in ppb.

Fig. 4-3: Compositional variation of sulfur and chalcophile elements across the Two Duck Lake gabbro.



4-5-1 Sulfur-metal variation diagrams

Sulfur-metal variation diagrams are presented in Figure 4-4 a to g. The diagrams exhibit coincident increasing metal and sulfur concentrations consistent with control by sulfide minerals. The scatter is due in part to analytical uncertainty, and probable heterogeneous PGM distributions. The S-rich nature of the basal zone relative to the main zone is also evident.

The y-intercepts of the best fit lines, excluding the basal zone correspond to the concentration of metal in a sulfur-free rock. These "sulfur free" metal concentrations suggest whether sulfides are the only host minerals for the various metals. From these best fit trend lines it is inferred that sulfur-free rocks contain approximately 95 ppm Ni, 0.24 ppb Ir and negligible Rh, Pt, Pd, Au and Cu. Therefore, it appears that Ni and Ir are contained in minerals other than sulfides.

4-5-2 Distribution of Ni in various minerals

Nickel is contained in several minerals in the TDL gabbro besides sulfides. Probable Ni-bearing minerals include olivine, magnetite, clinopyroxene, and orthopyroxene (Kd values in Table 3-2). In the following, an estimate of the amount of Ni held by silicates and magnetite is determined.

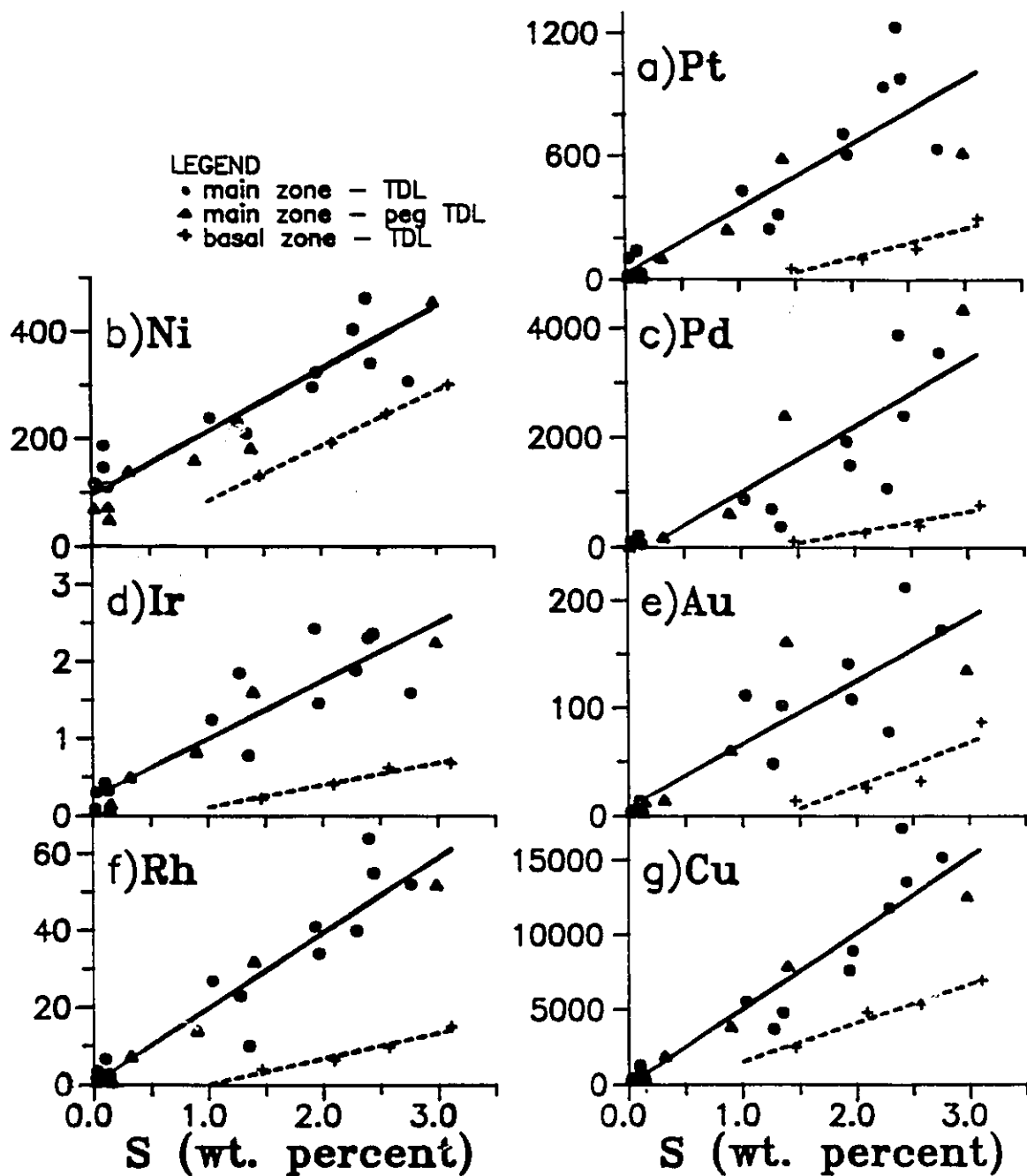


Fig. 4-4: Sulfur-metal variation diagrams for samples from the TDL gabbro. Symbols: main zone sulfide samples in coarse-grained gabbro, dots, and in pegmatitic gabbro, triangles; and, basal zone sulfides in coarse-grained gabbro, +.

The amount of Ni in olivine is calculated directly by multiplying the modal abundance of olivine by the abundance of Ni in olivine determined by electron microprobe (Table 2-1). The abundances of Ni in the pyroxenes and magnetite are determined indirectly because measured values are unavailable. The calculation involves application of distribution coefficients, average modal mineral abundances and the observed average Ni content of olivine. The calculations are done on a sample by sample basis and average values are listed in Table 4-3. It should be emphasized that since both the concentrations of Ni in olivine and the modal mineral abundance do not vary significantly across the TDL gabbro, calculated total Ni in sulfur-free rocks is approximately constant across the intrusion.

Table 4-3. Calculated Ni distribution in various minerals in TDL gabbro.

Mineral	D_{Ni} (min/melt)	Ni in mineral (ppm)	modal abundance (average%)	whole rock contribution (average ppm)
olivine	14	424	8.4	36
pyroxene	3.7	112	30	34
magnetite	14.7	445	4.4	20

The D values for pyroxene and magnetite are near minimum values published by Irving (1978). The D value for

pyroxene is a combined value for orthopyroxene (weight fraction or $X=0.25$; $D=2$) and clinopyroxene ($X=0.75$; $D=4.3$). The low value for magnetite is in agreement with experimental data by Fleet and MacRae (1988) for Ni-poor, Fe-rich charges.

The average total calculated concentration of Ni in magnetite and silicates in the TDL gabbro is 90 ppm. This value is close to 95 ppm, the estimate derived in Figure 4-4a, and therefore, the calculations are believed to be reliable.

4-5-3 Distribution of Ir in various minerals

Iridium is contained in minerals other than sulfides in the TDL gabbro. The average concentration of Ir in sulfur-free rocks, inferred from Figure 4-4b, is approximately 0.24 ppb. It is likely that this Ir is held in clinopyroxene and magnetite (references cited in section 1-6-2). Iridium concentrations have not been measured for individual minerals, but are probably very low (sub ppb level). It is believed that Ir was partitioned into these minerals from the silicate magma, and consequently, it is likely that relationships regarding its distribution will be similar to those for Ni. Therefore, the abundance of Ir in sulfur-free rocks is assumed to be constant across the TDL gabbro.

4-5-4 Silicate melt-sulfide liquid partitioning

Experimentally derived partition coefficients for the distribution of Ni, Ir and Cu between silicate melts and sulfide liquids are available (section 1-6-3A). Therefore, it is possible to test for equilibrium in the TDL gabbro by comparing measured Ni, Ir and Cu concentrations in the average bulk TDL sulfide liquid to that in the sulfur-free gabbro. This hypothesis is based on the assumption that the abundance of Ni, Ir and Cu in the sulfur-free gabbro corresponds to the amount in the silicate melt. This assumption is reasonable since it was determined in Chapters two and three (sections 2-2-5 and 3-3-4) that the TDL gabbro intruded as a crystal mush that solidified largely in-situ.

The amount of Ni and Ir in sulfur-free rocks is 95 ppm and 0.24 ppb, respectively. The average calculated concentrations of Ni and Ir in the TDL sulfides are 4320 ± 700 ppm and 29 ± 10 ppb, respectively (calculation of Ni and Ir in sulfides is made after whole rock concentrations are corrected for the amount in silicates and follows the procedure in section 4-5-5). Therefore, the observed partition coefficients are 45 and 121, respectively. These values are significantly lower than the range of values from 275 to about 900 for Ni and 3180 to 10^5 for Ir (references cited in section 1-6-3A). Therefore, the sulfide liquid was not in equilibrium with the silicate melt. Either the

amount of Ni and Ir in the silicate melt was too high, or the amount in the sulfide liquid was too low.

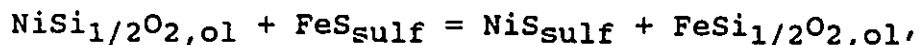
Unfortunately, the abundance of Cu in sulfur-free gabbro cannot be determined in a manner similar to that for Ni and Ir. The best fit line on the S versus Cu plot (Fig. 4-4g) intersects with a negative Cu value at $S=0$, however, due to scatter of data it is conceivable that up to 200 ppm Cu could be contained in the sulfur-free gabbro. Note that this value is greater than the upper limit of Cu concentrations in sulfur-free Keweenawan flood basalts (150 ppm Cu, BVSP 1982), and chilled margin samples of Nipissing diabase (114 ppm Cu, Lightfoot et al. 1987). The average calculated abundance of Cu in the sulfide melt is 17.4 ± 4.1 wt.% Cu. Three samples yielded between 20 and 25 wt.% Cu. Only samples with greater than 0.5 wt.% S ($n=14$) were used to calculate average copper in sulfide melt to minimize the propagation of analytical uncertainty. Sulfides with 17.4 wt.% Cu would be in equilibrium with a silicate melt containing 696 ppm Cu using a partition coefficient of 250 (Naldrett 1989) or 126 ppm using a partition coefficient of 1380 (after Peach et al. 1990). It is notable that Peach et al. (1990) showed $K_D(\text{Cu})$ varies with the fraction of FeS in sulfide melt and that the value 1380 corresponds to sulfide melts with high Ni and Cu concentrations; consequently, a lower K_D value is probably more applicable to the TDL

sulfides. Therefore, applying lower D values, for instance 600 to 250, implies that the TDL silicate melt contained between 290 and 696 ppm Cu. This range of Cu concentrations is higher than what is believed to be reasonable in basaltic magmas. It follows that either the sulfide liquid was not at equilibrium with the silicate melt and the sulfide liquid contains too much Cu, or the two were at equilibrium and the silicate melt was very Cu-rich.

Therefore, the concentrations of Ni and Ir is too low, and Cu possibly too high, in the TDL sulfide liquid to have been in equilibrium with the TDL silicate melt. Alternatively, the silicate melt/sulfide liquid partition coefficients are not applicable because a water-rich fluid was involved at some stage. This latter possibility is discussed more fully in section 4-5-8 and is rejected.

4-5-5 sulfide liquid-olivine disequilibrium (K_{D3})

If an immiscible sulfide liquid was in equilibrium with olivine then Ni and Fe are partitioned between the two phases according to the exchange reaction:



for which the distribution coefficient (K_{D3}) is given by:

$$K_{D3} = (\text{Ni/Fe})_{\text{sulfide melt}} * (\text{Fe/Ni})_{\text{olivine}}$$

where concentrations are molecular fractions.

K_{D3} values are calculated for 7 samples of TDL gabbro (Table 4-4). The Fe and Ni concentrations in olivine are determined by microprobe (Table 2-1a). The FeS in sulfide liquid is calculated by the following procedure:

- 1) subtract Ni in olivine, clinopyroxene and magnetite from whole rock concentrations,
- 2) convert remaining Ni to moles of pentlandite using appropriate formula; in this case atomic fractions 26.5 % Fe, 26.5 % Ni, and 47 % S are used (uncertainty discussed below),
- 3) convert Cu to moles of chalcopyrite (assuming stoichiometric proportions),
- 4) convert the remaining moles of S to stoichiometric pyrrhotite (FeS), and
- 5) the amount of FeS in the sulfide melt is the sum of FeS used in chalcopyrite, pentlandite and pyrrhotite.

Table 4-4. Compositional data in mole percent for bulk sulfide liquid and olivine, and calculated K_{D3} values.

sample	olivine		sulfide		K_{D3}
	Fe	Ni	FeS	NiS	
F3	45.74	.078	76.55	.595	4.57
F4	45.21	.093	63.26	.723	5.56
F6	40.11	.065	71.43	.606	5.20
F7	43.34	.075	72.23	.789	6.34
F18	44.14	.062	81.80	.423	3.70
F29	46.91	.023	91.12	.330	7.32
F31	49.26	.046	88.31	.436	5.24

There are two principal sources of error in the determination of K_{D3} . By far the greatest error is that due to the estimation of Ni in the sulfide melt. For example, a 50% error in estimating Ni concentrations in magnetite and silicates corresponds to a 25 % variation of K_{D3} .

The second source of error is analytical uncertainty. The error for Ni concentrations in olivine (probe data) is significant at concentrations near the detection limit. For example, a 33% error on 300 ppm NiO corresponds to a 17% variation of K_{D3} . The error for XRF data is minimized by selecting samples with greater than 1 wt. % S (2.8 wt.% sulphides). The error in this case is believed to be less than 5%.

Negligible error is introduced by the selection of sulfide mineral compositions. Chalcopyrite exhibits minimal solid solution, and the range for pyrrhotite solid solution composition is relatively small. Pentlandite compositions are more variable, but the abundance of pentlandite is much less than that of chalcopyrite and pyrrhotite, therefore, varying the composition of pentlandite does not significantly affect the total amount of FeS.

Result of K_{D3} calculation: The average K_{D3} for TDL gabbro is 5.42 ± 1.17 . This value is near the lower limit of the range (5-15) found in the majority of NiS deposits as

summarized in Table 3.2 of Naldrett (1989). Similar K_{D3} values were determined for the Water Hen intrusion, Duluth Complex (5.9) (Mainwaring and Naldrett 1977) and the Great Lakes Nickel deposit, Crystal Lake gabbro (8.2) (Fleet and MacRae 1983). These comparisons are relevant because the latter intrusions, like those in the Port Coldwell alkalic complex, are related to the Keweenaw Rift.

The K_{D3} value of most natural data is significantly lower than experimental values. Experimentally determined values for runs conducted under various conditions that approximate magmatic settings by Clark and Naldrett (1972), Fleet et al. (1977) and Fleet and MacRae (1983; 1987 and 1988) do not fluctuate significantly from values of 30 to 35. The effect that Cu might have on K_{D3} is not known, but Fleet & Stone (1990) maintain that low and moderate amounts of Cu in the sulfide liquid will not affect K_{D3} . The low K_{D3} value for the TDL gabbro implies disequilibrium between sulfide liquid and silicate melt. That is, either olivine contains too much Ni, or the sulfide melt contains too little Ni.

4-5-6 Mantle normalized PGE, Ni, Cu and Au

Normalized Ni, Cu, PGE and Au data are presented diagrammatically in two ways. The first is as mantle

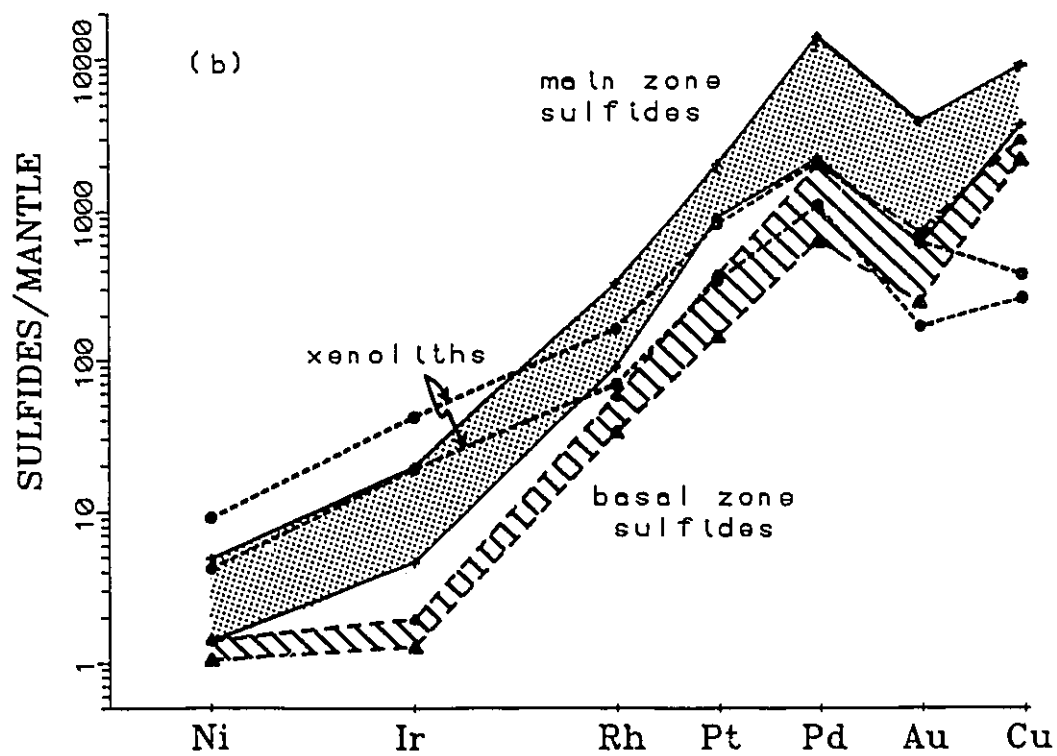
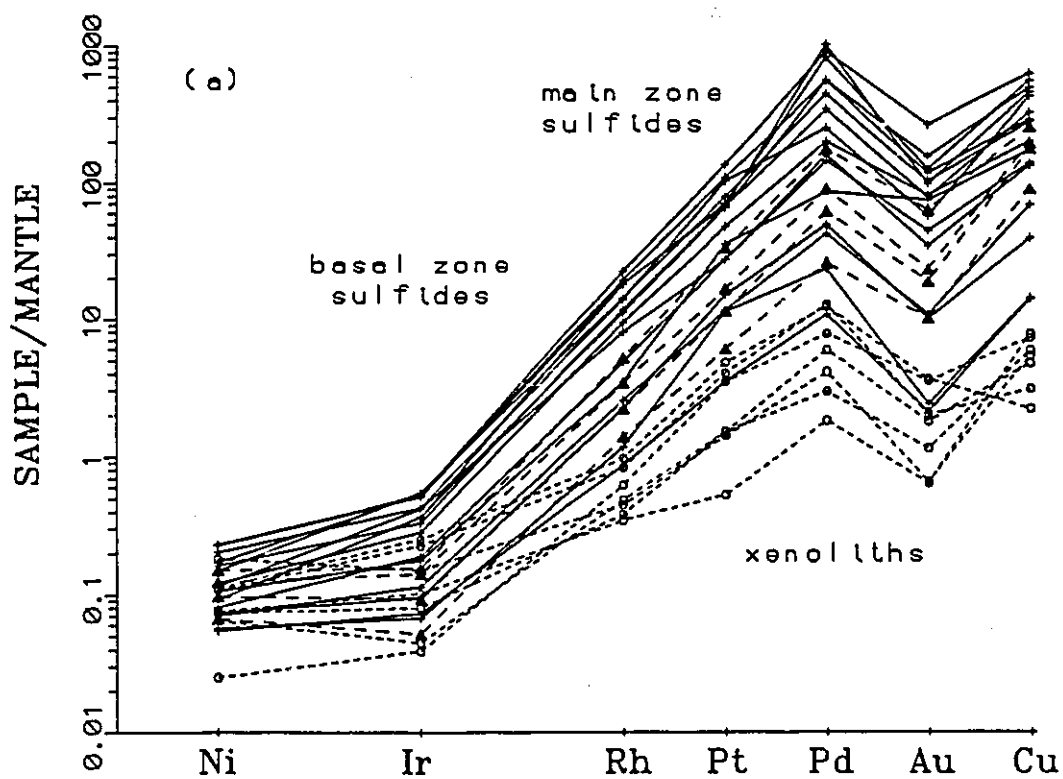
normalized (Barnes et al., 1988) whole rock ratios. The second is concentration in 100 percent sulfides, calculated by assuming the ideal composition of the sulfides, divided by mantle abundances. A difference between the two diagrams is that uncorrected whole rock Ni values are used in the former and estimated Ni values for the sulfide component (i.e., total Ni minus silicate/oxide Ni, see section 4-5-2) in the latter.

The metal composition of xenoliths, and the basal and main zones of the TDL gabbro, are compared in Figure 4-5a. Their calculated sulfide compositions are compared in Figure 4-5b. There are two important features exhibited by these diagrams. Firstly, (Fig. 4-5a) it is evident that samples from the TDL gabbro have more fractionated compositions (steeper patterns) than the xenoliths. Secondly, (Fig. 4-5b) basal zone sulfides contain slightly less Ni and Cu and significantly less PGE than main zone sulfides.

4-5-7 Pd-metal fractionation

There is a good power curve fit between Pd and the other metals as shown in Figures 4-6a through f. The Pd vs Ni curve is based on estimated Ni values for the sulfide component (section 4-5-2). A similar correction for Ir is

Fig. 4-5: (a) Mantle normalized Cu, Ni, PGE, and Au concentrations from Eastern gabbro xenoliths, and the main and basal sulfide zones in the TDL gabbro, and (b) the range of mantle normalized concentrations in sulfides for the samples plotted in (a).



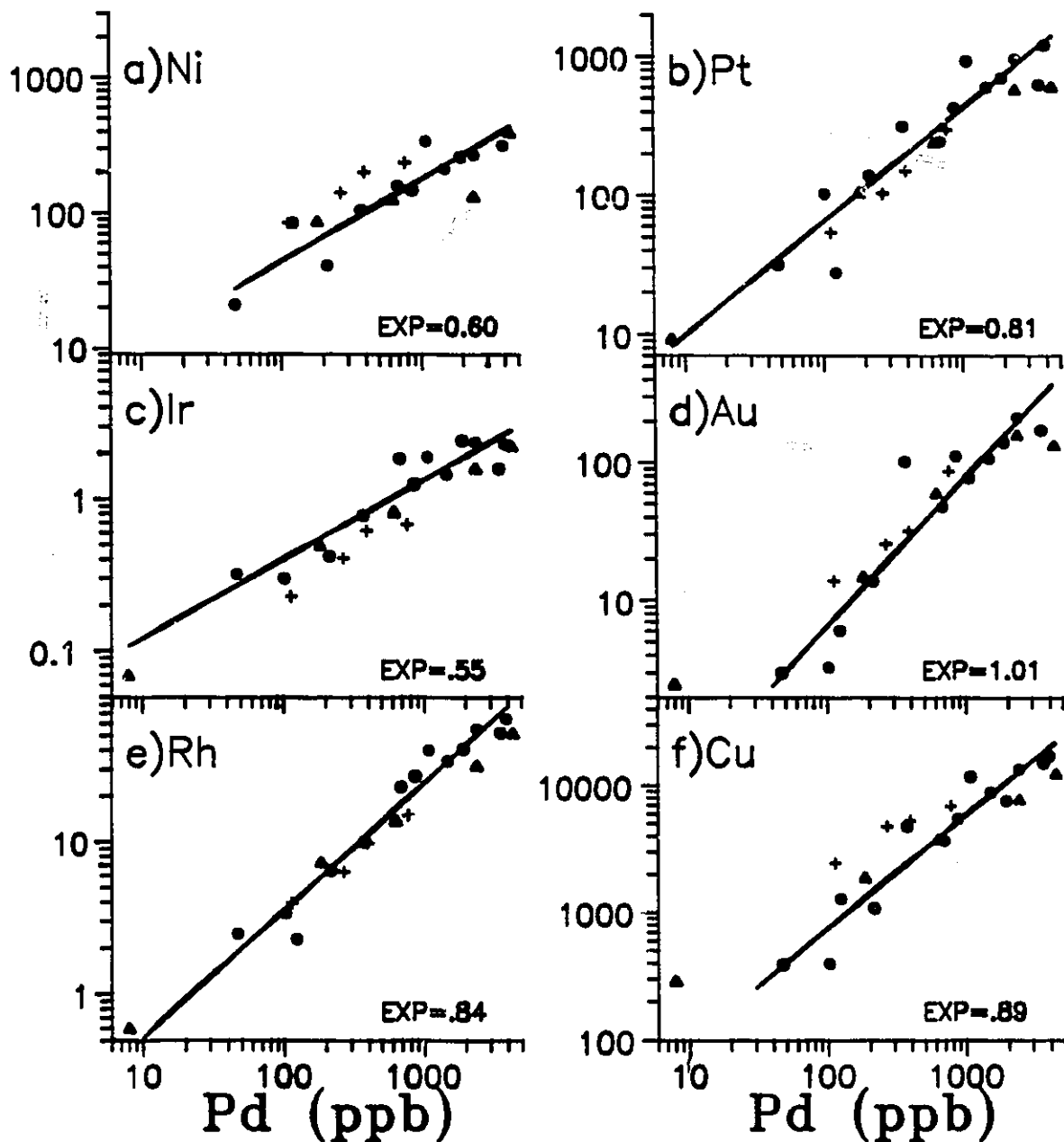


Fig. 4-6: Palladium-metal variation diagrams for samples from the TDL gabbro. Best fit lines are power curves, and exponential values are indicated. Symbols: main zone sulfide samples in coarse-grained gabbro, dots, and in pegmatitic gabbro, triangles; and, basal zone sulfides in coarse-grained gabbro, +.

not made. The exponential equations for the curves are of the form:

$$y = Pd^n * b$$

where y is metal (Ni, Ir, etc.) concentration, n is an exponent to which Pd (x value) is raised, and b is the y value (intercept) at Pd equals 1. If the exponential value is 1, as it is for Pd vs Au, then the curve is linear.

The exponential Pd-metal relationships indicate that Ni, Cu, PGE and Au do not behave coherently, i.e., some phase fractionates the metals. The exponents, listed in increasing order, are Ni=Ir<Rh=Pt<Cu<Au. This order is interpreted as representing a sequence in which the geochemical behaviour of the elements becomes increasingly like that of Pd. In other words, Ni is least like Pd and Au is most similar to Pd.

The variation of Pd/Ir correlates with that for Cu/Ni (Fig. 4-7), and therefore, the fractionation of Ni, Cu and PGE are probably simultaneous processes.

A final observation from Figure 4-6 is that sulfides in the basal zone (+ symbols) appear to be enriched in Ni and Cu relative to the PGE.

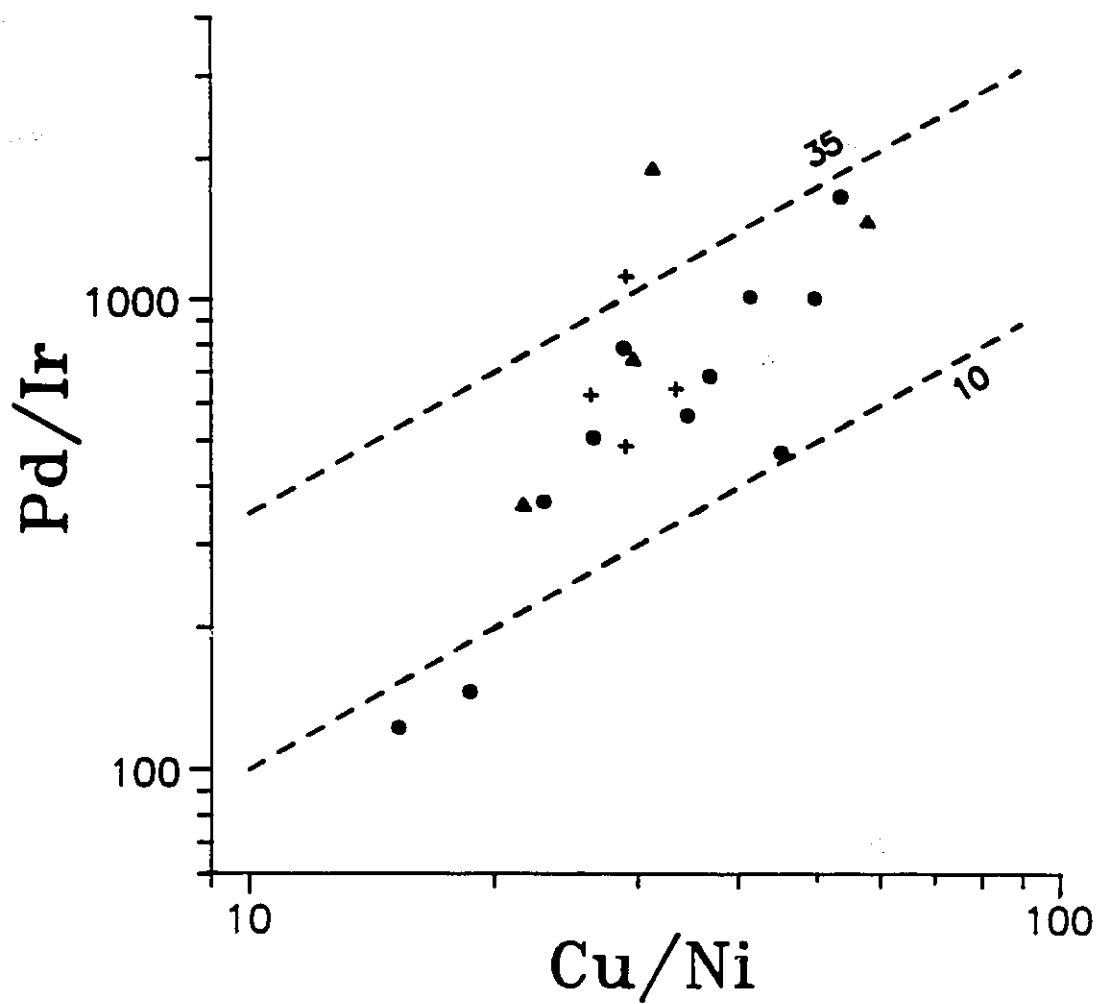


Fig. 4-7: Pd/Ir versus Cu/Ni variation diagram for samples from the TDL gabbro. Symbols: main zone sulfide samples in coarse-grained gabbro, dots, and in pegmatitic gabbro, triangles; and, basal zone sulfides in coarse-grained gabbro, +.

4-5-8 Possible mechanisms for Cu, Ni and PGE fractionation

The following sections compare observed fractionation trends and petrography in the TDL sulfides to possible mechanisms for metal fractionation.

A - Refinement of primary sulfides by interaction with hydrous fluids at low temperature: From evidence presented in a series of abstracts (Watkinson et al. 1986, Dahl et al. 1987, Ohnenstetter et al. 1989), Ohnenstetter & Watkinson (1991) inferred that the genesis of PGM in the TDL gabbro is consistent with refinement of primary sulfides by interaction with hydrous fluids at low temperatures. The evidence cited includes the strong zonation of PGM, and the association of PGM-bearing sulfides, predominantly chalcopyrite, with (a) pegmatite, (b) Cl-rich hydrous silicates (biotite and amphibole), and (c) Cl-bearing fluorapatite.

However, although this mechanism can account for the described microscopic features, it cannot account for larger scale features described in this study. For instance, it appears that Cu, Ni, Au and PGE fractionation occurred simultaneously, and if the hypothesized low temperature refinement of primary sulfides plays a major role in the genesis of the sulfide deposit then this process must include the migration of chalcopyrite. It follows that the

migration of chalcopyrite in hydrous fluids would result in the formation of chalcopyrite veins, but such veins have not been found. Further, there is no geochemical evidence for the existence of pervasive fluid-rock reactions, presumably necessary for large scale mobilization of sulfides. Therefore, although there is evidence for refinement of sulfides by hydrous fluids at low temperature, this mechanism probably did not play an important role in ore formation.

B - Sulfide liquid-silicate melt partitioning: This seems unlikely because the partition coefficients for Cu and Ni are much less than those for PGE, and that for Pd is equal to that for Ir. This order of fractionation is inconsistent with the observations.

C - Sulfide liquid-Fe alloy partitioning: The fractionation of metals in a sulfide liquid could conceivably occur by equilibration with other minerals, such as Fe-alloys. However, it is unlikely that this occurred in the TDL sulfides because the partitioning of Os, Ir and Pt into Fe-alloys from a sulfide melt is much stronger than for Pd and Ni (Fleet & Stone 1991).

D - Sulfide liquid-monosulfide solid solution partitioning:
It is possible for fractionation of a sulfide liquid by fractional crystallization of monosulfide solid solution (mss). Mss is believed to preferentially include Ni and Ir over Cu, Pd and Pt (Naldrett et al. 1982). This mechanism has been used to account for the compositionally zoned sulfide deposits at Sudbury (Hawley 1966, Keays and Crocket 1970; Cabri and Laflamme 1976; Naldrett et al. 1982) and at the Alexo mine, Ontario (Barnes and Naldrett 1986).

Despite the attractiveness of this mechanism to explain Ni and Ir fractionation from the rest of the metals in the TDL sulfides, it is unlikely to have been an important process for the following reasons. Firstly, experimental study of sulfide liquid-troilite (stoichiometric pyrrhotite) partitioning at 1000°C by Fleet & Stone (1991) determined that Ni ($D=.3$), and perhaps Ir ($D<1$), favoured the liquid, and that the behaviour of Ni was similar to that of Rh. This is not the observed order of fractionation for the TDL sulfides. Although this experiment was determined for Cu-free melts, the low Ni content of the troilite is analogous to the mss envisaged to have crystallized from the Ni-poor TDL sulfide liquid. Secondly, chalcopyrite/pyrrhotite mineral zonation at the hand sample (or larger) scale is absent in the TDL gabbro.

Therefore, the TDL sulfides probably did not lose Ni and Ir during fractional crystallization of mss.

4-5-9 Summary

The following is a summary of the above features:

- a) there are three petrographically and compositionally distinct types of sulfide mineralization (basal and main zones in the TDL gabbro, and xenolith-hosted sulfides),
- b) an interstitial, Cu-rich sulfide liquid appears to have been present in the TDL gabbro from a time at least as early as the intrusion of the TDL magma,
- c) the sulfide liquid becomes Cu-rich during crystallization of pyrrhotite,
- d) the Cu-rich sulfide liquid was apparently mobile,
- e) the bulk sulfide liquid was not at equilibrium with the host gabbro, and
- f) metals in the sulfides are fractionated by some phase; the ascending order in which the geochemical behaviour of the metals becomes increasingly like that of Pd is Ni=Ir<<Rh=Pt<Cu<Au.

4-5-10 Problems

There are two prominent characteristics of the TDL sulfides that are inconsistent with experimental studies of sulfide liquid-silicate melt or sulfide liquid-mineral

partitioning. Firstly, the bulk TDL sulfide melt was not at equilibrium with the TDL gabbro (Ni and Ir in the sulfides are too low, and Cu is possibly too high). Secondly, there is no known phase that could have coexisted with a supposed TDL sulfide melt to account for the metal fractionation. These inconsistencies indicate that an origin of bulk immiscible sulfide liquid segregation from a silicate melt is unlikely. Any proposed model for the genesis of sulfide mineralization in the TDL gabbro must therefore account for these features.

4-6 Petrography of sulfides in the MacRae occurrence

Sulfides at the MacRae occurrence consist of chalcopyrite, minor bornite and trace pyrite, galena and sphalerite. They occur in both the Geordie Lake (GL) gabbro and neighbouring quartz monzonite. The sulfides are subdivided into four principal types based on texture and setting. The first is ubiquitous, micron sized anhedral grains included predominantly within albite rims. These sulfides exist throughout the GL gabbro and generate a whole-rock S content of approximately 0.01-.02 wt percent.

The second, and most important type of sulfides with respect to PGE concentration, is disseminated aggregates of chalcopyrite grains that are intergrown with secondary amphibole (actinolite, Mulja & Mitchell 1991). The

actinolite/chalcopyrite aggregates vary in size from millimetres to centimetres, and occur interstitial to the major silicates or along micro-fractures within magnetite, clinopyroxene or plagioclase. Chalcopyrite is also intergrown with secondary amphibole rims on clinopyroxene (Fig. 4-8c and d). There is a spatial relationship between these sulfides and albite rims (Fig. 2-22), albite microdikelets (Fig. 2-20) and albite pods (Fig. 4-8a and b).

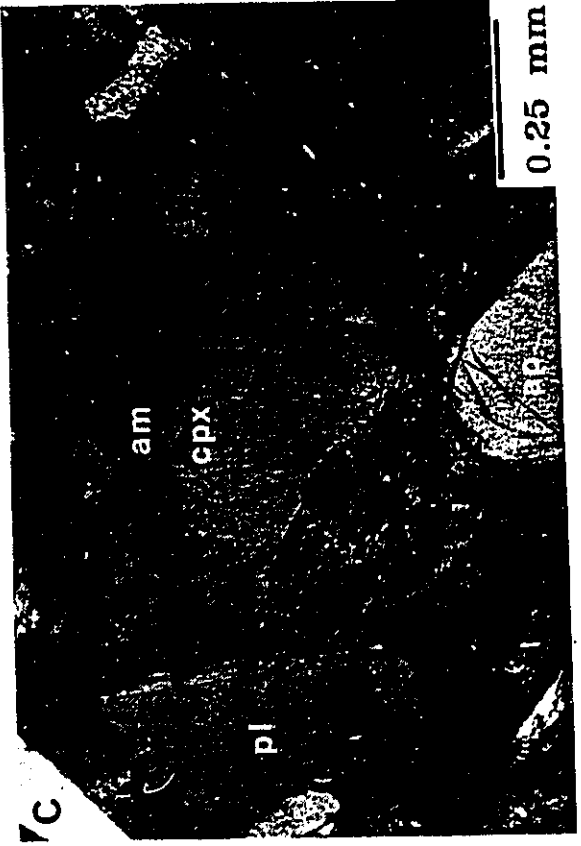
The third type of sulfide is massive chalcopyrite stringers within the GL gabbro and quartz monzonite (types 3a and 3b, respectively), located close to the gabbro-quartz monzonite contact. The stringers are up to a few centimetres thick and discontinuous. These sulfides contain melonite, hessite and altaite, but not appreciable PGM (Mulja 1989). Within quartz monzonite, away from the contact, sulfides occur in micro-veinlets of actinolite, chalcopyrite and trace pyrite, galena and sphalerite.

A fourth and relatively uncommon type of sulfides in the GL gabbro are blocky, interstitial chalcopyrite grains, less than 1 mm in size, and are typically in contact with unaltered plagioclase and clinopyroxene. According to Mulja (1989) they are not associated with PGM. These sulfides (samples G60 to G63) generate a whole-rock S content of approximately 0.05 wt.%.

Fig. 4-8: Photomicrographs of common type 2 sulfide-silicate relationships in albite pods and GL gabbro. Photomicrographs A and B are of the same location, but A is in transmitted light, and B reflected light. Similarly, C and D are in transmitted and reflected light, respectively.

A. and B. Subhedral laths of cloudy albite (grey to white) from albite pod sample G49 (also shown in Fig. 2-22C). Interstitial minerals are amphibole (dark) and chalcopyrite (opaque in A and white in B).

C. and D. Subhedral clinopyroxene crystal partly altered (approximately 60%) to actinolite. The original clinopyroxene crystal outline is in contact with the plagioclase crystal at the centre left. Chalcopyrite (white) in D is intergrown with amphibole in the altered clinopyroxene margin, and in interstitial positions (e.g., lower left).



4-7 Distribution of ore-forming elements in the MacRae occurrence

4-7-1 Unmineralized zone (background values)

The average abundance of metals in sulfide types 1 and 4 are listed in Table 4-5. They are considered to be background values. The variation of metal concentrations (1 sigma values) is small and suggests that these 'unmineralized' samples have relatively constant compositions. The abundance of Rh, Pd, Au and Cu are essentially the same in each type, but the average Ni is slightly higher and Ir slightly lower in type 4 sulfides. Despite the similarities in metal concentrations, average sulfur content of type 4 samples (0.055 wt%) is roughly 3 times that of type 1 samples. Therefore, type 4 sulfides are considered to be unimportant with respect to PGE mineralization and will not be considered further.

4-7-2 Mineralized zone

The distribution of S, Cu, Ni, Pb, Zn and PGE across a section through the mineralized zone of the GL gabbro and neighbouring quartz monzonite is shown in Figure 4-9. The sulfide type (1 to 4) is indicated at the right side of the figure, except for quartz monzonite. All samples in quartz monzonite contain type 3b sulfides. Note that the trend for

Fig. 4-9: Compositional variation of sulfur and chalcophile elements across the mineralized zone in Geordie Lake gabbro and neighbouring quartz monzonite. The sulfide type of each sample is indicated at the right (e.g., 52-2 is type 2 sulfides in sample G52). No suffix for samples of gabbro correspond to sulfide types 1 or 4, and all quartz monzonite samples contain type 3b.

Table 4-5: Nickel, PGE, Au, Cu, S, Pb, and Zn data for the MacRae Occurrence (GL gabbro).

157

sample	sulfide type	Ni	Ir	Rh	Pd	Au	Cu	S	Pb	Zn
ave.	G1 to G18	24.1	0.10	0.73	31.7	2.94	241	0.01	12	185
1 sigma	n=18	10.1	0.07	0.33	19.7	2.05	75		2.2	25
ave.	type 1 S<.02 wt.% in min. zone	56	0.0375	1.57	38	4.53	252	0.014	10.9	152
1 sigma	n=22	30	0.0229	0.98	19	5.1	121		3.6	21
ave	type 4 G60 to 63	38	0.018	0.965	24	2.6	226	0.055	10.6	157
1 sigma	n=4	4.5	0.96	0.14	9.1	1.3	67	0.01	2.3	11
G27	type 2 gab	67	0.01	3.6	227	11	1657	0.04	16	130
G29	gab	70	0.03	3.5	160	5.5	2062	0.11	6	161
G40	gab	83	0.05	3.5	258	5.4	3099	0.35	18	360
G41	gab	114	0.05	9.1	796	59	7437	0.61	14	177
G49A	gab	69	0.04	6.4	163	3.3	250	0.02	13	122
G52	gab	56	0.05	2	270	26	6072	0.61	15	151
G53	gab	102	nd	4	379	65	11408	1.85	9.4	206
G54	gab	56	nd	1.5	63	2.4	561	0.05	11	150
G55	gab	109	nd	6.2	271	9.2	2627	0.36	15	188
G65	gab	99	0.01	2.3	187	nd	2684	0.23	11	166
G67	gab	94	0.01	2.3	125	2.8	436	0.03	13	162
G78	gab	72	0.06	4.3	140	8.6	1047	0.11	16	178
G84	gab	159	0.11	27	1680	83	9783	1.49	17	178
G49	alb. pod	48	nd	4.7	166	111	6165	0.53	38	222
G68	type 3a	122	0.14	6.8	1140	231	12843	2.28	12	508
G24	type 3b syen	94	0.08	13	303	14	6356	0.63	14	447
G30	syen	12	0.02	0.4	29	11	443	0.01	24	244
G32	syen	3	0.09	nd	9.8	0.64	308	0.01	28	405
G33	syen	6	0.08	0.16	nd	1.1	762	0.03	70	387
G34	syen	4	0.07	nd	nd	0.24	132	0.02	23	388
G69	syen	172	0.07	11	280	188	16368	2.14	21	708
G71	syen	175	nd	8.2	283	27	8014	1.29	14	476
G72	syen	144	0.02	2.2	279	5.7	7450	0.65	35	355
G73	syen	27	0.1	0.15	389	27	6934	0.5	76	957
G74	syen	79	0.02	0.11	461	62	15733	2.06	71	568
G75	syen	107	nd	0.33	362	246	38396	6.02	31	101
mantle		2000	4.4	2.9	4.4	1.4	28			

note: Ni, Cu, Pb and Zn data in ppm, S in wt %, and PGE and Au in ppb.

Cu is almost parallel to that for S and reflects chalcopyrite as the major sulfide phase.

Despite the similarities in Cu contents, there are several compositional differences between sulfide types 2 and 3 distinguished in Figure 4-9. The following features are exhibited by type 2 sulfides:

- (a) spikes for Pd, Au (and Rh?) concentrations coincide with maxima for sulfur,
- (b) Ni and Ir are erratic and do not coincide with S, and
- (c) Zn and Pb are approximately constant.

The above observations contrast sharply with the following for type 3 sulfides:

- (a) the amount of Rh and Pd in the sulfides decreases rapidly away from the contact, whereas Au coincides with S,
- (b) the highest Ir concentrations occur at the contact, but decreases rapidly into the quartz monzonite, whereas Ni coincides with S, and
- (c) Zn and Pb concentrations are above background and coincide with S.

4-7-3 Distribution of Ni and Ir

The Ir concentrations in mineralized and unmineralized gabbro are equivalent; therefore, Ir is not associated with sulfides, except for type 3 near the contact. The small enrichments of Ni above background in

mineralized samples is likely due to minor phases such as melonite (NiTe) (Mulja 1989).

It is proposed that most of the Ni and Ir in the GL gabbro are contained by silicates and magnetite, and are fractionated from the interstitial melt as the melt migrates through the crystal pile (Chapter three). This is consistent with the rapid decrease in Ni concentrations from samples G18 to G1 in Figure 3-7. Comparison of Ni and Ir concentrations in the GL gabbro to those of the TDL gabbro are also consistent with significant fractionation between residual melt and GL gabbro minerals. The average Ni content (microprobe analysis) of three olivine grains in a single sample of GL gabbro from the mineralized zone (G58) is 400 ppm, a value within the range determined for the TDL gabbro. Therefore, the initial Ni concentration in the GL magma was approximately equal to that in the TDL magma, yet the average concentrations of Ni (24 ppm) in the unmineralized zone (G1 to G18 in Table 4-5) is less than the amount in sulfur-free TDL gabbro (95 ppm). Similarly, the concentrations of Ir are 0.1 and 0.24 ppb, respectively. These different values are best accounted for by fractional crystallization.

4-7-4 Distribution of Cu and Pd

The average Cu concentration of 240 ± 75 ppm (Table 4-5) in the unmineralized zone is generated by Cu contained in both chalcopyrite and silicates. Based on the amount of sulfur in samples G1 to G18 (0.01 wt %) the amount of Cu in chalcopyrite is approximately 100 ppm. Therefore, the amount in silicates is on the order of 140 ppm. As discussed for the TDL gabbro, 140 ppm is at the upper limit of Cu concentrations in basaltic rocks. Since the trend of increasing Cu in Figure 3-7 implies that Cu is incompatible, then it is reasonable to propose that the composition of Cu in the residual melt is much higher than 140 ppm. That is, as interstitial melt migrates through the crystal pile it is becoming enriched in Cu beyond that which is normal for basaltic magmas.

The amount of Pd in unmineralized samples (32 ± 20 ppb) is enriched relative to that in basaltic rocks. For example, the amount of Pd in the continental tholeiites of the Karroo and Deccan flood basalt provinces is on the order of 8 to 11 ppb (Crocket 1981; Barnes 1983). Therefore, if Pd behaves like Cu interstitial melt is becoming enriched in Pd during migration through the crystal pile.

4-7-5 Mantle normalized PGE, Ni, Cu and Au

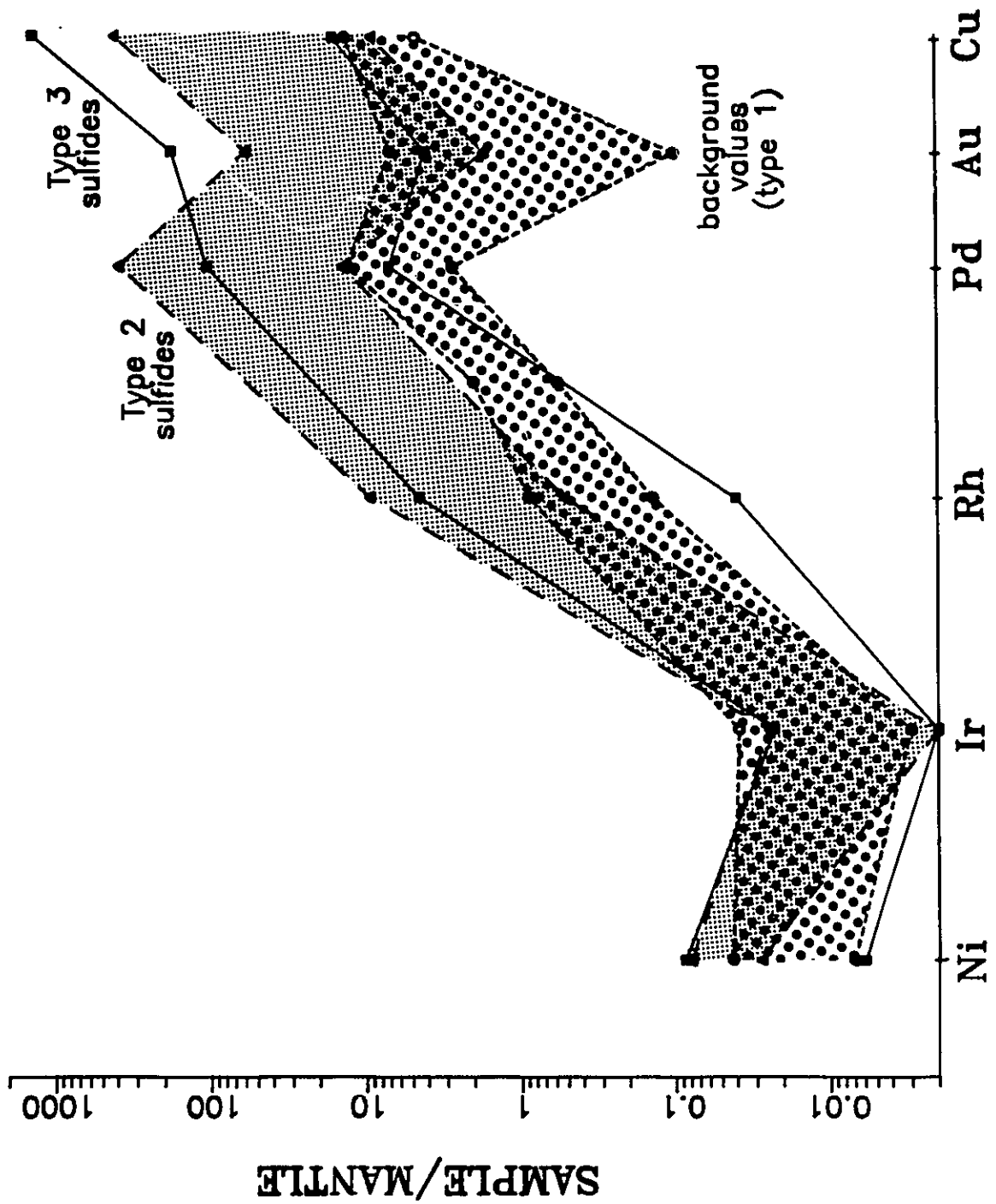
The range of mantle normalized Ni, Ir, Rh, Pd, Au and Cu concentrations in sulfide types 2 and 3 are compared to background values in Figure 4-10. It is evident that Pd, Au and Cu concentrations, and to a lesser extent Ni and Rh, are enriched in the sulfide samples, whereas Ir is not greater than background. The concentrations of Cu and Au relative to Pd and Rh are greater in type 3 sulfides than in type 2 sulfides.

4-8 Discussion

A model for the genesis of sulfides in the GL gabbro and neighbouring quartz monzonite must account for the following observations:

- 1) sulfide assemblages do not contain pyrrhotite,
- 2) the occurrence of three prominent types (1, 2 and 3) of sulfide mineralization; type 1 sulfides are ubiquitous in the GL gabbro and generate background values; type 2 sulfides are disseminated and occur in broad discontinuous zones within the GL gabbro; and, type 3 sulfides occur either at the contact or within the quartz monzonite,
- 3) the association between sulfides (chalcopyrite, bornite, pyrite, galena and sphalerite) and secondary amphibole,
- 4) the spatial association between sulfides and albite rims, microdikelets and pods,

Fig. 4-10: Range of mantle normalized Cu, Ni, PGE and Au concentrations in MacRae occurrence sulfide types 1 (background); 2 (disseminated sulfides in the Geordie Lake gabbro); and, 3 (stringer sulfides in quartz monzonite and GL gabbro at the contact).



5) the strong fractionation of Cu, Pd and Au and somewhat lesser Rh and Ni fractionation relative to Ir in the mineralized samples.

The above features of sulfide mineralization are consistent with a deuteric hydrothermal origin. That is, normal crystallization of anhydrous phases (plagioclase, etc.) from an evolved silicate melt led to a volatile (H₂O, Cl, etc.)-rich residual fluid. Equilibration of volatiles with evolved melt and nearby crystals resulted in the removal of alkali metals, S, Fe, Cu, Pd and Au, and lesser amounts of Ni and Rh to the hydrous fluid. The fluid migrated through the crystal pile along grain interfaces. Deposition of type 2 sulfides coincided with local hydrothermal alteration of primary minerals and the deposition of interstitial actinolite. This hypothesis is consistent with abundant evidence for the existence of evolved interstitial melt in the mineralized zone. Indeed, the albite pods exhibit evidence for the separation of a vapour phase (see section 3-4-5D).

The enriched Cu and Pd concentrations of the unmineralized gabbro (type 1 sulfides) probably represent trapped components introduced by the interstitial melt which invaded the cumulate pile. A late, presumably lower temperature mineralizing event resulted in the formation of type 3 sulfides.

Chapter 5 - Discussion and Conclusions

5-1 Genesis of the Two Duck Lake gabbro (Marathon deposit)

The Two Duck Lake intrusion is subdivided into a lower and upper zone. Sulfide mineralization occurs only in the lower zone, referred to as the TDL gabbro. The TDL gabbro was emplaced as a crystal mush consisting of silicate melt, plagioclase and olivine crystals, and immiscible sulfide liquid and there was little, if any, crystal-free magma in the chamber. The plagioclase and olivine crystals formed a framework for crystallization of the interstitial melt. In order of first appearance the crystallization sequence is plagioclase, olivine, clinopyroxene, orthopyroxene, magnetite, and finally, orthoclase and quartz. Apatite crystallized prior to orthoclase and quartz, and affected the composition of residual melt. Locally high concentrations of H₂O in the TDL magma interrupted the crystallization sequence and resulted in the growth of hydrous minerals, e.g., biotite and amphibole. Minor settling of plagioclase occurred to form rare modal layering. The trace-element concentrations and major mineral compositions of TDL pegmatitic gabbro are equivalent to those of coarse-grained TDL gabbro, so that pegmatite does not represent fractionated TDL magma. There are two types of granophyre: contact-related and pegmatite-

associated. The first type is 'dry' partial melt derived from country rock. It was intruded at the base of the TDL gabbro and locally affected crystallization of the TDL magma. The second type is 'wet' silicate magma derived by the accumulation of migrating interstitial melt. The liquid that crystallized pegmatite-associated granophyre is equivalent to TDL magma after it was approximately 90% crystallized.

5-2 Genesis of sulfides in the TDL gabbro

Sulfides occur in the TDL gabbro and in Eastern gabbro xenoliths. However, the latter sulfides are rare and are compositionally distinct from those in the TDL gabbro. Sulfide mineralization in the TDL gabbro forms two petrographically and compositionally distinct types; the basal and main zone sulfides. The main zone sulfides crystallized from a sulfide liquid that coexisted with the TDL crystal mush, but the two were not at equilibrium. The sulfide liquid becomes Cu-rich during crystallization of pyrrhotite and was mobile in the crystal mush. Metals in the sulfide liquid are fractionated; the ascending order in which the geochemical behaviour of the metals becomes increasingly like that of Pd is Ni=Ir<<Rh=Pt<Cu<Au. There is no known phase that can account for this fractionation in a sulfide liquid.

It is proposed that the TDL sulfide liquid formed by the reaction of TDL silicate melt with sulfur that was continuously extracted from the country rock. Most of the sulfide liquid formed at depth prior to emplacement of the TDL gabbro into its present location. Infiltration of sulfur continued over an interval of time coincident with significant fractionation of the magma. The composition of newly formed sulfide droplets depends on the composition of the local silicate melt, and is, therefore, dependant on the time of formation. Early sulfide liquid was relatively Ni-rich, and was in equilibrium with olivine. Later sulfide liquid equilibrated with fractionated silicate melt, and, therefore, contained less Ni and Ir. The later sulfide liquid was not in equilibrium with olivine. Throughout sulfide melt formation, droplets that equilibrate with 'fresh' silicate melt will have nearly constant Cu/Fe and total Rh+Pt+Pd+Au/Cu ratios. At this point, prior to intrusion of the TDL gabbro, the sulfide liquid existed largely as widespread, isolated droplets with variable Ni and Ir concentrations. The volume of a droplet increases when it comes into contact with other droplets, and therefore, accumulation of abundant sulfides occurred by turbulence in the magma chamber. Turbulence occurred during convection and intrusion into the present site. Coincident with sulfide liquid movement through the magma, monosulfide

solid solution crystallized resulting in migration of sulfide liquid progressively enriched in Cu. Larger accumulations of sulfide liquid presumably contain more of the 'new' and relatively Ni- and Ir-depleted sulfide liquid, therefore, accounting for the observed fractionation trends.

The basal zone sulfides could not have formed by the settling out of sulfides from the main zone. It probably formed by continued sulfur addition to TDL magma that was previously depleted in Cu, Ni and PGE by an earlier generation of sulfide liquid. The silicate melt was more strongly depleted in PGE than Cu and Ni, a reflection of the relative partition coefficients. Therefore, basal zone sulfides have lower (diluted) metal concentrations, but have enriched Cu and Ni concentrations relative to PGE.

The proposed model of progressive sulfide liquid formation coincident with silicate magma fractionation is in part based on ideas of Stone et al. (1989) and Fleet & Stone (1990) to account for variable K_{D3} values of coexisting olivine and sulfides in basaltic rocks. In general, a common feature of quenched sulfide aggregates in extruded basaltic magmas is their heterogeneous composition (e.g., MacLean, 1977; Stone et al., 1989; Fleet & Stone, 1990; Peach et al. 1990). Stone et al. (1989) and Fleet & Stone (1990) proposed that variable compositions are due to timing of sulfide formation. They implied that sulfide aggregates

form a continuum of early to late, probably sub-solidus sulfide types that range in composition from those in equilibrium with olivine to those that are not. Also, for samples from Hawaii, Fleet & Stone (1990) stated that there was a general correlation between sulfide and host rock compositions, the most nickeliferous sulfides occurring within the most magnesian olivine, and Ni-poor and Cu-rich sulfides occurring within residual melt. One significant difference between the model for TDL sulfides and the ideas proposed by Fleet & Stone (1990) is the timing of the last sulfides to form. Fleet & Stone (1990) would have late sulfides forming at sub-solidus temperatures, perhaps by metasomatic processes, whereas petrographic evidence in the TDL gabbro suggests that the late sulfides were formed prior to intrusion of the gabbro into the present location.

The continuous addition of sulfur from country rock is an important part of this model. It is conceivable that sulfur in the TDL gabbro was derived from two possible sources, magma and country rock. At other deposits there is evidence that the latter sulfur source is more important. For example, the addition of wallrock sulfur is an important step in the formation of sulfide deposits in the Duluth Complex (references cited in Ripley and Alawi, 1986), and the Crystal Lake Intrusion (Eckstrand and Cogulu, 1986). Petrographic, tectonic and compositional similarities

between these deposits and the Marathon deposit imply that sulfur in the TDL gabbro could also have been derived from wallrock. Therefore, it is proposed that original sulfur in the TDL magma (mantle sulfur) played a small role in the formation of sulfides in the TDL gabbro.

5-3 Genesis of the Geordie Lake gabbro (MacRae occurrence)

The following three stages are proposed to have occurred during solidification of the GL gabbro:

(1) **Cumulus to early intercumulus stage** - The GL gabbro was emplaced as a crystal mush consisting of plagioclase and silicate melt. The plagioclase crystals formed a framework for crystallization of the interstitial melt and there was little, if any, crystal-free magma in the chamber. Solidification of the interstitial melt generated, in order of first appearance, weakly zoned plagioclase overgrowths, magnetite, olivine and clinopyroxene. Apatite crystallized prior to clinopyroxene and affected the composition of the residual melt.

(2) **Late intercumulus stage** - Normal post-cumulus crystallization was interrupted by infiltration of a highly evolved, possibly volatile-rich silicate magma into the crystal pile and the flushing out (or dilution?) of original interstitial melt. The late silicate melt migrated through interstices, crystallized sodic plagioclase, recrystallized

some of the cumulus plagioclase, partly resorbed clinopyroxene, and reacted with magnetite to form biotite and amphibole. Local accumulations of infiltrated melt crystallized microdikelets and pods consisting predominantly of saccharoidal sodic plagioclase. Three prominent textural features of the mineralized zone generated by injection of late silicate melt are (a) very coarse-grained plagioclase and clinopyroxene at albite pod-GL gabbro contacts, (b) dendritic and zoned olivine, and (c) heterogeneous gabbro. The first two features are presumably a result of the temperature gradient between the two melts and the latter a result of the mixing of crystals and the two magma types.

(3) **Deuteric stage** - A hydrous vapour phase separated from the infiltrated magma during plagioclase crystallization and reacted with the plagioclase, thereby removing K, Rb, Cs and, probably, Ba and Ca, leaving feldspar with a composition of 98-100 % albite. Migration of the hydrous vapour into the crystal pile resulted in the formation of interstitial amphibole and amphibole alteration rims on clinopyroxene.

5-4 Genesis of sulfides in the GL gabbro

There are three prominent types of sulfide mineralization in the MacRae occurrence: type 1 sulfides are ubiquitous in the GL gabbro and generate background metal

values; type 2 sulfides are disseminated and occur in broad discontinuous zones within the GL gabbro; and, type 3 sulfides occur either at the contact or within the quartz monzonite. Sulfide types 2 and 3 consist predominantly of chalcopyrite and bornite, and minor pyrite, galena and sphalerite, and are invariably intergrown with secondary amphibole (actinolite). Type 2 sulfides are spatially associated with albite rims, microdikelets and pods. Type 3 sulfides occur in stringers that cut GL gabbro and quartz monzonite. Type 2 sulfides are compositionally distinct from type 3 sulfides. The latter containing significant Pb and Zn concentrations and much less PGE. Type 2 sulfides are significantly enriched in Cu, Pd and Au, and somewhat lesser amounts of Rh and Ni, above background.

The textural and compositional features of sulfide mineralization are consistent with a deuteric hydrothermal origin. It is proposed that the hydrous fluid, generated during step 3 (section 5-3) above, subsequently equilibrated with evolved melt and nearby crystals and resulted in the removal of alkali metals, S, Fe, Cu, Pd and Au, and lesser amounts of Ni and Rh to the hydrous fluid. The fluid migrated through the crystal pile along grain interfaces. Deposition of type 2 sulfides coincided with local hydrothermal alteration of primary minerals and the deposition of interstitial actinolite.

The enriched Cu and Pd concentrations of the unmineralized gabbro (type 1 sulfides) probably represent trapped components introduced by the interstitial melt which invaded the cumulate pile. A late, presumably low temperature mineralizing event resulted in the formation of type 3 sulfides (stringer sulfides) in the quartz monzonite and at the contact with the GL gabbro.

References

- Ballhaus C.G. & Stumpfl E.F. (1986): Sulfide and platinum mineralization in the Merensky reef: Evidence from hydrous silicates and fluid inclusions. *Contr. Mineral. Petrol.* 94, 193-204.
- Barnes, S.-J. (1983): *The origin of the fractionation of platinum-group elements in Archean komatiites of the Abitibi Greenstone Belt, Northern Ontario, Canada.* Unpublished PhD thesis, University of Toronto.
- Barnes, S.-J., Boyd, R., Korneliussen, A., Nilsson, L.-P., Often, M., Pedersen, R.B. & Robins, B. (1988): The use of mantle normalization and metal ratios in discriminating between the effects of partial melting, crystal fractionation and sulfide segregation on platinum-group elements, gold, nickel and copper: examples from Norway. In *Geoplatinum* (Prichard, H.M., Potts, P.J., Bowles, J.F.W. & Cripp, S.J. eds.). Elsevier, London, (113-143).
- Barnes S.-J., Naldrett A.J. & Gorton M.P. (1985): The origin of the fractionation of platinum-group elements in terrestrial magmas. *Chemical Geology* 53, 303-323.
- Barnes, S.J. (1986): The effect of trapped liquid crystallization on cumulus mineral compositions in layered intrusions. *Contr. Min. Petrol.* 93, 524-531.
- Barnes, S.J. & Campbell I.H. (1988): Role of late magmatic fluids in Merensky-type platinum deposits. *Geol* 16, 488-491.
- Basaltic Volcanism Study Project (1981): *Basaltic volcanism on the terrestrial planets.* Pergamon Press Inc, New York, 1286 pages.
- Beswick, A.E. (1973): An experimental study of alkali metal distributions in feldspars and micas. *Geoch. Cosmoch. Acta* 37, 183-208.
- Boudreau A.E., Mathez E.A. & McCallum I.S. (1986): Halogen geochemistry of the Stillwater and Bushveld Complexes: evidence for transport of the platinum-group elements by Cl-rich fluids. *Journ. of Petrol.*, 27, 967-986.
- Boudreau A.E. & McCallum I.S. (1989): Investigations of the Stillwater Complex: Part V. Apatites as indicators of evolving fluid composition. *Contrib Mineral Petrol* 102, 138-153.

- Brugmann G.E., Arndt N.T., Hofmann A.W. & Tobschall H.J. (1987): Noble metal abundances in komatiite suites from Alexo, Ontario, and Gorgona Island, Columbia; *Geoch. Cosmoch. Acta* 51, 2159-2169.
- Campbell, I.H. & Naldrett, A.J. (1979): The influence of silicate:sulfide ratio on the geochemistry of the magmatic sulfides. *Econ. Geol.* 74, 1503-1505.
- Cannon, W.F., Green, A.G., Hutchinson, D.R., Myung Lee, Milkereit, B., Behrendt, J., Halls, H.C., Green, J.C., Dickas, A.B., Morey, G.B., Sutcliffe, R. & Spencer, C. (1989): The North American Midcontinent Rift beneath Lake Superior from GLIMPCE Seismic reflection profiling. *Tectonics* 8, 305-332.
- Capobianco, C.J. & Drake, M.J. (1990): Partitioning of ruthenium, rhodium, and palladium between spinel and silicate melt and implications for platinum group element fractionation trends. *Geochim. Cosmochim. Acta* 54, 869-874.
- Capobianco, C.J., Drake, M.J. & Rogers, P.S.Z. (1990): Experimental investigation of partitioning of noble siderophile elements among basaltic liquidus phases. *V.M. Goldschmidt Conf. Prog. Abstr.*, 35.
- Carmichael, I.S.E., Turner, F.J. & Verhoogen, J. (1974): Solid solution in ternary feldspars. In *Igneous Petrology*. McGraw-Hill, New York (223-227).
- Cerny, P., Smith, J.V., Mason R.A., & Delaney, J.S. (1984): Geochemistry and petrology of feldspar crystallization in the Vezna pegmatite, Czechoslovakia. *Can. Mineral.* 22, 631-651.
- Chalokwu, C.I. & Grant, N.K. (1990): Petrology of the Partridge River Intrusion, Duluth Complex, Minnesota: 1. Relationships between mineral compositions, density and trapped liquid abundance. *Jour. Petrol.* 31, 265-293.
- Chyi, L.L. & Crocket, J.H. (1976): Partition of platinum, palladium, iridium, and gold among coexisting minerals from the deep ore zone, Strathcona mine, Sudbury, Ontario. *Econ. Geol.* 71, 1196-1205.
- Clark, T. & Naldrett, A.J. (1972): The distribution of Fe and Ni between synthetic olivine and sulfide at 900°C. *Econ. Geol.* 67, 939-952.
- Craig, J.R. & Kullerud, G. (1969): Phase relations in the Cu-Fe-S system and their application to magmatic ore deposits. In *Magmatic Ore Deposits* (H.D.B. Wilson, ed.). *Econ. Geol. Mon.* 4, 344-358.

Craig, J.R. & Scott S.D. (1974): Sulfide Phase Equilibria. In Sulfide Mineralogy (P.H.Ribbe, ed.). Miner. Society of Am. Short Course Notes 1 (CS-1 to CS-109).

Crocket J.H. (1979) Platinum-group elements in mafic and ultramafic rocks; a survey: *Can. Mineral.* 17, 391-403.

Crocket J.H. (1981): Geochemistry of the platinum-group elements. In Platinum-Group Elements: Mineralogy, Geology, Recovery (ed. L.J. Cabri), *Can. Inst. Mining Metall. Spec. Vol.* 23, 47-64.

Crocket J.H. & MacRae W.E. (1986): Platinum-group element distribution in komatiitic and tholeiitic volcanic rocks from Munro Township, Ontario. *Econ. Geol.* 81, 1242-1251.

Crocket J.H., Fleet M.E. & Stone W.E. (in press): Experimental partitioning of osmium, iridium and gold between basalt melt and sulphide liquid at 1300°C. *Australian Jour. of Earth Sciences.*

Currie, K.L. (1980): A contribution to the petrology of the Coldwell alkaline complex, northern Ontario. *Geol. Surv. Can. Bull.* 239.

Davis, D.W. & Sutcliffe, R.H. (1985): U-Pb ages from the Nipigon plate and northern Lake Superior. *Geol. Society of Am. Bull.* 96, 1572-1579.

Doyle, C.D. & Naldrett, A.J. (1987): The oxygen content of "sulfide" magma and its effect on the partitioning of nickel between coexisting olivine and molten ores. *Econ. Geol.* 82, 208-211.

Eckstrand, O.R. & Cogulu, E. (1986): Se/S evidence relating to genesis of sulphides in the Crystal Lake Gabbro, Thunder Bay, Ontario. *Geol. Assoc. of Can./Mineral. Assoc. of Can./Can Geoph. Union Joint Annual Meeting, Program with Abstr.* 11, 66.

Fitton, J.G. & Upton, B.G.J. (1987): Introduction. In Alkaline Igneous Rocks, *Geological Society Special Publication* 30.

Fleet, M.E. (1974): Partition of Mg and Fe²⁺ in coexisting pyroxenes. *Contr. Mineral. and Petrol.* 44, 251-257.

Fleet, M.E. & MacRae, N.D. (1983): Partition of Ni between olivine and sulfide and its application to Ni-Cu sulfide deposits. *Contrib. Mineral Petrol* 83, 75-81.

Fleet, M.E. & MacRae, N.D. (1987): Partition of Ni between olivine and sulfide and its application to Ni-Cu sulfide deposits. *Contr. Mineral. Petrol.* 83, 75-81.

Fleet, M.E. & MacRae, N.D. (1988): Partition of Ni between olivine and sulfide: equilibria with sulfide-oxide liquids. *Contrib. Mineral Petrol.* **100**, 462-469.

Fleet, M.E. & MacRae, N.D., & Herzberg, C.T. (1977): Partition of nickel between olivine and sulfide: a test for immiscible sulfide liquids. *Contrib. Mineral. Petrol.* **65**, 191-197.

Fleet, M.E. & Stone, W.E. (1990): Nickeliferous sulfides in xenoliths, olivine megacrysts and basaltic glass. *Contr. Min. Petrol.* **105**, 629-636.

Fleet, M.E. & Stone, W.E. (1991): Partitioning of platinum-group elements in the Fe-Ni-S system and their fractionation in nature. *Geoch. Cosmoch. Acta* **55**, 245-253.

Fleet, M.E., Stone, W.E. & Crocket, J.H. (1991): Partitioning of palladium, iridium, and platinum between sulfide liquid and basalt melt: Effects of melt composition, concentration, and oxygen fugacity. *Geoch. Cosmoch. Acta* **55**, 2545-2554.

Fujimaki, H (1986): Partition coefficients of Hf, Zr, and REE between zircon, apatite, and liquid. *Contr. Min. Petrol.* **94**, 42-45.

Good, D.J. & Crocket, J.H. (1989): PGE study of the MacRae and Marathon Cu-precious metal deposits, Coldwell complex. In Geoscience Research Grant Program, Summary of Research 1988-1989, *Ont. Geol. Surv. Misc. Paper* **143**, 186-198.

Grant, N.K. & Molling, P.A. (1981): A strontium isotope and trace element profile through the Partridge River Troctolite, Duluth Complex, Minnesota. *Contr. Min. Petrol.* **77**, 296-305.

Green, T.H. & Pearson, N.J. (1987): An experimental study of Nb and Ta partitioning between Ti-rich minerals and silicate liquids at high pressure and temperature. *Geoch. Cosmoch. Acta* **51**, 55-62.

Haselton, J.D. & Nash, W.P. (1975): Ilmenite-orthopyroxene intergrowths from the moon and the Skaergaard intrusion. *Earth Plan. Sci. Lett.* **26**, 287-291.

Heaman L.M. & Machado N. (1987): Isotope geochemistry of the Coldwell alkaline complex. I U-Pb studies on accessory minerals. G.A.C.-M.A.C. Annual Meeting, Abstracts with Programs, Saskatoon, p. 54.

Henderson, P (1984): General geochemical properties and abundances of the rare earth elements. In *Rare Earth Element Geochemistry* (P. Henderson, ed.). Elsevier (1-32).

Hoffman, E.L., Naldrett, A.J., Van Loon, J.C., Hancock, R.G.V. & Mason, A. (1978): The determination of all the platinum-group elements and gold in rocks, ores, etc. *Analytical Chimical Acta* 102, 157-166.

Hutchinson, C.S. (1974): *Laboratory Handbook of Petrographic Techniques*. Wiley - Interscience.

Irvine, T.N. (1974): Petrology of the Duke Island ultramafic complex, Southeastern Alaska. *Memoir Geol. Soc. Amer.* 138, 19-140.

Irving, A.J. (1978): A review of experimental studies on crystal/liquid trace element partitioning. *Geoch. Cosmoch. Acta* 42, 743-770.

Kretz, R. (1961): Some applications of thermodynamics to coexisting minerals of variable composition. Examples: orthopyroxene-clinopyroxene and orthopyroxene-garnet. *J. Geol.* 69, 361-387.

Lightfoot, P.C., Naldrett, A.J. & Hawkesworth, C.J. (1984): The geology and geochemistry of the Waterfall gorge section of the Insizwa Complex with particular reference to the origin of the nickel sulfide deposits. *Econ. Geol.* 79, 1857-1879.

Lightfoot, P.C., Conrod, D., Naldrett, A.J. & Evensen, N.M. (1987): Petrologic, chemical, isotopic and economic-potential studies of the Nipissing Diabase. In *Geoscience Research Grant Program, Summary of Research 1986-1987, Ont. Geol. Surv. Misc. Paper* 136, 4-26.

MacLean, W.H. (1977): Sulfides in Leg 37 drill core from the Mid-Atlantic Ridge. *Can. J. Earth Sci.* 14, 674-683.

Mainwaring, P.R. & Naldrett, A.J. (1977): Country-rock assimilation and the genesis of Cu-Ni sulfides in the Water Hen intrusion, Duluth Complex, Minnesota. *Econ. Geol.* 72, 1269-1284.

Makovicky M., Makovicky E., & Rose-Hanson J. (1986): Experimental studies on the solubility and distribution of PGE in base-metal sulphides in platinum deposits. In *Metallogeny of basic and ultrabasic rocks* (M.J. Gallagher, R.A. Ixer, C.R. Neary and H.M. Prichard, eds). Institution of Mining and Metallurgy.

- Mathez, E.A. (1989): Vapor associated with mafic magma and controls on its composition. In Ore deposition associated with magmas (J.A. Whitney & A.J.Naldrett, eds.) *Reviews in Econ. Geol.* 4 (21-32).
- Mathez, E.A. & Peach, C.L. (1989): The geochemistry of the platinum-group elements in mafic and ultramafic rocks. In Ore deposition associated with magmas (J.A. Whitney & A.J.Naldrett, eds.) *Reviews in Econ. Geol.* 4 (33-43).
- McBirney A.R. (1986): Constitutional zone refining of layered intrusion. In *Origins of igneous layering* (I. Parsons ed.) NATO ASI Series, D. Reidel Publ. (437-452).
- Medaris, L.G., Jr. 1969: Partitioning of Fe⁺⁺ between coexisting synthetic olivine and orthopyroxene. *Am. J. Sci.* 267, 945-968.
- Mitchell, R.H., Laflamme, J.H.G & Cabri, L.J. (1989): Rhenium sulphide from the Coldwell complex, northwestern Ontario, Canada. *Miner. Magazine* 53, 635-637.
- Mitchell R.H. & Platt R.G. (1982): Mineralogy and petrology of nepheline syenites from the Coldwell alkaline complex, Ontario, Canada. *Jour. of Petrol.* 23, 186-214.
- Mitchell R.H., Platt R.G. & Cheadle S.P. (1983): A gravity study of the Coldwell complex, northwestern Ontario and its petrological significance. *Can. J. Earth Sci.* 20, 1631-1638.
- Mountain B.W. & Wood S.A. (1988) Chemical controls on the solubility, transport, and deposition of platinum and palladium in hydrothermal solutions: a thermodynamic approach. *Econ. Geol.* 83, 492-510.
- Mountain, B.W. & Wood, S.A. (1988): Solubility and transport of platinum-group elements in hydrothermal solutions: thermodynamic and physical chemical constraints. In *Geoplatinum* (Prichard, H.M., Potts, P.J., Bowles, J.F.W. & Cripp, S.J. eds.). Elsevier, London (57-82).
- Muan, A. (1979): Crystallization in silicate systems. In *The evolution of the igneous rocks* (H.S. Yoder, Jr., ed.). Princeton University Press, New Jersey (77-129).
- Mulja, T. (1989): *Petrology, Geochemistry, Sulphide and Platinum-Group Element Mineralization of the Geordie Lake Intrusion, Coldwell Complex, Ontario*. M.Sc. thesis, Lakehead Univ., Thunder Bay, Ontario.
- Mulja T. & Mitchell R.H. (1990): Platinum-group minerals and tellurides from the Geordie Lake intrusion, Coldwell complex, Northwestern Ontario. *Can. Mineral.* 28, 489-502.

Mulja T. & Mitchell R.H. (1991): The Geordie Lake intrusion, Coldwell Complex, Ontario: A palladium- and tellurium-rich disseminated sulfide occurrence derived from an evolved tholeiitic magma. *Econ. Geol.* 86, 1050-1069.

Nafziger, R.H. & Muan, A. (1967): Equilibrium phase compositions and thermodynamic properties of olivines and pyroxenes in the system $MgO-FeO-SiO_2$. *Am. Mineral.* 52, 1364-1385.

Naldrett, A.J. (1969): A partition of the system Fe-S-O between 900°C and 1080°C and its applications to sulfide ore magmas. *Jour. Petrology* 10, 171-201.

Naldrett A.J. (1981) Nickel Sulfide Deposits: Classification, Composition, and Genesis. In *Economic Geology, Seventy-Fifth Anniversary Volume* (ed. B.J. Skinner)

Naldrett, A.J. (1989): Experimental studies on sulfide, sulfide oxide, and sulfide silicate systems. In *Magmatic sulphide deposits, Oxford Monographs on Geology and Geophysics* 14, 17-37.

Naldrett, A.J. (1989): Ores associated with flood basalts. In *Ore deposition associated with magmas* (J.A. Whitney & A.J. Naldrett, eds.) *Reviews in Econ. Geol.* vol 4 (103-118).

Naldrett A.J. & Cabri L.J. (1976) Ultramafic and related mafic rocks: their classification and genesis with special reference to the concentration of nickel sulfides and platinum-group elements: *Econ. Geol.* 71, 1131-1158.

Naldrett, A.J., Hoffman, E.L., Green, A.H., Chen-Lin Chou, & Naldrett, S.R. (1979): The composition of Ni-sulfide ores, with particular reference to their content of PGE and Au. *Can. Mineral.* 17, 403-415.

Newhouse, W.H. (1936): Opaque oxides and sulphides in common igneous rocks. *Bull. Geol. Soc. Amer.* 47, 1-52.

Nyman, M.W., Sheets, R.W. & Bodnar, R.J. (1990): Fluid-inclusion evidence for the physical and chemical conditions associated with intermediate-temperature PGE mineralization at the New Rambler deposit, southeastern Wyoming. *Can Mineral.* 28, 629-638.

Ohnenstetter, D., Watkinson, D.H. & Dahl, R. (1989): Platinum Group Minerals from the Two Duck Lake Intrusion, Coldwell Complex, Canada. *Bulletin of the Geological Society of Finland* 61.

Ohnenstetter, D. & Watkinson, D.H. (1991): Platinum-group mineralogy in Cu-rich sulfides, Two Duck Lake intrusion, Coldwell complex, northwestern Ontario, Canada. In 6th

International Platinum Symposium Programme and Abstracts.
International Association on Genesis of Ore Deposits.

- Osborn, E.F. (1979): The reaction principle. In *The evolution of the igneous rocks* (H.S. Yoder, Jr., ed.). Princeton University Press, New Jersey (133-170).
- Patterson, G.C., Scott J.F., Mason J.K., Schnieders B.R., MacTavish A.D., Dutka R.J., Kennedy M.C., White G.D. and Hinz P. (1987): Report of activities (1986) Regional and Resident Geologist. *Ont. Geol. Surv. Miscell. Paper 134*, 113-115.
- Pearce, J.A. & Norry, M.J. (1979): Petrogenetic implications of Ti, Zr, Y, and Nb variations in volcanic rocks. *Contr. Min. Petrol.* **69**, 33-47.
- Philpotts, J. (1970): Redox estimation from a calculation of Eu^{2+} and Eu^{3+} concentrations in natural phases. *Earth Planet. Sci. Lett.* **9**, 257-268.
- Peach, C.L. Mathez, E.A. & Keays, R.R. (1990): Sulfide melt-silicate melt distribution coefficients for noble metals and other chalcophile elements as deduced from MORB: Implications for partial melting. *Geoch. Cosmoch. Acta* **54**, 3379-3399.
- Platt, R.G. & Mitchell, R.H. (1982): Rb-Sr geochronology of the Coldwell Complex, northwestern Ontario, Canada. *Can. J. Earth Sci.* **19**, 1796-1801.
- Puskas, F.P. (1967): Port Coldwell area. *Ontario Department of Mines, Preliminary Map P.114*.
- Rao B.V. & Ripley, E.M. (1983): Petrochemical studies of the Dunka road Cu-Ni deposit, Duluth Complex, Minnesota. *Econ. Geol.* **78**, 1222-1238.
- Ringwood, A.E. (1961): Chemical and genetic relationships among meteorites. *Geoch. Cosmoch. Acta*, **24**, 159-197.
- Ripley, E.M. & Alawi, J.A. (1986): Sulfide mineralogy and chemical evolution of the Babbitt Cu-Ni deposit, Duluth complex, Minnesota. *Can. Mineral.* **24**, 347-368.
- Sage, R.P. (1991): Alkalic Rock, Carbonatite and Kimberlite Complexes of Ontario, Superior Province. In *Geology of Ontario, Ont. Geol. Surv. Special Vol. 4, Part 1* (683-709).
- Schiffries, C.M. (1982): The petrogenesis of a platiniferous dunite pipe in the Bushveld Complex: infiltration metasomatism by a chloride solution. *Econ. Geol.* **77**, 1439-1453.

Schwartz, G.M. (1930): The relations of magnetite and ilmenite in the magnetite deposits of the Duluth gabbro. *Am. Mineral.* 15, 243-253.

Sharpe, M.R. (1982): Noble metals in the marginal rocks of the Bushveld Complex. *Econ. Geol.* 77, 1286-1295.

Shaw, D.M. (1968): A review of K-Rb fractionation trends by covariance analysis. *Geoch. Cosmoch. Acta* 32, 573-601.

Shaw, D.M. (1970): Trace element fractionation during anatexis. *Geoch. Cosmoch. Acta* 34, 237-243.

Smirnov, V.I. (1960): The deposits of the Noril'sk region. In *Ore deposits of the U.S.S.R.*, Vol. III (V.I. Smirnov ed.: translated by D.A. Brown into English) (34-46).

Smith, R.K. & Lofgren, G.E. (1983): An analytical and experimental study of zoning in plagioclase. *Lithos* 2, 153-168.

Smyk, M.C. (1986): *Macroscopic Petrography of Sulphide Mineralization at the Marathon Pt-Pd-Cu Property, Coldwell Alkaline Complex, Northwestern Ontario*. unpublished study, Department of Geology, Carleton University, Ottawa, Ontario.

Stone, W.E., Crocket, J.H. & Fleet, M.E. (1990): Partitioning of palladium, iridium, platinum, and gold between sulfide liquid and basalt melt at 1200°C. *Geoch. Cosmoch. Acta* 54, 2341-2344.

Stone, W.E., Fleet, M.E. & MacRae, N.D. (1989): Two-phase nickeliferous monosulfide solid solution (mss) in megacrysts from Mount Shasta, California: A natural laboratory for nickel-copper sulfides. *Am. Mineral.* 74, 981-993.

Streckeisen, A. (1976): To each plutonic rock its proper name. *Earth-Sci. Reviews* 12, 1-33.

Stumpfl E.F. & Ballhaus C.G. (1986): Stratiform platinum deposits: new data and concepts. *Fortschr. Miner.* 64-2, 205-214.

Sutcliffe, R.H. (1991): Proterozoic Geology of the Lake Superior Area. In *Geology of Ontario, Ontario Geological Survey, Special Volume 4, Part 1* (627-660).

Usselman, T.M., Hodge, D.S., Naldrett, A.J. & Campbell, I.H. (1979): Physical constraints on the characteristics of nickel-sulfide ore in ultramafic lavas. *Can. Mineral.* 17, 361-372.

Wadsworth, W.J. (1985): Terminology of postcumulus processes and products in the Rhum layered intrusion. *Geol. Mag.* 122, 549-554.

- Wager, L.R., Brown, G.M. & Wadsworth, W.J. (1960): Types of igneous cumulates. *Jour. Petrol.* 1, 73-85.
- Watkinson, D.H., Whittaker, P.J. & Jones, P.L. (1983): Platinum group elements in the Eastern gabbro, Coldwell complex, northwestern Ontario. *Ont. Geol. Surv. Misc. Paper* 113, 183-191.
- Watkinson D.H., Dahl R. & McGoran J. (1986) The Coldwell complex platinum-group element deposit: 2. Relationships of platinum-group elements to pegmatitic biotite-bearing gabbro and the role of a fluid phase [abs]: G.A.C.-M.A.C. Program with Abstracts, v. 11, p. 143.
- Watson, E.B & Capobianco, C.J. (1981): Phosphorus and the rare earth elements in felsic magmas: an assessment of the role of apatite. *Geoch. Cosmoch. Acta* 45, 2349-2358.
- Watson, E.B. & Harrison, T.M. (1984): Accessory minerals and the geochemical evolution of crustal magmatic systems: a summary and prospectus of experimental approaches. *Physics of Earth and Planet. Interiors* 35, 19-30.
- Webster, J.D. & Holloway, J.R. (1988): Experimental constraints on the partitioning of Cl between topaz rhyolite melt and H₂O and H₂O+CO₂ fluids: New implications for granitic differentiation and ore deposition. *Geoch. Cosmoch. Acta* 52, 2091-2105.
- Weiblen, P.W. (1982): Keweenawan intrusive igneous rocks. *Memoir Geol. Soc. Amer.* 156, 57-82.
- Whittaker P.J. (1979): *Geology of the east central Port Coldwell complex from Pic River to Red Sucker Cove*. M.Sc. thesis, McMaster University, Hamilton, Ontario.
- Wiebe, R.A. (1968): Plagioclase stratigraphy: a record of magmatic conditions and events in a granite stock. *Am. J. Sci.* 266, 690-703.
- Wilkinson, S.J. (1983): *Geology and sulphide mineralization of the marginal phases of the Coldwell Complex, Northwestern Ontario*. M.Sc. thesis, Carleton University, Ottawa, Ontario.
- Wood, B.J. & Fraser, D.G. (1977): *Elementary thermodynamics for geologists*. Oxford University Press, Oxford
- Wood, S.A. (1987): Thermodynamic calculations of the volatility of the platinum-group elements (PGE) at magmatic temperatures. *Geoch. Cosmoch. Acta* 51, 3041-50.
- Yoder, H.S. & Tilley, C.E. (1962): Origin of basalt magmas: An experimental study of natural and synthetic rock systems. *Jour. Petrol.* 3, 342-532.

Appendix I - Analytical Methods for Whole-rock Data

Introduction

This section describes techniques used to collect a wide spectrum of whole-rock geochemical data from both the Geordie Lake Gabbro (MacRae occurrence) and the Two Duck Lake Gabbro (Marathon deposit). Samples from the former deposit are indicated by the prefix G and the latter by F.

The data is presented in the order that analytical techniques are described. The data can be found in the following tables:

- a) whole rock major-element data in Tables AI-4 and 5,
- b) trace-element data (including Cl and U) in Tables AI-6 and AI-7,
- c) REE, Ta, Th, Hf, Cs and Sc in Table AI-12,
- d) PGE, S, Cu, and Ni in Tables AI-13 and 14.

Sample selection

Samples collected for this study were selected from diamond drill core and outcrop available at both deposits. Samples G1 to G46, F1 to F15, F200d, F200w and F34 to F37 were collected from outcrops and the remainder from diamond drill core. Those collected from outcrop were larger (at least 1 kg) than those from the drill core (at least 500 g) since the latter were restricted by the respective exploration company to a maximum of 15 cm of core.

Sample preparation

Samples were crushed to 1 cm chips in a jaw steel crusher, reduced to 1 to 2 mm chips in a ceramic lined disk grinder then ground to <200 mesh in a tungsten carbide mill. Cobalt (approximately 50 to 100 ppm) and W were introduced to the samples from the tungsten carbide mill.

Major- and trace-element analysis by XRF

The major-elements were analysed by X-Ray Fluorescence on fused glass discs, prepared using a La oxide flux (methods of Norris and Chappel, 1977). The trace-elements Ni, Cu, S, Ba, Cr, Pb, Zn, V, Nb, Rb, Sr, Y and Zr were determined on pressed powder pellets.

Analyses were calibrated using several international standards. Accuracy of the analyses was tested by comparing a second suite of standards, analysed as unknowns, with the recommended values of Govindaraju (1984). The results of this test are listed in Tables AI-1 and 2 and indicate good agreement. Several samples were run in duplicate to test the reproducibility of analyses. The results are listed in Table AI-3. In general, agreement between duplicates is good (<5%), but the G samples show approximately 10% variation for Fe₂O₃, Al₂O₃ and SiO₂.

All trace- and major-element data obtained by XRF analysis including Cl and U are listed in Tables AI-4, 5, 6 and 7.

Trace-element analysis by INAA

REE, Ta, Th, Hf, Cs, Sc, Cl, U, and the Platinum-group elements were analysed by Instrumental Neutron Activation Analysis (INAA) at the McMaster Nuclear Reactor. The methods and rock standards used are summarized in Table AI-8. Samples and standards were counted with a 19.8% efficient coaxial hyperpure Ge detector with a resolution of 1.9 keV at the 1332-keV ⁶⁰Co peak. The detector was coupled to an APTEC Windows based PC multichannel analyzer.

Counting error and precisison of INAA data

Reproducibility of analysis is checked by analysing several replicates of individual samples. The results are listed in Table AI-9. In general, the

reproducibility is close to 5%. Exceptions are Cl (20% for G84), Ho (12%) and Cs (18%). These variations are slightly greater than the counting errors for the respective concentrations. The counting error on each sample is calculated using the following formula:

$$\sqrt{\frac{((\text{Peak}_{\text{std}} + \text{Background}_{\text{std}}))^2}{(\text{Peak}_{\text{std}} - \text{Background}_{\text{std}})} + \frac{((\text{Peak}_{\text{sample}} + \text{Background}_{\text{sample}}))^2}{(\text{Peak}_{\text{sample}} - \text{Background}_{\text{sample}})}}$$

which gives 95% confidence limits of counting errors. The counting error increases with decreasing abundance so the error is reported for specific ranges of concentration in Table AI-10. Note that PGE are treated separately below.

Rare earth element, Ta, Th, Hf, Cs and Sc analysis

Eighteen samples were irradiated at the McMaster Nuclear Reactor to determine their rare-earth element, Ta, Th, Hf, Cs and Sc concentration (listed in Table AI-12). The samples, weighing approximately 0.5 g each, were sealed in 1.5 cm³ polyethylene vials. Samples were irradiated with standards SY-2 and MRG-1.

In order to optimize counting conditions for the diverse characteristics of the REE isotopes the samples were irradiated twice and counted at three separate times (see Table AI-11). The first irradiation was for 1 hour with an epithermal flux of approximately 1.6×10^{11} n/(cm²xs). The second irradiation, which was approximately 14 days after the first, was for 3.5 hours with a thermal flux of approximately 8×10^{12} n/(cm²xs).

Counting was done in three sessions. The first was three days after the first irradiation. The second was 7 days after the second irradiation and the third four weeks later.

Enhancement of light REE by U fission: The effects of primary interference reactions (produced by U fission) on the abundances of Sm, La, Nd and Ce as reported by Landsberger and Simsons (1987) and Landsberger (1986) were evaluated. In all cases the apparent concentration due to U is less than 1.6% of the measured concentration and this is less than the statistical counting errors which are typically 5%, consequently, corrections were not made to the data.

Chlorine analysis

Samples weighing approximately 0.4 g were irradiated using Rabbit system #4 for 10 s in a thermal flux of approximately 6.5×10^{12} n/(cm²xs). They were allowed to decay for 1 hr and then counted for 600s. The detection limit is approximately 60 ppm and is dependent on the amount of Na and Mn in the sample. All Cl analyses are listed in Table AI-7. All of the Two Duck Lake Gabbro samples were analysed but concentrations are below the detection limit.

Uranium analysis

Samples were analysed for U by delayed neutron counting. Samples weighing approximately 0.4 g were irradiated for 60 s, then allowed to decay for 10 s and counted for 60s. The technique is based on counting neutrons emitted by fission products of ²³⁵U generated by thermal neutron activation of the uranium isotope. Some of the fission products emit delayed neutrons with half-lives ranging from 0.3 to 56s (Laul 1979). These neutrons were counted using a boron trifluoride in polyethelene matrix detector.

The detection limit was found to be approximately 0.5 ppm. This detection limit is much higher than that found under optimum conditions because of the high level of contamination inherent to the system. The

contamination was measured during the session by analysing 6 blanks. The resulting blank correction factor was subtracted from the sample counts. The error due to this procedure is on the order of 5.4% (1 sigma variation for the 6 blanks).

The blank corrected sample counts were compared to those for U standards and calibrated against those of international standard SY-2 and W-1. All U data are listed in Table AI-7. Analysis of the Two Duck Lake Gabbro samples was attempted but concentrations were found to be below the detection limit.

Platinum-group element analysis

The abundance of platinum-group elements in the samples is very low and requires a pre-concentration step prior to INAA. Therefore, PGE and Au are determined by the fire assay-neutron activation technique described by Hoffman et al. (1978). In order to optimize counting conditions for the isotopes of interest samples are irradiated and counted twice (see Table AI-11). The first irradiation is used to determine Rh and Pd and the second Au, Pt and Ir. All PGE data are listed in Tables AI-13 and 14.

Fire assay/acid dissolution pre-concentration: Briefly, 50 g of sample were fused with a flux, consisting of 60g Na_2O_4 and 30g NaCO_3 , and enough Ni and S to bring the total amount to 16g and 10g, respectively. The samples were fused for 2 hours at 1000°C . The resulting sulfide beads were crushed and dissolved in 400ml of hot HCl. The dissolution takes approximately 2 hours. The PGE and Au are insoluble and were filtered off through a millipore (5 um pore) vacuum filtering system. The filter paper is neatly folded and sealed into a small package of plastic freezer wrap. These packets were then irradiated at the McMaster Nuclear Reactor. Eleven

replicates of the standard SARM7 were prepared in the same way, except only 20g of powder was used for each.

Rh and Pd determination: To determine Rh and Pd the filter papers were irradiated using Rabbit system #4 for 10 s in a thermal flux of approximately 6.5×10^{12} n/(cm²xs). They were allowed to decay for 90 seconds then counted for 200s. The filters were analysed over a period of several days. In order to compare data from each session the neutron flux in the reactor was monitored by irradiating and counting six aliquots of sulfur: three at the beginning and three at the end of each session.

Rh and Pd concentrations are calculated in a two step procedure. First, all of the sample and standard data is normalized using the respective flux factors calculated from the sulfur data. Then the Pd and Rh liquid standard data is compared to the samples and calibrated using the average of counts for all of the SARM-7 standards.

Pt, Ir and Au determination: To determine Ir, Pt and Au the filter papers were re-irradiated in the RIFLS position (9c or 9d) for 1 hour in a thermal flux of approximately 8×10^{12} n/(cm²xs). The samples were allowed to decay for five to six days then counted for 1500 to 7200 seconds depending on the sample.

The samples were irradiated in several batches. A piece of Co wire (flux monitor) and two SARM 7 standards were included in each batch. After all of the samples were irradiated and counted the individual pieces of Co wire were counted and the respective analyses were normalized to the appropriate flux factor. In this way the average count rates for all of the SARM-7 standards could be used to determine the sample concentrations.

Au interference on Pt analysis: The neutron flux available at the McMaster Reactor is sufficiently high that it is necessary to evaluate the production of Au199 from the conversion of Au197 (Crocket 1981). The Au199 produced in this manner will add to that produced by the conversion of Pt198. This is important since Pt concentrations are measured by counting the radiation emitted from the Au199 at 158 keV. To evaluate this effect a pure gold standard was irradiated along with the samples and counted. The response in the 158 KeV region resulting from ^{199}Au generated by the $^{197}\text{Au}(2n, \gamma)^{199}\text{Au}$ is a maximum of 1 ppb Pt for each ppb Au in the sample. The corrections due to this effect are not made because the Pt/Au ratio of the samples (4 to 40) brackets the value for the SARM-7 standard (12). The maximum error for Pt concentrations corresponding to this effect is on the order of 5 to 10 %.

Precision: The precision of the method, based on the analyses of ten replicates of the SARM-7 standard, is reported in Table AI-15. The precision (standard deviation as a percent of mean measured value) for Pt, Rh, and Pd is less than 7 %, for Ir 5.5%, and Au 34%. The counting error for these elements is less than 3% for all of the standards. The counting error for each sample is calculated using the formula in the section titled 'Counting error and reproducibility of INAA data'. The results are reported in Table AI-16 for specific ranges of concentration.

Reproducibility of sample analyses is listed in Table AI-17. As predicted by the inspection of the counting errors reported in Table AI-16 the variation between duplicates decreases with increasing concentration.

Au analysis by this method is not very precise, the standard deviation for 10 SARM7 samples is 34%. One possible explanation for this lack of precision is

related to the behaviour of Au. Perhaps the Au occurs in the sulfide bead as native metal and when the bead is crushed Au is smeared into small crevices in the mill wall. Precautions taken to minimize this effect were a) samples were crushed in order of ascending sulfur concentration and b) the mill was thoroughly cleaned and wiped with acetone after each sample was crushed. Despite these precautions the precision of Au analysis is poor and this data should be treated accordingly.

Contamination: To evaluate possible FGE contamination introduced during the preconcentration procedure, three blank samples were analysed with the others. The blank samples were prepared using 20 g of pure silica powder instead of 50 g of sample and followed all of the steps outlined above. Very small quantities of Au and Ir were detected in the blank samples. However, later analysis of the pure silica powder revealed a small quantity of Au, therefore Au contamination was not evaluated by this procedure. A very low level of Ir was detected in the blanks by counting them for a period of 5 hours approximately 1 month after the samples were counted. Results for the three blanks give an average of 0.138 counts/s \pm 28% (1 sigma) relative to the normal 7 day cooling off period allowed for the samples. This count rate was subtracted from the sample counts and is equivalent to 0.019 ppb, roughly half of the lowest Ir concentration in the samples. Although this correction factor introduces error to the low level analyses it is not greater than the variation measured between duplicates (see above). Two possible sources for this Ir contamination are the pure Ni powder and the steel mill used for crushing the sulfide beads.

Table AI-4: Major element data for the Marathon deposit. Rock types are as follows: tdl=Two Duck Lake gabbro; peg=pegmatitic TDL gabbro; gran=TDL granophyre; x1=fine-grained gabbronorite xenolith; x2=fine-grained olivine gabbronorite xenolith with olivine blasts (upto 2 cm); x3=fine-grained olivine gabbronorite xenolith with poikilitic pyroxene, olivine and magnetite crystals; x4=medium-grained mela-olivine gabbronorite xenolith; x5=fine-grained mela-gabbronorite xenolith; x6=medium-grained olivine gabbronorite xenolith; x7=medium-grained gabbronorite xenolith. All values are in percent.

sample rock type	F1 tdl	F2 tdl	F3 tdl	F4 tdl	F5 tdl	F6 tdl	F7 tdl	F8 tdl	F8c tdl
SiO2	48.46	48.17	48.45	46.50	46.89	47.91	47.45	45.32	48.21
Al2O3	13.11	13.40	13.16	13.20	12.69	13.17	13.92	13.75	15.24
Fe2O3	18.95	17.04	17.87	18.93	19.27	18.55	10.43	13.98	11.17
MgO	8.06	7.87	7.85	7.80	7.98	7.54	8.48	8.48	8.59
CaO	12.36	13.00	12.88	13.67	13.77	12.87	13.53	13.06	12.74
Na2O	2.01	1.95	2.30	1.92	1.96	1.87	2.03	1.97	1.50
K2O	0.37	0.41	0.35	0.25	0.29	0.47	.40	.41	0.28
TiO2	0.65	0.73	0.68	0.57	0.51	0.46	.54	.81	0.51
P2O5	0.16	0.19	0.14	0.22	0.26	0.13	.19	.23	0.18
MnO	0.16	0.16	0.14	0.15	0.15	0.12	.15	.16	0.17
Total	99.67	99.22	99.38	97.78	99.87	97.86	98.40	99.57	98.59

sample rock type	F9 tdl	F15 tdl	F18 tdl	F19 tdl	F29 tdl	F30 tdl	F31 tdl	F32 tdl	F200d tdl
SiO2	47.79	47.86	46.00	47.04	46.17	44.97	45.15	45.12	48.14
Al2O3	16.81	15.67	15.02	13.23	11.50	12.13	12.57	13.58	14.87
Fe2O3	10.84	12.14	14.12	14.12	17.02	17.70	17.53	17.36	11.25
MgO	7.53	6.73	8.61	9.05	7.53	7.40	6.43	6.31	9.00
CaO	12.72	12.66	12.00	11.47	11.86	11.54	12.09	11.87	12.90
Na2O	2.41	2.42	2.00	1.91	1.96	1.72	2.01	1.87	1.53
K2O	0.36	0.42	0.33	0.51	0.49	0.43	0.37	0.44	0.22
TiO2	0.55	1.48	0.66	0.92	1.15	0.77	1.32	0.99	0.58
P2O5	0.17	0.25	0.18	0.30	1.24	0.37	0.57	0.58	0.28
MnO	0.14	0.14	0.15	0.20	0.21	0.22	0.19	0.19	0.17
Total	99.34	99.86	99.09	100.07	99.13	97.26	98.24	98.29	98.94

sample rock type	F8p peg	F21 peg	F22 peg	F23 peg	F24 peg	F26 peg	F25 gran	F200w gran	F11 x1
SiO2	48.03	47.86	43.71	46.81	45.81	45.72	56.04	66.47	50.85
Al2O3	12.92	17.96	13.38	11.64	14.20	12.66	8.34	13.45	15.30
Fe2O3	11.49	10.56	19.07	15.01	16.30	16.22	10.73	4.67	10.51
MgO	10.30	5.09	11.06	8.84	6.61	6.81	6.60	2.47	7.09
CaO	13.93	12.21	8.98	13.43	11.72	12.95	10.92	4.24	11.75
Na2O	1.06	2.34	1.82	1.60	2.05	1.99	1.89	2.86	2.57
K2O	0.26	0.55	0.30	0.33	0.52	0.42	1.71	3.33	0.19
TiO2	0.52	1.05	0.42	1.13	1.73	1.94	1.02	0.66	1.04
P2O5	0.13	0.23	0.19	0.18	0.29	0.30	0.14	0.63	0.08
MnO	0.18	0.13	0.25	0.180	.19	0.19	0.17	0.13	0.11
Total	98.82	97.97	99.18	99.04	99.41	99.73	97.46	98.91	99.50

sample rock type	F37 x1	F12 x2	F13 x3	F14 x4	F36 x4	F16 x5	F17 x5	F34 x6	F35 x6	F27 x7
SiO2	51.48	49.94	46.20	42.15	45.37	51.23	51.67	45.86	45.90	56.36
Al2O3	16.14	15.12	17.34	9.10	9.40	6.11	5.97	12.79	11.93	14.00
Fe2O3	9.99	10.41	13.54	22.07	16.01	10.08	10.35	15.24	15.71	7.46
MgO	8.07	7.61	10.10	16.11	16.44	15.62	16.08	12.36	11.09	4.60
CaO	8.54	12.36	9.92	8.19	8.53	14.98	13.80	9.96	9.45	10.45
Na2O	2.77	2.72	2.06	1.23	2.13	0.89	1.29	1.51	2.89	3.28
K2O	0.19	0.28	0.30	0.24	0.26	0.16	0.17	0.26	0.29	1.50
TiO2	1.68	0.77	0.14	0.44	0.75	0.38	0.42	1.60	1.65	0.58
P2O5	0.05	0.09	0.12	0.20	0.15	0.14	0.10	0.19	0.19	0.17
MnO	0.21	0.08	0.16	0.29	0.26	0.19	0.14	0.25	0.26	0.14
Total	99.10	99.48	99.88	100.01	99.36	99.77	99.51	99.02	99.36	98.63

Table AI-6: Trace-element data for the Marathon deposit.

	Ba	Cr	Pb	Ni	Zn	V	Nb	Rb	Sr	Y	Zr
F1	336	89	7.8	117	68	237	6.7	8.6	694	12	53
F2	344	105	7.7	114	68	282	9.6	12	670	13	60
F3	315	108	11	325	83	282	3.6	5.4	665	9	46
F4	248	215	13	464	83	197	0.4	3.9	688	7	34
F5	266	174	11	189	64	166	3.3	2.2	697	12	39
F6	277	97	3.5	342	109	130	4.3	13	664	10	57
F7	259	121	2.0	240	78	145	5.8	15	635	12	47
F8	261	156	7.8	308	103	228	9.0	18	517	15	65
F8c	296	104	13	406	131	149	10	9.1	599	13	37
F8p	276	251	10	458	152	204	5.3	15	445	12	40
F9	326	112	4.0	147	69	213	3.9	5.0	735	9.9	46
F11	106	333	2.3	161	63	216	2.1	3.6	527	11	29
F12	142	454	2.0	129	65	251	4.9	1.9	490	14	21
F13	317	16	3.4	132	50	59	0.9	4.5	823	3.6	30
F14	290	6	13	203	119	182	2.5	4.5	434	6.1	30
F15	357	99	8.2	77	67	288	5.1	6.8	625	15	59
F16	288	1283	8.6	224	56	167	3.6	3.3	224	12	28
F17	39	1274	6.0	215	59	231	1.1	1.5	103	13	25
F18	329	177	10	211	78	202	5.7	4.9	637	9.0	55
F19	360	75	7.4	110	91	262	9.8	15	568	12	74
F20	293	486	5.8	231	88	268	3.7	4.1	528	11	37
F21	367	61	10	184	73	299	7.4	11	770	14	63
F22	313	6	7.7	162	110	166	3.8	11	575	5.6	43
F23	265	87	7.3	141	81	438	6.1	10	476	15	57
F24	449	44	6.0	73	86	629	14	14	639	13	79
F25	241	17	11	52	67	428	15	63	144	19	213
F26	291	11	7.8	70	85	728	11	13	575	17	67
F27	490	16	8.5	50	65	215	16	58	533	20	100
F29	277	89	2.2	133	101	375	3.5	12	545	18	48
F30	316	224	17	248	110	309	3.6	14	580	14	54
F31	370	165	13	302	119	378	5.3	5.1	539	16	68
F32	513	79	15	194	125	410	8.7	4.9	622	21	54
F34	230	601	5.6	152	51	292	3.0	6.0	421	12	50
F35	263	607	2.4	180	56	279	3.2	12	401	13	52
F36	195	707	3.8	365	54	167	3.2	9	336	13	45
F37	175	451	5.1	147	52	243	3.3	2.2	448	11	77
F200d	325	177	4	298	131	148	11	14	617	15	44
F200w	934	42	25	45	90	79	45	112	293	22	321

Note: All values in ppm. Analysis of all samples for Cl and U was attempted by INAA, but, all samples contain less than the detection limits of 60 and 0.5 ppm, respectively.

TABLE AI-8: Summary of INAA methods and sample concentrations.

Element	method of analys.	range of conc.	rock standard	conc. in standard
Cl	1	60 to 5200	1632b	1260+/-100
U	2	0.5 to 11	SY2, W1	285, 0.57
Gd	3	3 to 14	SY2	17
La	4	10 to 114	MRG-1	9.8
Sm	4	3 to 20	MRG-1	4.5
Ho	4	.28 to 2.1	MRG-1	0.49
Sc	4	4 to 55	MRG-1	55
Lu	5	.14 to .75	MRG-1	0.12
Nd	5	13 to 117	MRG-1	19.2
Yb	5	0.6 to 5	MRG-1	0.6*
Ce	6	30 to 350	MRG-1	26
Eu	6	1 to 4.3	MRG-1	1.39
Tb	6	0.13 to 1.3	SY2	2.5
Ta	6	0.5 to 8.5	SY2	2.01
Th	6	0.77 to 27	SY2	379
Hf	6	0.7 to 11	MRG-1	3.76
Cs	6	0.13 to 3	SY2	2.4
Rh	7	.1 to 50	SARM7	240
Pd	7	8 to 4400	SARM7	1530
Au	8	0.1 to 370	SARM7	310
Ir	8	.05 to 2.5	SARM7	74
Pt	8	20 to 1250	SARM7	3740

* denotes information value for element
All values in ppm except PGE which are ppb.

Method: 1: delayed gamma with 10 sec irradiation, 60 s delay and 10 min count, Rabbit site #4
 2: delayed neutron (60 s count)
 3: prompt gamma (500 s count)
 4: delayed gamma, 1 hr. epithermal irradiation, 3 day delay
 5: delayed gamma, 3.5 hr. thermal irradiation, 7 day delay
 6: delayed gamma, thermal irradiation and 40 day delay
 7: delayed gamma, Rabbit site 4 (fire-assay preconcentration)
 8: delayed gamma, 7 day delay (fire-assay preconcentration)

Table AI-9: Precision of analyses is given as standard deviation in percent of the mean measured value.

Element	no. of replic.	sample number	conc. ppm	1 sigma std.err.
Cl	4	1632b	1260	7.5%
	4	G84	360	20
U	3	SY2	284	3.0
	4	G84	1.83	7.0
La	4	F25	43	3.3
Ce	4	F25	93	5.0
Nd	4	F25	35	1.0
Sm	4	F25	6.00	2.6
Eu	4	F25	0.99	4.1
Gd	3	F25	5.06	2.0
Tb	3	F25	0.47	5.6
Ho	4	F25	0.67	12
Yb	4	F25	1.37	1.4
Lu	4	F25	0.26	2.1
Sc	4	F25	49	3.5
Ta	4	F25	1.45	4.3
Th	4	F25	10.1	10
Hf	4	F25	5.08	5.3
Cs	4	F25	0.58	18

Table AI-10: Summary of counting error, listed by respective ranges in concentration.

Element	conc. ppm	error percent
Cl	90-200	20-40
	200-500	10-20
	500-1000	5-10
	>1000	<5
La	12-20	5-10
	>20	<5
Ce	>30	<2
Nd	13-35	5-10
	>35	<5
Sm	2	30
	3-4	10-15
	4-6	5-10
	6-9	3-5
	>9	<3
Eu	0.9-5	<2
Gd	3-5	10
	5-9	5-10
	9-15	5
Tb	0.3	9
	.3-.65	5
Ho	.65-1.5	3-5
	.26	25
	.28-.56	10-15
Yb	.56-2	5-10
	.6-5	4-6
Lu	.1-.65	4-6
Sc	17-48	<1
Ta	<.6	5-6
	.6-9	4-5
Th	.6-1	5-7
	1-2	2-5
Hf	>2	<2
	.7-1	5-6
Cs	1-11	2-5
	.1-.2	20-30
	.2-.7	10-15
	.7-5	5-10

Table AI-11: Summary of irradiation and counting conditions for REE and other trace-elements.

 SHORT IRRADIATION
 THERMAL (10 SEC)
 Tdelay is 60 minutes
 Tcount is 600 seconds

Element	product isotope	gamma ray (keV)	half life
Cl	38Cl	2166.8	37.29m

 FIRST LONG IRRADIATION
 EPITHERMAL (1HR)
 Tdelay is approximately 3 days
 Tcount is approx. 1500 seconds

Element	product isotope	gamma ray (keV)	half life	comments
La	140La	1596*, 816	40.23h	negligible U int W (at 72 keV)
Sm	153Sm	69.6, 103.2*	46.7h	
Ho	166Ho	1380	26.7h	
Sc	46Sc	889.3	83.9d	

 SECOND LONG IRRADIATION
 THERMAL (3.5 HRS)
 Tdelay is approximately 7 days
 Tcount is approx. 1000 seconds

Element	product isotope	gamma ray (keV)	half life	comments
Lu	177Lu	208.34, 113	6.71d	negligible U int
Nd	147Nd	91.0*, 531.4	10.98d	
Yb	175Yb	396.1	4.2d	

 Tdelay is approximately 40 days
 Tcount is 2 hours

Element	product isotope	gamma ray (keV)	half life	comments
Ce	141Ce	145.67	32.5d	Th at 145.4
Eu	152Eu	122.1, 1408*	12.2y	check Ba at 124
Tb	160Tb	298.6, 879.4*	73d	Th at 300.1
Ta	182Ta	67.8, 1221*	115.1d	broad peak
Th	233Pa	311.96	27.0d	
Hf	181Hf	482.6	44.6d	
Cs	134Cs	795.9	2.07y	

 SHORT IRRADIATION
 THERMAL (60 sec.)
 Tdelay is 90 sec.
 Tcount is 120 seconds

Element	product isotope	gamma ray (keV)	half life
Rh	104Rh	51.4	4.34m
Pd	109Pd	188.9	4.69m

 LONG IRRADIATION
 THERMAL (1HR)
 Tdelay is approximately 5 days
 Tcount is approx. 1500-10000 seconds

Element	product isotope	gamma ray (keV)	half life	comments
Pt	199Au	158.8	3.15d	Au interference
Ir	192Ir	316.5	74.02d	
Au	198Au	411.8	2.695d	

Note: * indicate the preferred energy for counting.

Table AI-12: REE and trace element data for 17 samples determined by INAA.

	F1	F3	F5	F8c	F8p	F24	F25	F31	F200
La	19	13	14	14	12	32	43	32	19
Ce	37	31	32	30	nd	64	93	67	39
Nd	17	15	17	15	nd	28	35	32	21
Sm	3.87	3.28	3.42	3.44	3.65	5.31	6.00	6.66	4.27
Eu	1.34	1.23	1.36	1.27	nd	1.61	.985	1.95	1.38
Gd	nd	nd	3.75	3.08	nd	nd	5.06	3.75	3.27
Tb	0.31	0.33	0.32	0.26	nd	0.43	0.45	0.56	0.41
Ho	0.39	0.33	0.43	0.28	0.56	0.59	0.67	0.71	0.61
Yb	0.76	0.75	0.67	0.60	nd	1.20	1.36	1.29	0.95
Lu	0.15	0.15	0.14	0.16	nd	0.21	0.26	0.26	0.18
Sc	41	42	43	43	nd	41	48	42	40
Ta	0.92	0.60	0.55	0.56	nd	1.36	1.46	0.93	0.66
Th	1.20	0.68	0.77	0.84	nd	2.95	10.2	1.38	0.93
Hf	1.07	0.91	0.90	1.29	nd	1.74	5.08	1.37	1.31
Cs	0.32	0.19	0.16	0.13	nd	0.72	0.58	0.48	0.31

	F200w	G1	G2	G47	G48	G49	G49a	G50
La	64	115	136	60	66	188	95	94
Ce	120	243	255	117	132	354	178	182
Nd	46	94	99	52	57	107	69	79
Sm	7.96	16.7	17.4	9.52	9.90	20	14	13.4
Eu	1.35	4.30	3.95	2.47	2.66	3.53	3.18	3.36
Gd	5.49	11.7	nd	6.39	7.42	14.1	9.67	10.2
Tb	0.65	1.47	1.53	0.64	0.89	1.58	1.16	0.99
Ho	.843	1.84	1.75	0.79	0.92	2.10	1.65	1.25
Yb	1.55	4.08	3.89	1.76	1.91	5.04	3.16	2.29
Lu	.328	0.69	0.66	0.30	0.32	0.69	0.53	0.43
Sc	53	23	26	29	25	17	22	25
Ta	3.79	6.27	5.41	2.07	2.36	8.46	4.14	3.22
Th	12.9	14.4	12.7	3.53	5.03	27	8.39	7.70
Hf	8.29	6.89	6.13	1.94	2.71	11	4.10	3.82
Cs	1.71	4.84	4.33	2.17	2.69	0.69	2.13	2.99

Note: nd indicates not determined. All values in ppm.

Table AI-13: Nickel, Cu, Au, PGE and S data for the Marathon deposit.

sample	type	Ni	Ir	Rh	Pt	Pd	Au	Cu	S
F1	tdl	117	0.09	1.5	20		3.7	239	0.02
F2	tdl	114	0.3	3.4	106	102	3.3	398	0.03
F3	tdl	325	1.46	34	610	1495	103	8897	1.96
F4	tdl	464	2.31	64	1235	3896	362	17172	2.4
F5	tdl	189	nd	2.3	28	123	6.1	1297	0.1
F6	tdl	342	2.36	55	984	2410	213	13551	2.44
F7	tdl	240	1.25	27	435	869	112	5522	1.03
F8	tdl	308	1.59	52	638	3560	173	15173	2.76
F9	tdl	147	0.42	6.5	140	216	14	1092	0.1
F12	xen	129	0.2	1.4	13.9	26	2.5	132	0.01
F13	xen	132	1.11	3.7	nd	nd	2.8	36	nd
F14	xen	203	1.06	2.8	nd	nd	4.8	95	nd
F15	xen	77	0.1	1.2	18	8	9.7	131	0.01
F16	xen	224	1.11	2.8	44	54	5.1	62	0.21
F17	xen	215	1	2.4	37	56	2.8	86	0.42
F18	tdl	211	0.78	10	317	372	102	4763	1.35
F19	tdl	110	0.32	2.5	32	47	3	392	0.13
F20	tdl	231	1.85	23	247	690	48	3674	1.27
F21	peg tdl	184	1.61	32	593	2410	162	7885	1.39
F22	peg tdl	162	0.83	14	246	627	61	3838	0.9
F23	peg tdl	141	0.5	7.4	107	184	15	1915	0.32
F24	peg tdl	73	0.08	0.9	9.4	nd	2.3	718	0.14
F25	peg tdl	52	0.07	0.6	9.3	8	2.5	293	0.02
F26	peg tdl	70	0.15	0.7	17	nd	13	472	0.15
F29	tdl	133	0.23	4	55	113	14	2476	1.46
F30	tdl	248	0.62	9.8	152	390	32	5323	2.57
F31	tdl	302	0.68	15	300	770	87	6948	3.11
F32	tdl	194	0.41	6.4	105	267	26	4805	2.09
F34	xen	152	0.45	1	4.9	8	0.89	217	0.01
F35	xen	180	0.18	0.7	nd	10	0.16	97	0.01
F36	xen	365	0.66	1.3	13	18	0.92	151	0.01
F37	xen	147	0.35	1.1	14	13	1.6	165	0.01
F8c	tdl	406	6.5	40	3270	1080	406	11800	2.29
F8p	peg tdl	458	2.26	52	620	4370	136	12600	2.98
F200d	tdl	298	2.43	41	714	1930	141	7600	1.93
F200w	gran tdl	45	0.16	3.7	91	276	9.8	3200	0.28

symbols: tdl, Two Duck Lake gabbro; peg, pegmatitic; gran, granopyre;
xen, xenolith

Ni, Cu data in ppm, S in wt %, Au and PGE in ppb

Table AI-15: Results of 10 SARM7 standard determinations. The precision of PGE analyses is given as standard deviation and in percent of mean measured value. The counting error (1 sigma) is less than 3 to 5 % for each element.

	Pt	Ir	Au	Rh	Pd
sa1	3701	75	298	234	1493
sa2	3972	76	434	242	1526
sa3	4183	75.7	287	254	1498
sa4	na	80.9	265	258	1731
sa5	3850	75.1	226	232	1520
sa6	3387	71.6	191	216	1410
sa7	3828	74.3	556		
sa8	3821	75.2	295		
sa9	3514	68.5	289		
sa10	3404	67.6	261		
accepted value	3740	74	310	240	1530
precision percent	266 7.1	3.9 5.3	107 34	16 6.6	107 7.0

Table AI-16: Summary of counting error per sample listed by the respective range in concentration.

element	range of values (ppb)	range of error %
Ir	.01 to .1	15 to 30
	.1 to 1	5 to 15
	>1	<5
Rh	.5 to 1	10 to 30
	1 to 5	3 to 10
	>5	<3
Pt	<5	20 to 40
	5 to 10	10 to 20
	10 to 50	5 to 15
	>50	<5
Pd	8 to 25	15 to 35
	25 to 50	10 to 15
	50 to 200	5 to 10
	>200	<5
Au	>.05	<1

Table AI-17: Results of duplicate analyses.

sample	Ir	Rh	Pt	Pd	Au
F2	.33	3.4	111	102	3.3
F2a	.28	n.a.	98	n.a.	3.3
F3	1.46	34	595	1470	103
F3a	1.46	35	628	1522	113
F9	.42	6.5	137	204	9.7
F9a	.42	6.5	143	227	18
G3	.06	0.3	7.4	9.0	2.6
G3a	.09	0.8	7.0	12	3.8
G5	.11	0.5	8.2	22	3.6
G5a	.28	0.9	8.2	15	2.9
G10	.08	1.3	24	87	3.6
G10a	.07	1.5	30	68	9.7
G19	.07	0.8	9.0	n.d.	2.9
G19a	.10	1.4	n.d.	n.d.	1.8
G20	.06	0.5	7.6	13	3.0
G20a	.04	1.2	n.d.	15	1.2
G21	.08	0.8	8.8	26	3.6
G21a	.02	1.3	7.6	15	2.9

note:nd,not detected;n.a.,not analysed

Introduction

Olivine, plagioclase, orthoclase, clinopyroxene and orthopyroxene were analyzed with the JEOL JXA-8600 Superprobe electron microprobe at The University of Western Ontario. Minerals analyzed were selected from highly polished thin sections prepared by Geoplastech Inc, Toronto. Olivine, plagioclase and some pyroxene analyses were conducted by the author with the helpful guidance of R. L. Barnett and D. M. Kingston. Some pyroxene analyses were conducted by Barnett.

Olivine: Olivine grains were analyzed using a number of natural mineral standards, as follows: SiO₂, MgO and NiO using an olivine standard (P140, see Fleet & MacRae 1983), FeO using an orthopyroxene standard (R2202), CaO using a clinopyroxene standard (WAK), and MnO using a rhodocrosite standard (RHOD). The electron beam operated at 10.3 nA and 15 kV. Peak counting times were between 20s and 100s depending on the element. NiO data were obtained with 100s peak counts using the LIF crystal. Under these operating conditions the detection limit for NiO was found to be on the order of .03 wt.%, CaO 0.04 wt.%, and MnO 0.08 wt.%. To evaluate the accuracy and precision of olivine analyses 10 spots from 1 grain of standard P140 were analysed and the results are listed in Table AII-1.

Table AII-1. Results of 10 analyses from one grain of olivine standard P140 to test precision and accuracy of olivine analyses. The precision is given as standard deviation of mean measured values.

Element	Average	Precision	Accepted values
SiO ₂	41.05	0.25	40.85
FeO	7.13	0.20	7.23
MnO	0.11	0.03	0.07
MgO	51.59	0.49	51.63
CaO	0		
NiO	0.30	0.02	0.305
SUM	100.18		

Pyroxene and Feldspar: Pyroxene and feldspar were analyzed using several mineral standards as follows: albite (ALBI), orthoclase (ORTH), anorthite (AN90), clinopyroxene (WAK), and orthopyroxene (R2202). The electron beam operating conditions were the same as for olivine and peak counting times were 20s for all elements. Control of data quality was maintained by periodic analysis of standards during each session.